Thermo-optical and thermo-elastic effects onboard the LISA Pathfinder mission

Francisco Rivas García

Universitat Autònoma de Barcelona (UAB)

Departament de Física

Programa de Doctorat en Física

Thermo-optical and thermo-elastic effects onboard the LISA Pathfinder mission

Tesis presentada por Francisco Rivas García
para obtener el grado de Doctor en Física

Directores: Dr. Miquel Nofrarias i Serra, Dr. Carlos F. Sopuerta

Tutor: Dr. Diego Pavón Coloma

20 de septiembre de 2019

A mi familia.

"En ciencia el hecho queda, pero la teoría se renueva."
Prologue to the second edition of *Reglas y consejos sobre la investigación biológica. Los tónicos de la voluntad*
Santiago Ramón y Cajal

Agradecimientos

Escribir unos agradecimientos no es una tarea sencilla, sobre todo cuando se trata de dar gracias por la consecución de algo que ha llevado unos cuatro años pero que va ligado a todos aquellos estudios anteriormente realizados.

Todo empezó cuando mi gran amigo Paco me envió una oferta para realizar un doctorado enmarcado en una misión llamada LISA Pathfinder. Por tanto, es de justicia agradecerle a él en primer lugar ya que al enviarme aquel email me dió la oportunidad de empezar este tránsito.

Decidido ya a aplicar a dicha oferta, me puse en contacto con Carlos, quien muy comprensivamente y pacientemente entendió todos los problemas burocráticos que encontré y se amoldó a los tiempos que éstos fijaban. Él me abrió la puerta de este campo de estudio tan maravilloso y del grupo del ICE encargado de las misiones LISA Pathfinder y LISA. Además, siempre ha estado ahí para ayudarme en todo lo que he necesitado. Por esto y porque sin la confianza que él mostró en mí desde un principio hoy no estaría aquí escribiendo estos agradecimientos, ¡gracias Carlos!

Una vez ya firmado el contrato y cargado de ilusión por la nueva aventura que comenzaba, Carlos me presentó a la persona más importante en todo este periplo, Miquel. Él ha sido, además de una gran amigo, el mejor maestro posible. Tengo que agradecerle por toda su paciencia (casi infinita), por sus explicaciones sobre los PSD, el MCMC, sobre las Optial Windows y los Struts, etc., pero sobre todo por la fe que siempre ha mostrado en mí y por encontrar siempre la forma de motivarme y de hacerme ver el vaso medio lleno, nunca medio vacío. ¡Gracias Miquel!

¡Y qué decir de mi grupo del ICE! Juan Pedro, Víctor, Lluis, Ferran, David, Dani, Marius, Nacho, Juan, Carlos, Carles, Alberto, Pep e Iván, gracias por haberme hecho sentir como en casa, por todo lo que he aprendido de vosotros y por todas las risas y grandes momentos pasados. Deteniéndome un poco en Ferran, a él le tengo que agradecer toda la ayuda que me ha prestado y todo lo que me ha enseñado durante estos años, pero especialmente al principio, cuando yo no tenía ni pajorera idea. Como por una especie de obra del destino, mi primera habitación en Barcelona fue la que tuvo Ferran, mi predecesor en cuestiones térmicas, cuando él empezó su doctorado. ¡Qué pequeño es el mundo!

Y por supuesto, también he de detenerme en Juan Pedro. Lo cierto es que no puedo imaginar estos años sin él. Con él he compartido todas las visicitudes que conlleva un doctorado, los momentos de alegría y de alta motivación, los viajes y congresos, y también los momentos de desánimo y nuestras inquietudes post tesis. También hemos tenido innumerables charlas sobre política, historia, filosofía y teología, y además me ha enseñado mucho sobre libros de fantasía y lo poco que sé de voleibol (uno de los pocos deportes que no sigo). ¡Gracias Juan Pedro!

También quiero agradecer a todo el equipo de LISA Pathfinder y demás colaboradores durante estos años, Rita, Pep, Martin, Nikos, Michael, Michele, Paul, Bill, etc., todos grandes científicos de los que he podido aprender mucho. Especialmente quiero agradecer a la gente del AEI del grupo de LISA Pathfinder, Martin, Michael, Andi, Sara, Lennart, etc., y al Mensa team, por esos inolvidables tres mes de estancia en Hannover.

Gracias también a todos los doctorandos del ICE por nuestras comidas en el etse y por todos los momentos vividos, y en general a todos los miembros del instituto, un instituto del que me siento orgulloso de formar parte. También quiero agradecer al personal de administración del IEEC, Eva, Anna y Pilar, por todas las gestiones realizadas y por su enorme amabilidad. ¡Cuánta paciencia tenéis! Y también a Josep, que junto con Víctor y Lluis, tantas veces me han apañado el ordenador.

Por supuesto todo esto no habría ocurrido nunca sin mis padres. Gracias

papá y mamá por todo, por la educación que me habéis dado y sobre todo por haberme siempre dado ánimos y apoyo. Es imposible expresesar con palabras todo lo que significáis. Soy quien soy por vosotros. ¡Gracias papás! Y gracias hermana, por estar siempre ahí y por tu ejemplo, pues no conozco a nadie con una voluntad como la tuya, digna de Cajal. ¡Gracias Sandra! Y gracias a toda mi familia, especialmente a mis abuelos y abuelas, los mejores.

También quiero agradecer a todos mis amigos, Dani, Víctor, Paco, Manuel, Vellido, Guille, Cal y Cala, Roberto, Laura, Ana, Cantón, Aina, y todos los demás (que me perdonen a los que no menciono) porque dicen que los amigos son como una segunda familia, y vosotros ciertamente que los sois. Muy especialmente quiero agradecer a Dani, Víctor y Paco, por nuestros paseos y por tantos momentos inolvidables vividos y que seguiremos viviendo.

Para terminar quiero escribir unas pocas líneas a Silvia, mi compañera de viaje. Gracias por todo, por apoyarme siempre, por animarme, por escuchar todos mis problemas, por oír ensayar mis charlas una y otra vez, y por, en definitiva, estar ahí siempre. Sencillamente sin ti esto no habría sido posible. No se puede expresar con palabras todo lo que te debo, así que me limitaré a decir: ¡Babubillo babubu! ¡Gracias Silvia!

Cerdanyola del Vallès, Barcelona, septiembre de 2019

Prologue

The LISA Pathfinder mission has paved the way to the Gravitational-Wave space astronomy. Not only it tested the technology needed by a space observatory LISA-like, but also studied and analysed the non-gravitational forces that appear between two free-falling test masses. Indeed, after about a year and a half of the mission (including commissioning, science operation, and extension phases), the satellite measured a residual acceleration noise between the masses of (1.74 ± 0.05) fm $\mathrm{s}^{-2}/\sqrt{\mathrm{Hz}}$ above 2 mHz. It is an improvement roughly of a factor 15 with respect the LISA Pathfinder requirement established before the mission, and a factor 5 with respect the LISA requirement in that moment. This achievement has been possible thanks to the fact that the spacecraft had different subsystems. Besides acting on 15 degrees of freedom of the spacecraft, they allowed us to perform experiments to estimate and subtract the several disturbances.

Thermal fluctuations were one of the sources of perturbation that modified the relative acceleration between both test masses. Depending on whether they induce real forces on the masses or only changes in the optical path length, we distinguish two kinds of thermal disturbances, namely: those that are around the test masses and which produce real forces on them, and those that appear in locations such as the optical windows or the struts (thermo-optical and thermo-elastic contributions), where these thermal fluctuations can produce distortions that in turn change the optical path length of the laser. Aiming to monitor and analyse the temperature

onboard the satellite, it was equipped with 24 thermal sensors and 14 heaters distributed around the more critical parts of the instrument. With the thermal sensors we measured the temperature in those locations and with the heaters we stimulated thermally those components where the two kind of thermal disturbances commented before could acted.

In this thesis, in addition to showing the main results obtained during LISA Pathfinder, I am going to focus on the temperature. I will show how the temperature evolved thorough the mission in its different phases and what thermal stability we achieved. Furthermore, I will present the different in-flight experiments carried out to analyse and estimate the thermo-optical and thermo-elastic contributions, showing their impact on the total differential acceleration noise. Finally, we discuss the implications of these analyses to the future Gravitational-Wave observatories, such as LISA.

Contents

List of Figures

List of Tables

Acronyms

ADC Analog-to-Digital Converter.

AO Analysis Object.

AOM Acousto-Optical Modulator.

ASD Amplitude Spectral Density.

CFRP Carbon Fiber Reinforced Polymer.

CMB Cosmic Microwave Background.

DAL Days After Launch.

DAU Data Acquisition Unit.

DDS Data and Diagnostics Subsystem.

DFACS Drag-Free Attitude and Control System.

DFT Discrete Fourier Transform.

DMU Data Management Unit.

DOF Degrees Of Freedom.

DPS Differential Power Sensing.

DRS Disturbance Reduction System.

DWS Differential Wavefront Sensing.

EH Electrode Housing.

ELITE European LISA Technology Experiment.

ESA European Space Agency.

ESOC European Science and Operations Centre.

FEE Front End Electronics.

GRS Gravitational Reference Sensor.

GW Gravitational Wave.

IAU Integrated Avionics Unit.

IFO Interferometer.

IS Inertial Sensor.

ISS Inertial Sensor Subsystem.

LCA LTP Core Assembly.

LEOP Launch and Early Orbit/Operations Phase.

LIGO Laser Interferometer Gravitational-Wave Observatory.

LISA Laser Interferometer Space Antenna.

LPF LISA Pathfinder.

LTP LISA Technology Package.

LTPDA LTP Data Analysis.

MOC Mission Operations Centre.

NASA National Aeronautics and Space Administration.

NGO New Gravitational Observatory.

NTC Negative Temperature Coefficient.

OB Optical Bench.

OBC On-Board Computer.

OMS Optical Metrology Subsystem.

OW Optical Window.

PTA Pulsar Timing Arrays.

RIN Relative Intensity Noise.

RM Radiation Monitor.

STR Strut.

TM Test Mass.

TS Temperature Sensor.

UV Ultraviolet.

WB Wheatstone Bridge.

Chapter 1

Gravitational Waves and detectors

Gravitational Waves (GWs) are ripples in the fabric of spacetime produced by an energy-momentum distribution that changes over time (with a second time derivative of the quadrupole moment different from zero) [56, 77, 96]. Albert Einstein predicted them [38] as a direct consequence of his General Relativity theory. Like electromagnetic waves travelling through the vacuum, GWs travel at the speed of light (in General Relativity) and are transverse waves. These waves are very weak in such a way that the strongest ones we can observe come from events such as supermassive black hole mergers.

Building a GW space observatory is one of the biggest goals for the scientific community. Currently, there are several ground-based detectors like the Laser Interferometer Gravitational-Wave Observatory (LIGO) [4], which did the first observation of GWs on September 14th, 2015 [1], Virgo [5, 6], and KAGRA [79]. Several other detections have been carried out with LIGO and Virgo since the first, which are the starting point of GW astronomy [3]. However, the ground-based detectors are limited by several noise sources, such as seismic noise and gravity-gradient noise, that make detections at

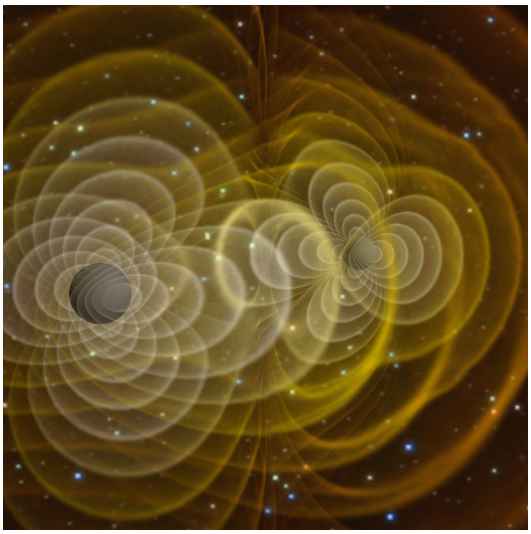

Figure 1.1: Image of GWs produced by a binary black hole system. Image obtained from [91].

low frequencies almost impossible. For that reason, it has proposed since the 70s to build a space observatory to explore GW sources emitting in the low-frequency GW band and observe the Universe from this new window.

In the early 2030s, the European Space Agency (ESA), with the collaboration of the National Aeronautics and Space Administration (NASA), is planning to send to space the first space observatory of GWs, the Laser Interferometer Space Antenna (LISA) [13, 27, 85]. LISA was selected as the L3 mission in June 2017 in ESA's Science Programme [84]. Previously, the science case of the L3 mission was selected on 2013 to be the science of "The Gravitational Universe" (white paper submitted by the evolved-LISA (eLISA) consortium [85]), a very wide science case based on low-frequency gravitational-wave astronomy.

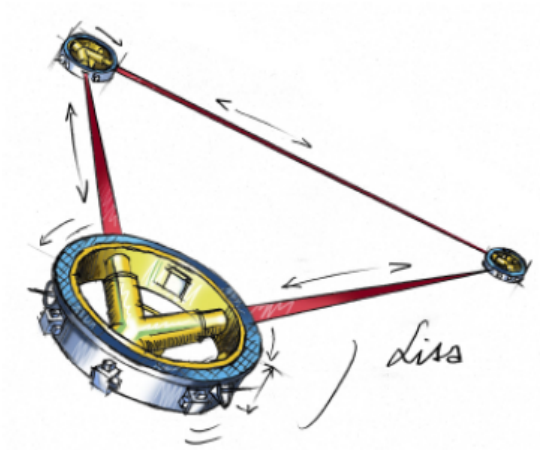

Figure 1.2: Artistic image of the LISA mission. Image obtained from [92].

1.1 Historical background

In the 1960s, J. Weber built the first GW detector known as Weber bars [98]. He designed a detector based on the action of tidal forces on aluminum resonant bars, at room temperature and isolated from ground vibrations and acoustic noise in the laboratory. He claimed to have detected GWs but the results were not confirmed by similar experiments done elsewhere [99, 100].

In 1974, Russell Alan Hulse and Joseph Hooton Taylor, Jr of Princeton University, discovered PSR B1913+16, a pulsar in a binary system with another neutron star. In 1993, they were awarded the Nobel Prize for this discovery along with the explanation they gave to the observed phenomenon [54]. By using the Arecibo antenna of 305 m, Hulse and Taylor detected radio emissions and identified the source as a pulsar which rotates 17 times per second around itself. When they measured these radio pulsations, they realized that there was a systemic variation in the arrival time of the signals. Sometimes the pulsations arrived a little earlier and some-

times a little later than expected. These variations changed repetitively and softly, with a period of 7.75 hours. They observed that they could explain it if the pulsar was together with another neutron star in orbit around a common center of mass. Sometime after this, they also realized that the period of the binary system changed according to the predictions of General Relativity for the emission of GWs. That was the first indirect detection of GWs.

The first direct observation of GWs was made on September 14th, 2015 by the two detectors of the LIGO observatory, GW150914 [1]. The waveform matched the predictions of General Relativity for gravitational radiation emanating from the inward spiral and merger of a pair of black holes of around 36 and 29 solar masses and the subsequent "ringdown" of the single resulting black hole (this final black hole has approximately 72 solar masses, which means that three solar masses were carried out in energy by the emitted GWs). It was also the first time that a binary black hole system and stellar-mass black holes with masses bigger than 30 solar masses were observed. Figure 1.3 shows this detection.

Since the first direct detection, a total number of 11 GW events have been found in the O1 and O2 observing runs [3]. At the time of writing this thesis, the O3 run was ongoing with a significant number of candidate detections being identified in the data. The one detected on August 17th, 2017 (GW170817, it was deduced that the detection should have happened in the 'blind spot' of Virgo, so it could give a better location in the sky of the event), was the first time that a GW event was also observed by electromagnetic emission [2]. These waves appeared as a consequence of a pair of two neutron stars spiralling closer to each other and finally merging. In Figure 1.4 we can see the first catalogue containing all the GW events detected by the LIGO-Virgo collaboration in runs O1 and O2.

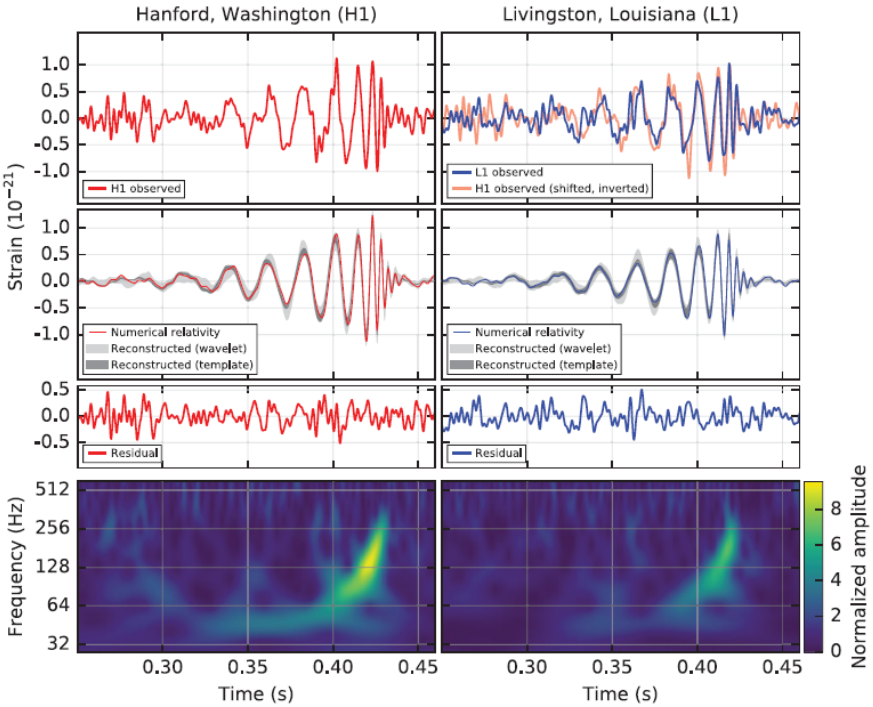

Figure 1.3: First detection of GWs made by both LIGO observatories. Image obtained from [1].

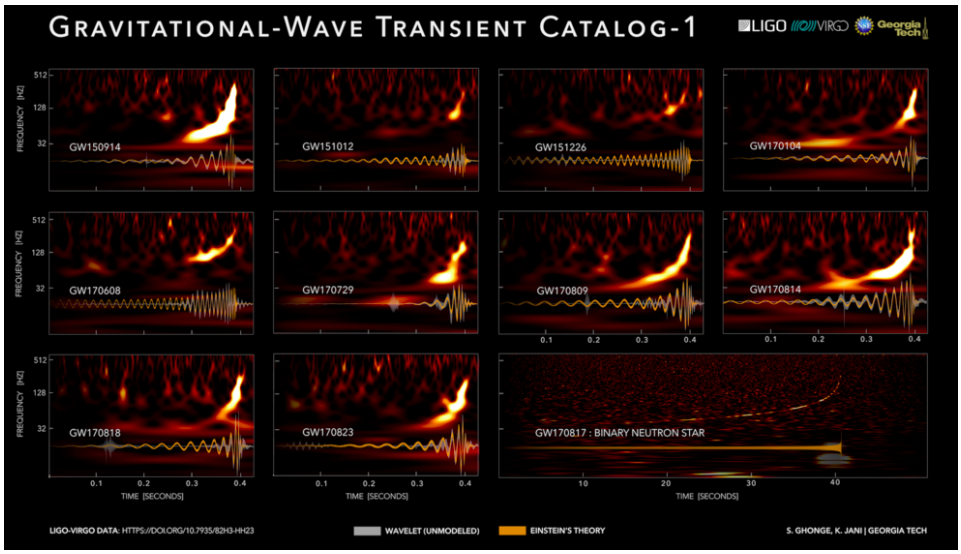

Figure 1.4: GWs observed so far. Image obtained from [91].

1.2 Mathematical foundations

Einstein's equations of General Relativity are [56, 77, 96]:

$$G_{\mu\nu} + \Lambda g_{\mu\nu} = kT_{\mu\nu}, \tag{1.1}$$

where $g_{\mu\nu}$ is the metric tensor, $G_{\mu\nu} = R_{\mu\nu} - \frac{1}{2}Rg_{\mu\nu}$ is the Einstein tensor ($R_{\mu\nu}$ is the Ricci tensor and R is the scalar curvature), Λ is the cosmological constant, and $T_{\mu\nu}$ is the energy-momentum tensor. If we consider that $\Lambda = 0$ and $k = 8\pi G/c^4$ (this value is derived from the movement of the inner planets of the Solar System), Eq. (1.1) is given by:

$$G_{\mu\nu} = \frac{8\pi G}{c^4}T_{\mu\nu}, \tag{1.2}$$

where G is Newton's gravitational constant.

If we take the weak-field approximation, it means that the spacetime is

flat when it suffers a small disturbance, so that the second order terms in the perturbation are negligible:

$$g_{\mu\nu} = \eta_{\mu\nu} - h_{\mu\nu} + O(h_{\mu\nu}^2), \tag{1.3}$$

where $\eta_{\mu\nu} = diag(-1\ 1\ 1\ 1\ )$ is the metric tensor of a flat space and $h_{\mu\nu}$ is the perturbation of that flat space. If $h_{\mu\nu} << 1$, $O(h_{\mu\nu})^2$ is negligible, we have the linear version of the equations of General Relativity.

Now, we define the following coordinate change:

$$x^{\alpha'} = x^{\alpha} + \xi^{\alpha}(x^{\beta}), \tag{1.4}$$

where ξ^{α} is a vector whose components depend on the original coordinate. If ξ^{α} is small and taking into account that by means of $\eta_{\mu\nu}$ we can raise and lower index, we get the following first order equation:

$$g_{\alpha'\beta'} = \eta_{\alpha\beta} + h_{\alpha\beta} - \xi_{\alpha,\beta} - \xi_{\beta,\alpha}, \tag{1.5}$$

where $\xi_{\alpha} = \eta_{\alpha\beta}\xi^{\beta}$, $\xi_{\alpha,\beta} = \frac{\partial \xi_{\alpha}}{\partial x^{\beta}}$, and $\xi_{\beta,\alpha} = \frac{\partial \xi_{\beta}}{\partial x^{\alpha}}$. Hence, $h_{\alpha'\beta'}$ can be defined as $h_{\alpha\beta} - \xi_{\alpha,\beta} - \xi_{\beta,\alpha}$, and if $|\xi_{\alpha,\beta}|$ are small, then the new $h_{\alpha\beta}$ will continue being small. This change is a coordinate gauge transformation.

The Riemann tensor to linear order of $h_{\mu\sigma}$ is:

$$R_{\mu\nu\rho\sigma} = \frac{1}{2}(\partial_{\rho}\partial_{\nu}h_{\mu\sigma} + \partial_{\sigma}\partial_{\mu}h_{\nu\rho} - \partial_{\sigma}\partial_{\nu}h_{\mu\rho} - \partial_{\rho}\partial_{\mu}h_{\nu\sigma}). \tag{1.6}$$

In analogy to electrodynamics we adopt of the Lorenz gauge:

$$\overline{h}_{\alpha\beta,\alpha} = 0, \tag{1.7}$$

where $\overline{h}_{\alpha\beta}$ is the trace-reverse perturbation. Taking into account this, the

Einstein tensor is given by:

$$G_{\alpha\beta} = -\frac{1}{2}(-\frac{1}{c^2}\frac{\partial^2}{\partial t^2} + \nabla^2)\overline{h}_{\alpha\beta}. \tag{1.8}$$

Therefore Einstein's equations for a weak field can be written as follows:

$$(-\frac{1}{c^2}\frac{\partial^2}{\partial t^2} + \nabla^2)\overline{h}_{\alpha\beta} = -16\pi G T_{\alpha\beta}/c^4. \tag{1.9}$$

In vacuum ($T_{\alpha\beta} = 0$) Eq. (1.9) will take the following form:

$$(-\frac{1}{c^2}\frac{\partial^2}{\partial t^2} + \nabla^2)\overline{h}_{\alpha\beta} = 0, \tag{1.10}$$

where ∇^2 is the Laplace operator.

The homogeneous and linear wave equation has as a particular solution the plane wave:

$$\overline{h}_{\alpha\beta} = A_{\alpha\beta}e^{ik_\lambda x^\lambda}, \tag{1.11}$$

where $A_{\alpha\beta}$ is a traceless, symmetric and constant tensor that contains the wave polarisation, so it is also called polarisation tensor.

The value of $\overline{h}_{\alpha\beta}$ is constant in a hypersurface in which the internal product $k_\lambda x^\lambda$ is constant.

Then, if we consider the wave vector $\overrightarrow{k} = (\omega, 0, 0, \omega)$, where ω is the wave frequency, propagating in the z direction, we have the canonical representation, which corresponds to the so-called transverse and traceless (TT) gauge, a particular case of the Lorenz gauge introduced before:

$$\overline{h}_{\alpha\beta} = A_{\alpha\beta}\cos[\omega(t-z)] = \begin{bmatrix} 0 & 0 & 0 & 0 \\ 0 & A_{xx} & A_{xy} & 0 \\ 0 & A_{xy} & -A_{xx} & 0 \\ 0 & 0 & 0 & 0 \end{bmatrix} \cos[\omega(t-z)], \tag{1.12}$$

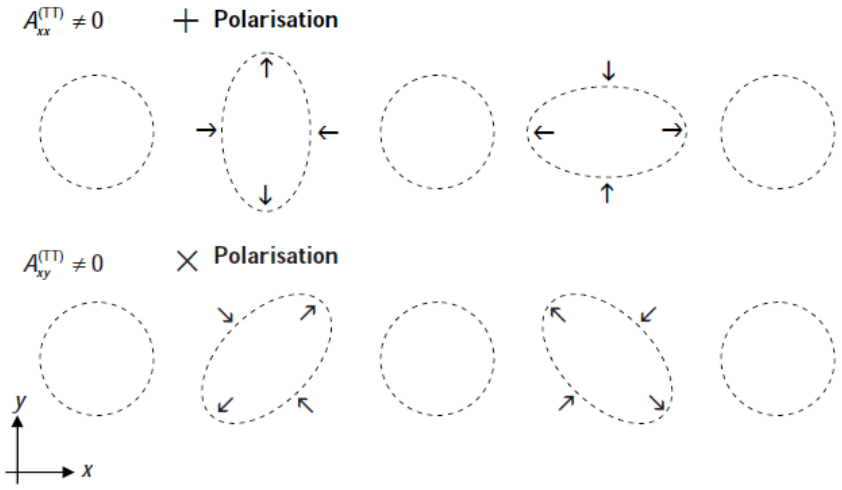

Figure 1.5: GWs present two possible polarisation modes: '+' and 'x'. Image obtained from [57].

where A_{xx} and A_{xy} are known as plus and cross polarisation amplitudes of the GW —see Figure 1.5.

1.3 Sources of Gravitational Waves

In general, whatever system with the second time derivative of the quadrupole moment different to zero produces GWs. We can distinguish four different types of GWs associated to different types of systems: continuous GWs, GWs of compact binary systems coalescence, burst GWs, and GW backgrounds [91].

Continuous GWs are produced by systems with an approximately constant frequency, for example, a star with a protuberance and with a very fast rotation around its axis. These sources produce weak GWs since they evolve over long periods and are less violent than, for example, the bursts.

GWs from compact binary systems coalescence are mostly detectable at the last moments of the life of these systems, when both objects are going to merge. Usually they are composed of two black holes, two neutron starts, or one black hole and one neutron star. As the two masses orbit around each other, their orbital distances decrease and their velocities increase, which causes the frequency of the GWs to increase until merger.

Although we have not detected burst GWs yet, their origin could be supernovae or gamma ray burst, short-duration sources. They would produce GW signals whose modulations would decrease in a short time after the explosion.

There are two types of GW backgrounds. The first one would be the stochastic signals originating from cosmological sources. They are the vestige of the GWs of the early evolution of the Universe. These could appear as a consequence of the uncoupling of the gravity from the other three fundamental forces, namely the electromagnetic force, the weak nuclear force, and the strong nuclear force. They could carry information about the origin of the Universe because they were produced between 10^{-36} and 10^{-32} seconds after the Big Bang while the Cosmic Microwave Background (CMB) was originated around 300000 years after the Big Bang. The spectrum produced by these waves would be similar to the spectrum produced in the CMB, continuous and equal at all points of the Cosmos. The other type of gravitational-wave background would appear by means of a combination of a large number of signals from binary systems that are emitted simultaneously throughout the entire space.

1.4 Gravitational Wave detectors

The basic idea for the different types of GW detectors developed (except for those that can detect the GW backgrounds) has been that when a GW

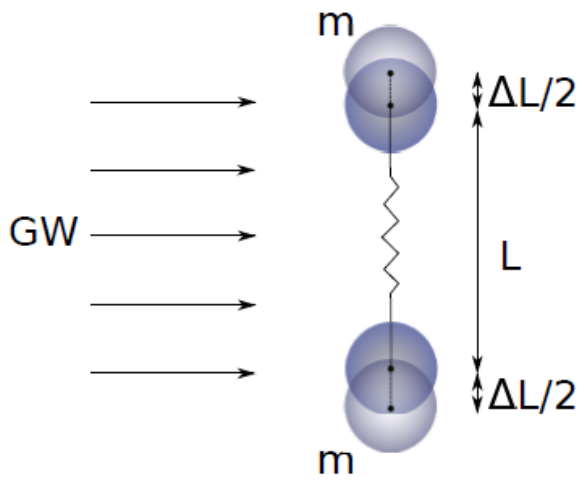

Figure 1.6: Change in the separation between two bodies when a GW passes. Image obtained from [46].

passes through two bodies that fall freely, their separation changes —see Figure 1.6. This change in the separation is measured in terms of strain, h:

$$h = \Delta L/L, \tag{1.13}$$

where L is the proper distance between both bodies and ΔL is the change when a GW passes through. This is a result of General Relativity.

Figure 1.7 shows the different GW sources and what types of detectors can carry out their observation. As we can see, GWs at high frequencies can be detected by the ground-based detectors like LIGO [1, 2, 4] or by means of resonant bars [10], space observatories can observe around the milliHertz [13, 85], the detections from 10^{-9} to 10^{-6} Hz would be made by Pulsar Timing Arrays (PTA) [41, 93, 103], and, finally, taking into account the CMB polarization [8], it would be possible to observe the trace of GWs at lowest frequencies, the so-called B modes of the CMB.

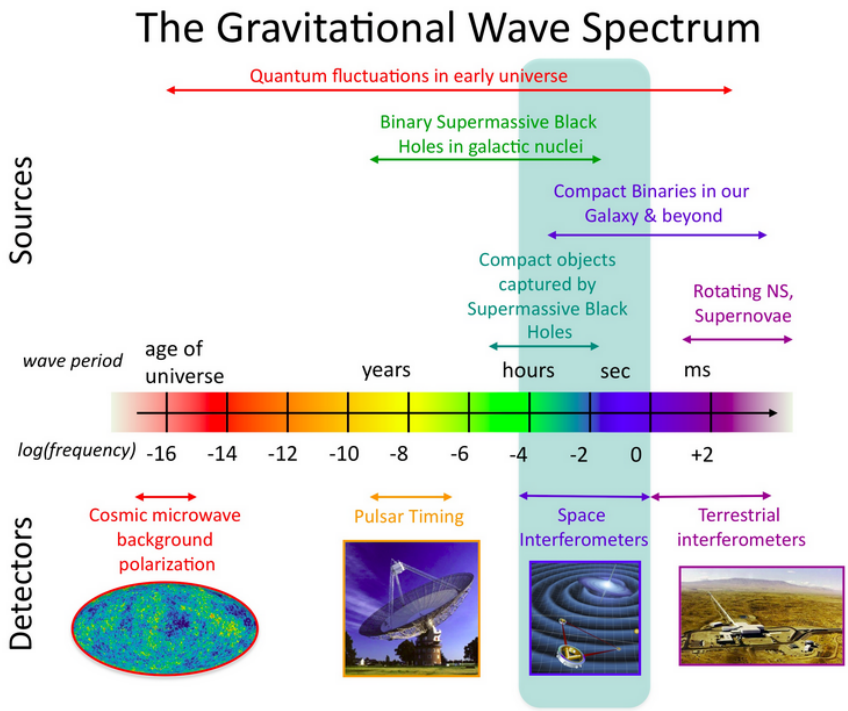

Figure 1.7: GW spectrum with sources and observatories. Image obtained from [90].

1.4.1 Resonant mass detectors

The principle of resonant mass detectors is based on the idea of the resonant amplification of a signal. As it is shown in Figure 1.6, if we have two bodies joined by a spring, a GW passing through will produce oscillations around the equilibrium position and the measurement will be the mechanical amplification of the characteristic frequency of the spring. The main noise sources for these detectors are the thermal noise and the read-out seismic noise, which will be described in Section 1.4.2.

As it was said in Section 1.1, J. Weber built the first GW detector, which was a resonant mass detector, in the 1960s [98]. It was a massive aluminium cylinder that operated at room temperature with a resonance frequency of approximately 1600 Hz. The fundamental problem with this type of detectors is that they are very sensitive only at a peak in their resonance frequency.

In 1971, several institutions agreed on the development of a network of this type of detectors (two of which were AURIGA [33] and NAUTILUS [26]) that worked together, in order to make correlation analysis to identify the direction and speed of the incoming waves. However, no coincident events were detected. These detectors are not operative nowadays, mostly because their technology has reached the maximum development and they have been superseded by the laser interferometric detectors.

1.4.2 On-ground laser interferometric detectors

By means of a Michelson interferometer of arm-length L we can measure the change of phase, $\delta\phi$, between two laser beams reflected in two bodies due to the motion of the masses when passing a GW [60]:

$$\delta\phi = 2\frac{\omega_{\mathrm{L}}}{\Omega_{\mathrm{GW}}} h_{+} \sin\frac{\Omega_{\mathrm{GW}}\tau}{2}, \tag{1.14}$$

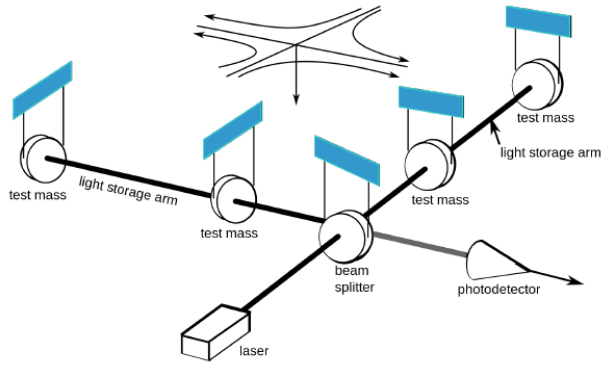

Figure 1.8: Laser interferometer detector. Image obtained from [91].

where Ω_{GW} is the angular frequency of the GW which induces a polarised strain h_+ aligned with the arms of the interferometer, ω_{L} is the angular frequency of the laser, and $\tau = 2L/c$ is the time that a beam takes to complete twice the distance that separates the bodies of a single arm, with c being the speed of light. Figure 1.8 shows a scheme of this kind of detector. It is possible to increase the effective length L a factor nearly 100 by adding Fabry-Perot cavities (one for each arm), which amplifies the laser power in the cavities. By increasing the length of the arms of the interferometer, it is possible to increase the size of the signal in the data-stream.

In short, because of GWs interact with matter by compressing objects in one direction and stretching them in the perpendicular direction, the most modern detectors are L-shaped and measure the relative lengths of their arms by means of laser interferometry, which observes the interference patterns produced by combining the light of both arms in the photodetector. Three of these interferometers are in USA: two of them in Hanford, Washington State, one of 4 km and another of 2 km (that serves for testing and for prototyping), and the other one of 4 km in Livingston, Louisiana —see Figure 1.9. They are called LIGO [37, 47], which is the biggest GW

Figure 1.9: LIGO Livingston observatory. Image obtained from [91].

detector to date. Other ground-based detectors are Virgo [5, 6] in Italy and KAGRA [79] in Japan.

Since directional observations cannot be made with a single detector such as LIGO (without counting the rotation of the Earth around the Sun that allows a first directional discrimination), multiple interferometers are needed to locate GW sources with a high precision, except for continuous signals. GWs travel at a finite speed, which is assumed (according to General Relativity) that is the speed of light. This causes a delay (of about 10 milliseconds) in the detection between the two LIGO detectors. Using this delay and the delay between LIGO and its international partners, it is possible to find a more accurate location of the GW source in the sky. As mentioned in a previous section, this procedure was followed in the observation of GW170817 [2] (coalescence and merger of two neutron stars), which allowed its detection in many bands of the electromagnetic spectrum at different times. The use of multiple detectors can also help to distinguish GW emitters.

The main noise sources for these detectors are the seismic noise, the thermal noise, the shot noise, and the gravity-gradient noise [57, 70]. The seismic noise is the main limitation which appears at a frequency below 10 Hz, the seismic wall. The mechanical vibrations are filtered with pendulums and several vibration isolating systems as piezoelectric actuators. Between 50 and 250 Hz the thermal noise limits, mainly as a result of Brownian noise in the mirrors. Regarding the shot noise, it limits above 250 Hz and appears due to fluctuations in the intensity of the light in the photodiode. Finally, we can find others limits such as those caused by local changes in the newtonian field, a noise source known as gravity-gradient noise. This puts a wall at around 1 Hz, which prevents laser interferometer ground-based detectors from detecting sources below that frequency. This also motivates the development of space-based detectors like LISA to access the low-frequency band of GWs.

1.4.3 Pulsar Timing Arrays

An array of millisecond pulsars, which are highly accurate clocks that emit pulses of electromagnetic radiation, can be used in the Galaxy as a detector, by measuring changes in the arrival times (to the Earth) of the emitted pulses. GWs emitted by, for example, massive black hole binaries in the centres of merging galaxies can vary the arrival times of the pulses in the order of 10 ns per year.

There are currently three projects using this technique, the Australian Parkers PTA [103], the European PTA [41, 93], and, finally, the American NANOGrav [9]. They collaborate in the International Pulsar Timing Array project [53]. The future will be the Square Kilometer Array (SKA).

1.4.4 Cosmic Microwave Background polarisation

The primordial GWs produce a signal in the polarisation of the anisotropies of the CMB. The polarisation vector field can be decomposed into two

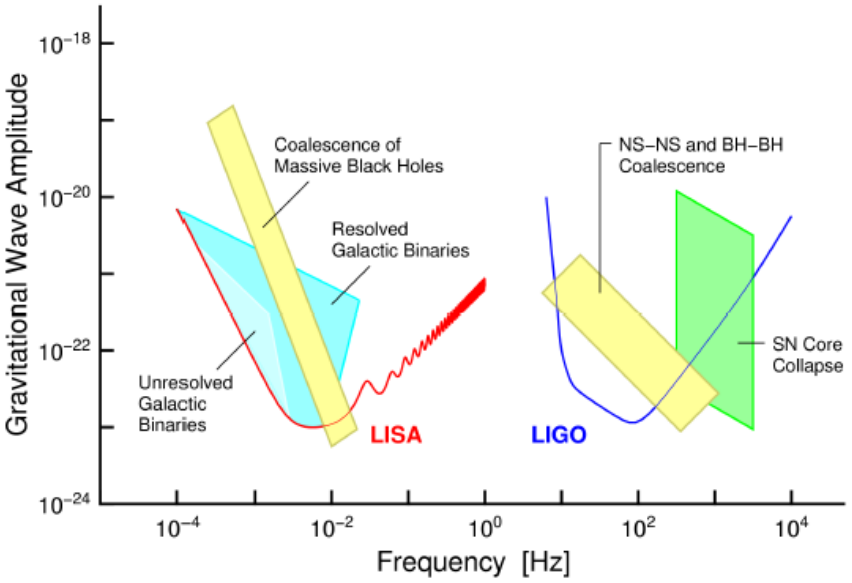

Figure 1.10: LISA and LIGO sensitivities. Image obtained from [42].

modes, a null rotational mode, E mode, and a null divergence mode, B mode. The latter mode can not be produced by scalar perturbations, so that its detection is an indirect signal of the existence of quadrupole component that could be directly associated with primordial GWs.

BICEP2 [67] announced in March 2014 a possible detection of GWs but later measurements with Planck [7] ruled out this possibility and associated the observed rotational structures in the polarisation to interstellar dust [8].

1.4.5 Space-based observatories of Gravitational Waves: LISA

Due to the limitations of the ground-based detectors seen in the previous section, it is necessary to build a space observatory of GWs if we want to observe in the milliHertz range, where there are GWs coming from supermassive black hole mergers, or from earlier phases in the life of binary black

hole systems or binary neutron star systems than the phases observed by on-ground detectors (the moments before merging). In the 1980s, NASA studied a mission that consisted of six spacecrafts in a heliocentric orbit. Between 1990 and 2005 the conception of the observatory was changing. First, in the classic version of LISA there were three spacecrafts and three arms with a length of 5 million km each. In 2012, NASA decided that it could not follow a joint schedule with ESA and this development forced the ESA to go forward with a reduced version called New Gravitational Observatory (NGO), with only two arms of 1 million km each. In 2013, ESA approved the science theme proposed by the white paper "The Gravitational Universe" [85], where, as an example, an observatory proposal was made, eLISA. Finally, after the GW detections by LIGO-VIRGO and the success of LISA Pathfinder (LPF) [15, 62, 69], LISA was selected as the L3 mission in January 2017 [84]. In this case, the observatory will consist of three 2.5-million km arms. The launch is expected to be in 2034.

The scientific objectives of this mission are very diverse: to study the nature of black holes, specifically the massive black hole mergers, and map the spacetime around them; to explore stellar populations as well as the structure and dynamics of the galactic core; to answer fundamental questions about the nature of gravity (if the graviton has mass or not, the speed at which GWs propagate, etc) and perform more and better tests of General Relativity; to test new physical and cosmological theories; and to explore TeV energy scales.

In the version proposed in the document that was selected by ESA for the L3 mission in 2017 [84], LISA will be composed of three spacecraft in an Earth-trailing heliocentric orbit between 50 and 65 million km from Earth with a constellation-plane inclination of 60^o, having this constellation a triangle shape with a size for each side of 2.5 million km, as seen in Figure 1.11.

Each spacecraft will contain two Test Masses (TMs), each of which will

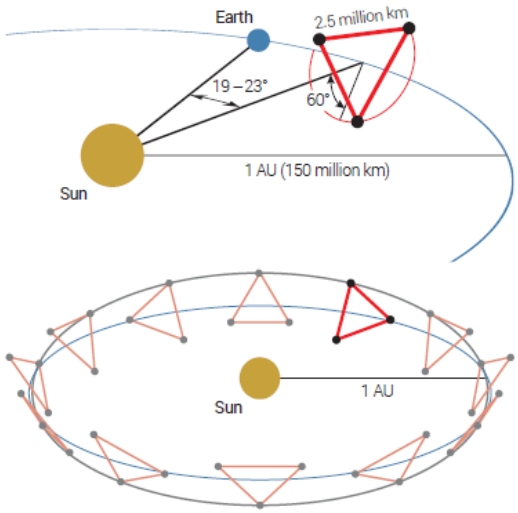

Figure 1.11: LISA orbit. Image obtained from [84].

be in a nearly perfect free-fall inside an Electrode Housing (EH) which in turn will be contained in the Gravitational Reference Sensor (GRS). It will be possible to measure the TM local position with respect the walls of its respective EH by means of capacitative measurements.

By means of three independent interferometric combinations [84] as seen in Figure 1.12, we can measure the distance changes between the TMs caused by the GWs, that will be of the order of pm to nm. These three independent combinations allow simultaneous measurement of the two possible polarisations of the GW and the characterisation of the instrumental noise background. The TM-TM measurement for each arm is divided in these parts: TM1 to Optical Bench (OB) in spacecraft 1, OB in spacecraft 1 to OB in spacecraft 2 through telescopes, and, finally, OB in spacecraft 2 to TM2.

Each spacecraft will be equipped with different subsystems (for exam-

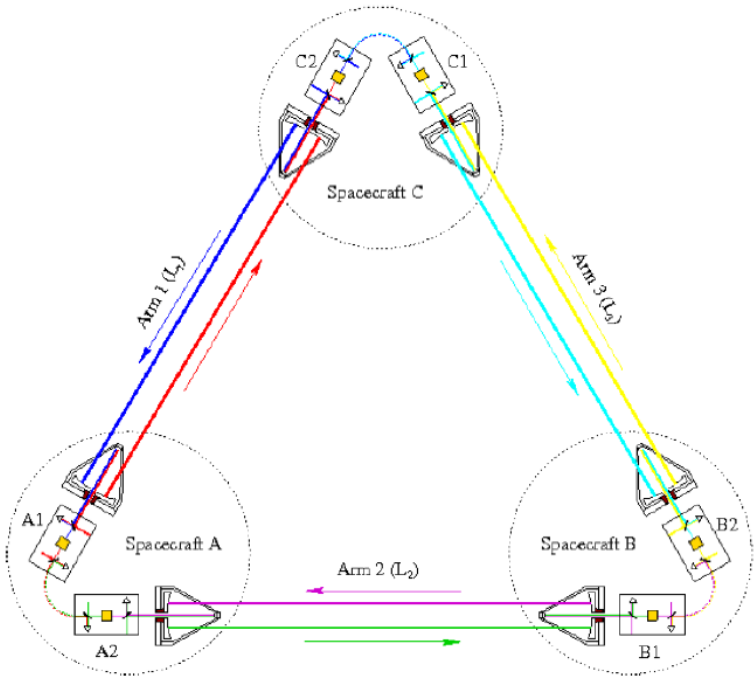

Figure 1.12: LISA configuration. Image obtained from [34].

ple, the thermal diagnostics subsystem, part of the Spanish contribution to the mission) that will allow to estimate and remove the non-gravitational forces around the TMs (taking into account the LPF results [17, 21]) of the measurements. In addition, like for the LPF case, each spacecraft will have a set of thrusters that will apply tiny forces of the order of microNewton to keep the spacecraft centred on one of the TMs.

In terms of the single TM acceleration spectral density, the requirement for LISA is as follows [84]:

$$S_{\mathrm{a}}^{1/2} \leq 3 \cdot 10^{-15} \frac{\mathrm{m}\ s^{-2}}{\sqrt{\mathrm{Hz}}} \cdot \sqrt{1 + (\frac{0.4\ \mathrm{mHz}}{f})^2} \cdot \sqrt{1 + (\frac{f}{8\ \mathrm{mHz}})^4} \qquad (1.15)$$

$$100\ \mu\mathrm{Hz} \leq f \leq 0.1\ \mathrm{Hz} \qquad \text{requirement}$$

$$20\ \mu\mathrm{Hz} \leq f \leq 1\ \mathrm{Hz} \qquad \text{goal}$$

To reach the acceleration noise level that appears in Equation (1.15), the proposed requirement for the TM-TM interferometric distance should be [84]:

$$S_{\mathrm{IFO}}^{1/2} \leq 10 \cdot 10^{-12} \frac{\mathrm{m}}{\sqrt{\mathrm{Hz}}} \cdot \sqrt{1 + (\frac{2\ \mathrm{mHz}}{f})^4} \qquad (1.16)$$

$$100\ \mu\mathrm{Hz} \leq f \leq 0.1\ \mathrm{Hz} \qquad \text{requirement}$$

$$20\ \mu\mathrm{Hz} \leq f \leq 1\ \mathrm{Hz} \qquad \text{goal}$$

This last requirement concerns the interferometric measurement system, which contains the laser, the clock, the telescope, the OB, the phase measurement system, and the Time-Delay Interferometry (TDI) [87] processing. The TDI will take the laser measurements and it will drastically reduce the laser frequency noise by synthesizing virtual equal-arm length interferometers.

Much of the technology necessary to carry out all these measurements has been tested by LPF (Chapter 2) while the first long-distance inter-

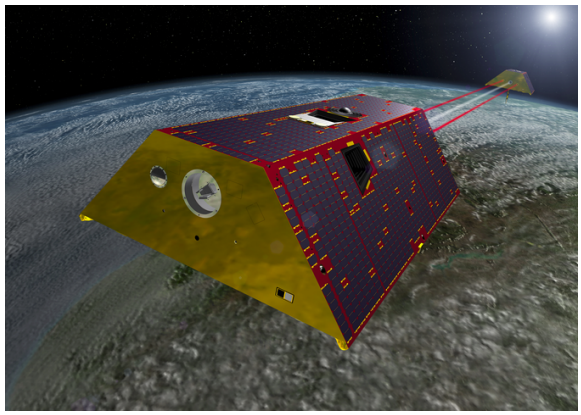

Figure 1.13: The two GRACE Follow-On satellites follow each other in orbit around the Earth, separated by about 220 km. Image obtained from [89].

spacecraft laser interferometer has been successfully tested by GRACE Follow-On (the TDI has not been tested because GRACE Follow-On has only one arm and for the TDI more arms are needed) —see Figure 1.13—, which is composed of two satellites separated by about 220 km which follow each other in orbit around the Earth [89]. These two missions have tested key elements for LISA and paved the way for its successful implementation.

Chapter 2

The LISA Pathfinder mission and its results

As seen in Chapter 1, the ground-based detectors of GWs present several noise sources, such as the seismic noise, which limit their measurement capability at low frequencies, below 1 Hz. GWs coming from, for example, supermassive black hole mergers can not be detected on ground. Hence, it is necessary to build a space observatory to open the low-frequency window. LISA has been already selected as the L3 mission of ESA's Cosmic Vision Program [84].

In order to test the technology necessary to build LISA, ESA, with collaboration of NASA, developed LPF [15, 62, 69]. The aims of this mission were to test the technology necessary to build a space observatory of GWs and estimate the non-gravitational perturbations of the residual acceleration between two solid gold platinum cubes that flowed in a near-perfect gravitational free fall. During the future LISA mission, it will be necessary to remove all these non-gravitational perturbations of the measurements to be only susceptible to the gravity of space.

In this chapter, we will see the different components of LPF, how it

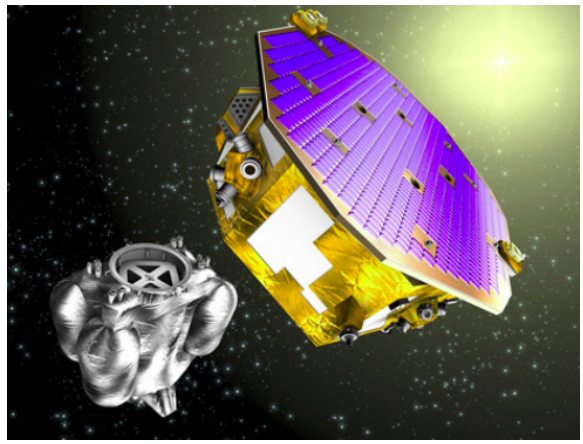

Figure 2.1: Artistic image of LPF. Image obtained from [92].

worked, and the main results obtained during the mission.

2.1 Introduction

This mission was proposed for the first time in 1998 to the ELITE (European LISA Technology Experiment) program. In 2000, a proposal was made to carry out a joint mission between two spacecrafts: LISA and Darwin Pathfinder. This second one would consist of four or five spacecrafts that would search Earth-like planets around other stars and analyse their atmospheres to see if their chemical composition could lead to life. Finally, this concept was discarded and it was established a single spacecraft, passing the mission to be called LISA Pathfinder. It was agreed that Europe would build the LISA Technology Package (LTP) and NASA the Disturbance Reduction System (DRS). Both would be equipped with two inertial sensors, a laser metrology system, thrusters, and a drag-free control system. However, during the development phase, some key units from the DRS were descoped and only the colloidal thrusters and control units ended up as a part of the mission.

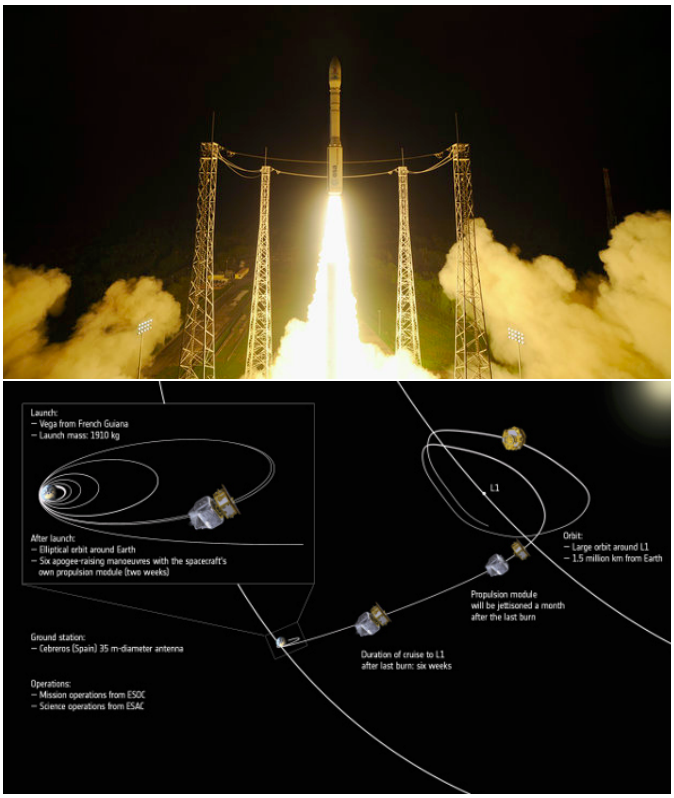

Figure 2.2: *Top*: LPF launch. *Bottom*: LPF Lissajous orbit. Images obtained from [92].

After more than a decade of development, LPF was launched from Kourou, French Guiana on December 3rd, 2015. It was sent to a metastable orbit (Lissajous orbit) 1.5 million kilometers from Earth towards the Sun around a point known as the first Sun-Earth Lagrange point (L1) and it was operating until July 17th, 2017 when it was decommissioned by ESA —see Figure 2.2.

The main scientific goal of LPF was to reach the following differential acceleration noise between the TMs separated 38 cm [15, 62]:

$$S_{\mathrm{a}}^{1/2} \leq 3 \cdot 10^{-14} \cdot \sqrt{1 + (\frac{f}{3\,\mathrm{Hz}})^2}\ \mathrm{m}\ s^{-2}/\sqrt{\mathrm{Hz}} \tag{2.1}$$

$$1\,\mathrm{mHz} < f < 30\,\mathrm{mHz}$$

To get the acceleration noise level that appears in Eq. (2.1), the requirement for the TM-TM interferometric distance was [15]:

$$S_{\mathrm{IFO}}^{1/2} \leq 9 \cdot 10^{-12} \cdot \sqrt{1 + (\frac{3\,\mathrm{mHz}}{f})^2}\ \mathrm{m}/\sqrt{\mathrm{Hz}} \tag{2.2}$$

$$1\,\mathrm{mHz} < f < 30\,\mathrm{mHz}$$

Since gravity is the weakest fundamental interaction, by using laser interferometry of a resolution of pm to measure the relative acceleration of two masses in free-fall conditions, it has been possible not only to achieve the above requirements but also to improve expectations, as we will see in the following sections.

2.2 LISA Pathfinder spacecraft

The spacecraft was foreseen with all the instruments to correctly perform all the experiments during the mission. It also supported the propulsion module until its release once LPF was in the way to its orbit.

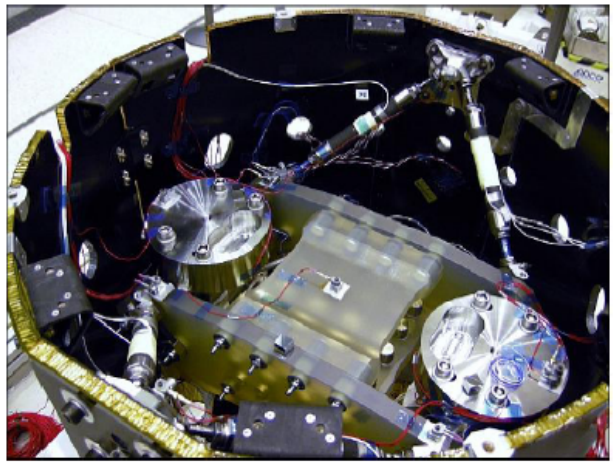

Figure 2.3: LTP inside the thermal shield. Image obtained from [12].

The platform of the spacecraft was provided with mechanical support for the rest of the spacecraft's subsystems. It had the shape of an octagonal prism with a diameter of 2.31 m and a height of 0.96 m. One of the two bases was covered by a sunshield panel that had an array of triple-junction of three GaAs solar cells of 2.8 m^2, while the other base was connected to the propulsion module. A large central cylinder contained the LTP Core Assembly (LCA) [62].

Summarizing, we could say that the fundamental components of LPF were [15, 62]:

- The LISA Technology Package (LTP), which contained two cubic Test Masses (TMs) of 46 mm for each side and which served both as mirrors for the interferometer and inertial references for the position control system (thrusters, Drag-Free Attitude Control System (DFACS), and diagnostics subsystem). The LTP was a single LISA arm shrunk from 2.5 million km to 30 cm.

- Colloidal thrusters, the NASA contribution, whose function was the same as the thrusters of ESA, cold gas thrusters, but using colloidal particles to propulse instead of cold Nitrogen gas. The latter were originally developed for ESA's GAIA mission [40]. Thrusters applied tiny forces (microNewton) to keep the satellite centred on one of the TMs.

2.2.1 The LISA Technology Package

The main role of the LTP —see Figure 2.4— was to achieve a differential acceleration measurement between the two free-falling TMs according to the scientific objective —see Eq. (2.1). It consisted of two main subsystems:

- Gravitational Reference Sensors (GRSs) [15, 62, 69].
- Optical Metrology Subsystem (OMS) [15, 42, 50, 62, 69, 71].

In addition, the satellite was equipped with a Data and Diagnostics Subsystem (DDS), the Spanish contribution to the LPF mission, led by the Institut d'Estudis Espacials de Catalunya (IEEC). The Spanish contributions to the LISA Pathfinder and LISA missions have been funded through the following national projects of the Spanish ministry that manages science and technology: *Development and Exploitation of the LISA Pathfinder Mission and Contributions to The Gravitational Universe and STE-QUEST* (ESP2013-47637-P), *Topical Network on Gravitational Waves* (FPA2015-69815-REDT), *From LISA Pathfinder to the ESA-L3 mission: Towards Gravitational Wave Astronomy from Space* (ESP2015-67234-P), and *Spanish Contribution to LISA, the ESA-L3 Mission* (ESP2017-90084-P).

Gravitational Reference Sensor Subsystem

The GRSs contained the two TMs and all the systems that were interacting with them such as Electrode Housings (EHs), Front-End Electronics (FEE),

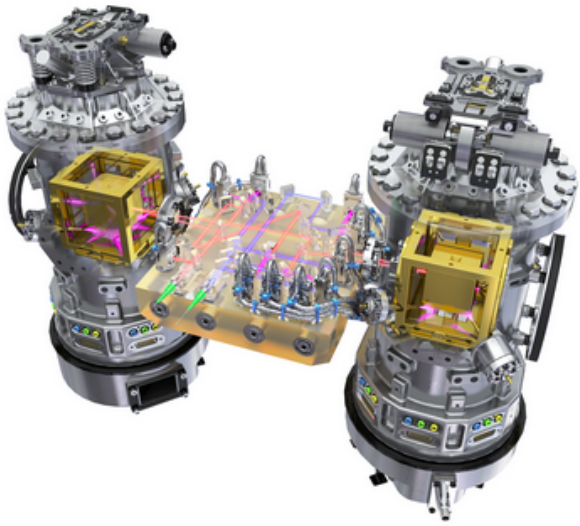

Figure 2.4: Artistic image of the LTP. Image obtained from [92].

vacuum system, charge management, and caging mechanism [15, 62, 69] — see Figure 2.5.

The TMs were inside the EHs with a pressure less than 10^{-5} Pa (by using a venting duct for each EH, it was possible to reach a pressure as low as possible by evacuating the particles from residual outgassing). By means of the electrodes (made of gold-coated sapphire) located on the inner wall of them, the EH sensed and controlled all the six Degree of Freedom (DOF) of each TM [28]. There was a distance of 4 mm between these electrodes and their respective TM.

The read-out electronics, Inertial Sensor Subsystem Front End Electronics (ISS FEE), was arranged in such a way that the electrodes of opposite faces of the TM were combined via capacitive sensing. So, a change in the position of the mass produced a bi-polar differential signal that was intro-

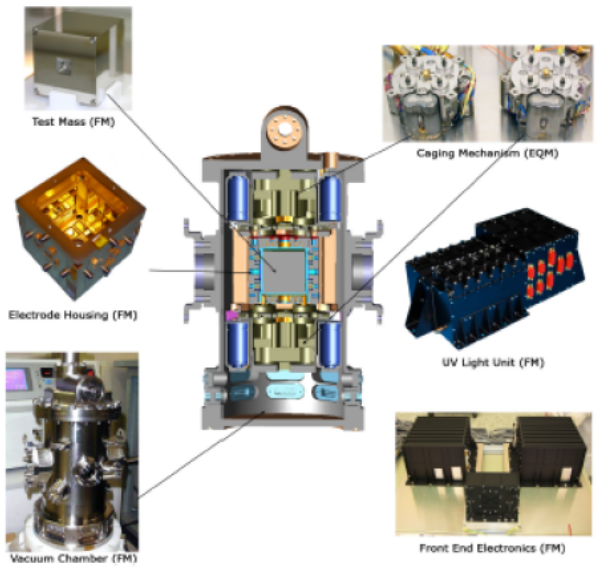

Figure 2.5: Main components of a GRS. Image obtained from [69].

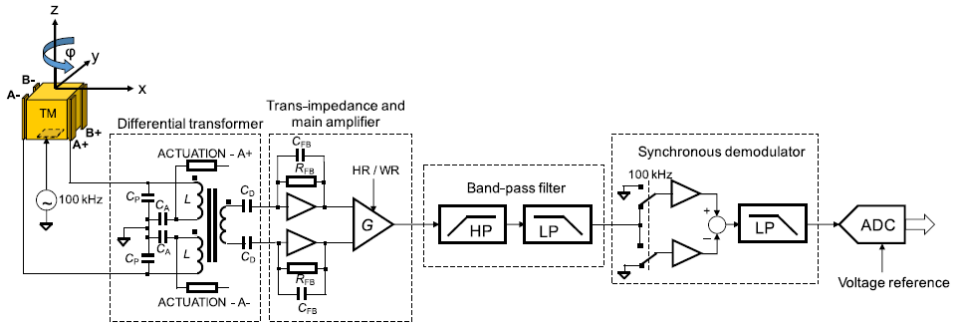

Figure 2.6: A single TM channel connected to its ISS FEE, along the x-axis. Two pairs of electrodes (A+ and A-, B+ and B-) allow simultaneous measurement of the TM displacement and rotation, which is achieved by measurement of the gaps between the TM and the electrodes at opposing sides of the TM. The actuation circuit (one for each electrode) applies forces and torques on the TM using the same electrodes. 100 kHz AC bias is injected on the TM, measuring differential currents, which are also amplified and converted into an AC sensing voltage proportional to the TM motion. Sensing voltage is filtered at the AC injection frequency and its amplitude is demodulated and converted into a digital value. Image obtained from [18].

duced as input data in the DFACS. The ISS FEE could actuate on the TM correcting its displacement by applying forces and torques on it using the same electrodes —see Figure 2.6. Results in flight about this can be found in [18].

The TMs were charged as a result of collisions with cosmic rays and solar charged particles. By means of fiber optic cables, ultraviolet (UV) light from Mercury vapor lamps were put inside the EHs. Depending on the sign of the electrical charge of the TM, the light shone on the TM or on the EH in order to discharge the masses. Experiments to understand the charge-induced force noise on the TMs were carried out during the mission [19].

On the other side, the Caging Mechanism Assembly kept the masses locked during the launch and the transfer phases. When the spacecraft

arrived at its orbit around L1, the TMs were released with less than 5 μm/s and 100 mrad/s to pass to the free-fall state [102].

Optical Metrology Subsystem

Onboard LPF, we had a Nd:YAG laser with wavelength of 1064 nm and a power of near 25 mW [15, 42, 50, 62, 69, 71]. The interferometry was split in two parts, as seen in Figure 2.7:

- The modulation bench, which was composed of the first Beam Splitter (BS0), Acousto-Optic Modulators (AOMs), and optical fibres. The beam was divided in two paths and each of them was shifted in the frequency (a different amount) with the AOMs, one at 80 MHz and the another one at 80 MHz + 1.2 kHz, with a frequency difference between both of 1.2 kHz (heterodyne frequency). After this, by means of the optical fibres the two beams arrived at the OB.

- The OB, which was composed of a block of Zerodur base plate (200$\times$ 212 $\times$ 22.5 mm) with mirrors of fused silica [39, 71]. Here, the beams were recombined and carried to the Photodiodes (PDs).

Once the two beams with their shifted frequencies arrived at the OB, different beam splitters formed four interferometers (IFOs) as seen in Figure 2.8:

- x_1 interferometer, by means of which we obtained the relative position between the TM1 and the OB, not only the distance but also two angles, one with respect the z-axis and another one with respect y-axis. This distance drove the drag-free control loop that used the microNewton thrusters to exert forces on the spacecraft.

- $x_1 - x_2$ interferometer, by means of which we obtained the relative distance between both TMs, as well as the angular positions with respect the z-axis and the y-axis. This distance drove the electrostatic

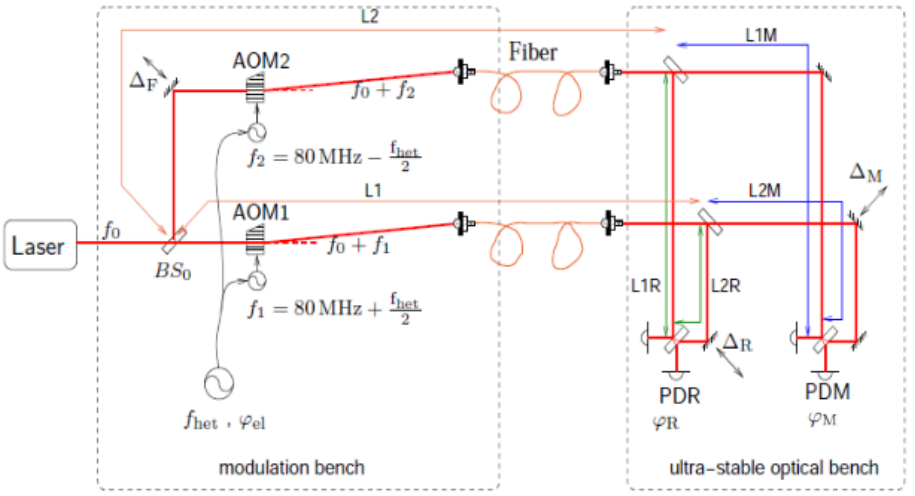

Figure 2.7: This image shows the two different parts in the LTP interferometry, namely the modulation bench and the OB. In the OB we can observe the two different interferometric measurements obtained, the phase measured by the measurement interferometer, φ_M, and the phase measured by the reference interferometer, φ_R. The main interferometer measurement is the difference between both, $\varphi_M - \varphi_R = \Delta_M - \Delta_R$. In LPF there were two measurements interferometers, to get, on the one hand, the interferometric distance between one TM and the OB, and, on the other hand, the interferometric distance between both TMs. Image obtained from [42].

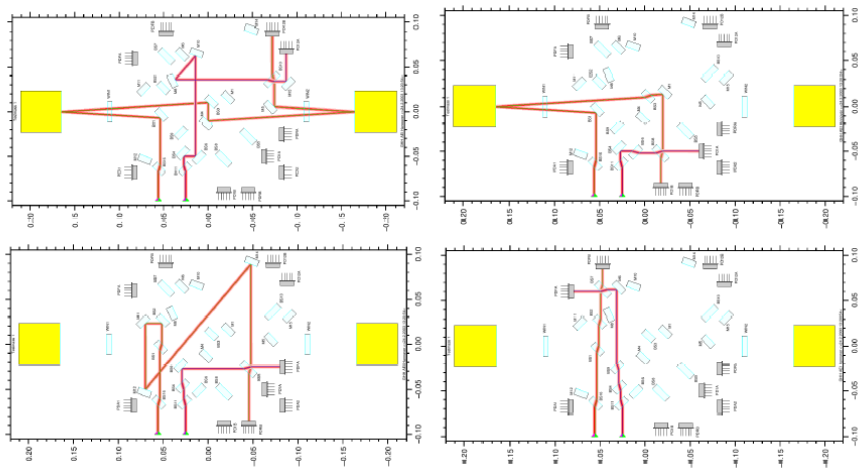

Figure 2.8: From left to right, top to bottom: $x_1 - x_2$ interferometer, x_1 interferometer, reference interferometer, and frequency interferometer. Image obtained from [64].

suspension of TM2, which applied the necessary electrostatic forces by means of the electrodes on the faces of its EH.

- Reference interferometer, whose measurement was subtracted from the other measurements to remove all the perturbations produced outside the OB, since this interferometer was sensitive to them.

- Frequency interferometer, with an arm length mismatch of 38 cm in order to suppress the frequency noise. Its phase was used to stabilise the frequency [42, 68].

The signals from the PDs of each interferometer were sent to the phasemeter. The phasemeter extracted the data at a frequency of 100 Hz and performed a Single Bin Discrete Fourier Transform to measure the phase of the signals at the heterodyne frequency. The phasemeter not only provided the longitudinal phase of the respective interferometers but also provided the angles (in the horizontal and vertical planes) between the wavefront of the

beams that arrived at the PD through the Differential Wavefront Sensing (DWS) technique. There was another different way to measure the angles, the Differential Power Sensing (DPS) technique, that computed the DC angles by subtracting the mean laser power that arrived at one half of the PD to the mean laser power that arrived at the other one half, normalised by the total power on the PD. The DPS technique had a wider dynamic range than the DWS technique, but the latter had better sensitivity [42].

Data and Diagnostics Subsystem

The DDS was composed of heaters, thermistors, magnetometers, coils, the Radiation Monitor (RM), and the Data Management Unit (DMU). So, the objective of this subsystem was to study different perturbations on the LTP coming from several noise sources such as magnetic fields or thermal gradients around the TMs [29, 46, 64], or thermo-elastic movements of the structure as a consequence of thermal expansions or thermal contractions [29, 44, 46, 64–66].

The LTP was equipped with 24 thermal sensors and 14 heaters. By means of the thermal sensors, it has been possible to measure the temperature in different thermally sensitive locations. Heaters were used to inject thermal signals on the places where they were located. Therefore, in addition to measuring the temperature, the LTP carried out several experiments in order to understand the different disturbances that can appear by thermal fluctuations. The reader will find more details on these experiments in the following chapters.

To measure the magnetic field, four fluxgate magnetometers were located surrounding the LTP [34]. Also, by using the coils, several experiments have been carried out in flight to increase the disturbances produced by the magnetic field and, thereby, ease our understanding about these effects and estimate what part of the total acceleration noise between both TMs is due to magnetic-induced forces.

The RM is a charged particle counter. Some particles with more energy of 100 MeV could penetrate until they reached the TMs, charging them. It in turn produced an electric force on them, changing the relative acceleration between both. Several experiments and analysis made during the mission can be found in [19, 20, 24].

Finally, the DMU was the interface which managed most of the scientific instrumentation on the spacecraft. It was the responsible for managing and controlling the DDS. It also handled the acquisition, by means of two Data Acquisition Unit (DAU). In addition, it received the IFO read-outs from the phasemeter and generated the feedback to the laser control system.

On the other hand, the On-Board Computer (OBC) controlled systems such as thrusters, solar array, start tracker, etc. Besides, it was the responsible for processing the GRS data from the FEE and the OMS data from the DMU, being the one that commanded the control signals to the GRSs or thrusters in every moment.

Drag-Free Attitude and Control System

The DFACS [28] had as main objective the dynamic control of the spacecraft so that the one established by Eq. (2.1) was always respected. It worked using sensors and actuators by means of which it was possible to detect disturbances on the TM around which was centred the spacecraft (TM1) in the orbit, and correct deviations of its geodesic trajectory in this orbit using capacitive suspension control and the microNewton thrusters. To be more concrete, above the bandwidth $1\,\text{mHz} < f < 30\,\text{mHz}$ the spacecraft was controlled by the thrusters whereas below that bandwidth, the TM2 followed to the TM1 using capacitive suspension control.

So, the DFACS controlled 15 of the 18 total DOF of the system: 6 DOF for each TM and 3 DOF for the spacecraft —see Figure 2.9. Beside of shield-

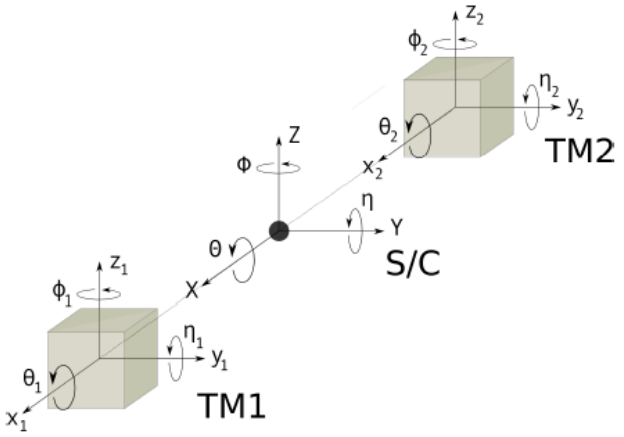

Figure 2.9: LTP reference frame where we can see the axis rotation angles. Image obtained from [46].

ing the TM1 from perturbations on its geodesic trajectory as commented in the previous paragraph, the DFACS also maintained the solar array of the spacecraft pointing to Sun and the communication antenna pointing to Earth.

The DFACS had several modes of operation:

- *Science mode*: The spacecraft and the TM2 (the secondary TM) followed the TM1 in its geodesic. At the same time there were two sub-modes:
  - *Science mode 1.1*: It used the capacitive read-outs in order to sense the movement of the TMs.
  - *Science mode 1.2*: Read-outs (x_1, x_2, η_1, η_2, ϕ_1 and ϕ_2) measured by interferometry (using for the remaining DOF the capacitive sensors) were used to control the positions of the TMs and the spacecraft.
- *Attitude mode*: It controlled the attitude mode of the spacecraft while

the TMs were mechanically caged.

- *Accelerometer mode*: In this mode the movement of the TMs depended on the spacecraft movement since the TMs were caged electrostatically.

- *Normal mode*: In this mode the spacecraft followed to the TM1 and the TM2 in turn followed to the spacecraft using capacitive sensors as motion sensors.

2.3 LISA Pathfinder operations and data analysis

During the operations phase, the communication with the spacecraft was performed via ESA's Estrack ground station network. It sent the information to the Mission Operations Centre (MOC) at the European Science and Operations Centre (ESOC) in Darmstadt (Germany), where data retrieval and conversion were carried out and stored in repositories [88] —see Figure 2.10. Each day had two deliveries, namely: early morning the instrument configuration and evaluation data, and late afternoon the full data set [51, 57].

Everyday there was one team on duty at ESOC to perform quick look and analyse the data, and another team, which had been on duty the previous day, which consolidated its analysis and generated a logbook with the results. In order to analyse the data, the LTP Data Analysis (LTPDA) toolbox, a dedicated MATLAB toolbox, was implemented. It consists of an object-oriented data analysis environment that allows transporting the history of the objects with themselves, easing tracking of them [51, 57]. With scripts developed with this toolbox, it has been possible to perform the analysis almost in real-time of the data obtained during the mission.

As stated previously, the main aim of the mission was to reach the requirement given by Eq. (2.1). In order to do so, the LPF scientific team

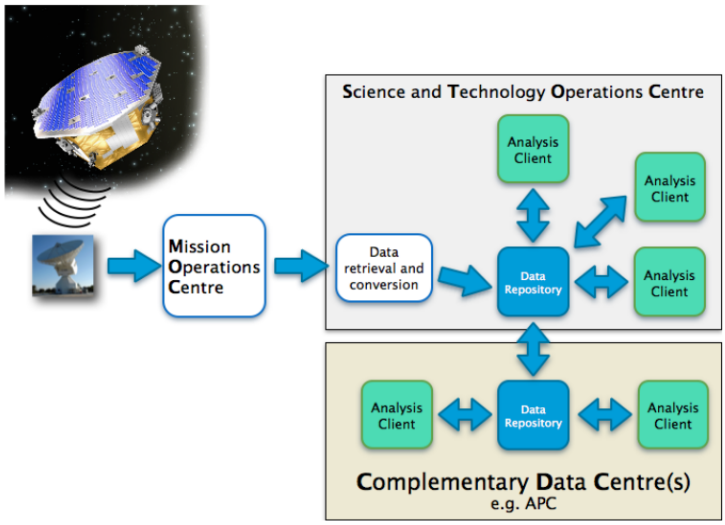

Figure 2.10: Schematic of the science operations scheme and data flow of the ground segment. Image obtained from [16].

carried out several experiments in flight in order to remove all the non-gravitational forces that disturbed the relative acceleration between the TMs in order to get that the system only was susceptible to gravity.

The experiments consisted of stimulating with the different subsystems whatever of the multiple non-gravitational effects. In that sense, we could say that LPF was a laboratory in space. Some of the experiments made during the mission to investigate the disturbances on the TMs were:

- *Acceleration noise measurements*: During long noise runs it was measured the differential acceleration between the TMs in different control modes, stiffness conditions, etc [17, 21].

- *Dynamics system identification experiments*: These were performed to calibrate the dynamic of LPF. Several experiments took place since it was necessary to study the long-term stability of the system as well as

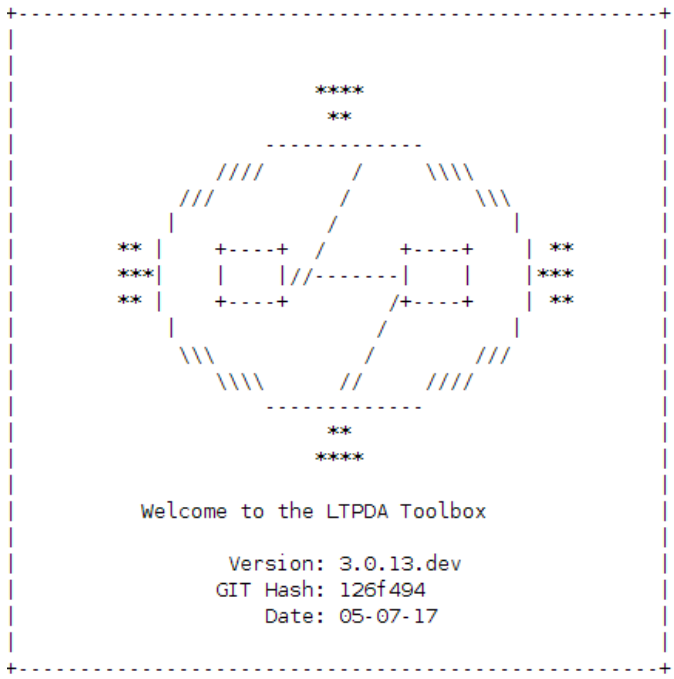

Figure 2.11: LTPDA toolbox logo.

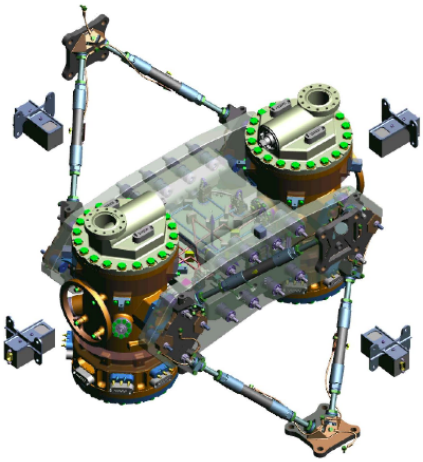

Figure 2.12: Artistic image of the LTP. The circular coils (copper color) are located next to the GRSs and the magnetometers are the grey floating boxes. Image obtained from [34].

estimate and compare the different calibration parameters for different working configurations. By injecting series of sinusoidal signals in critical points, it was possible to estimate these different calibration parameters. Results about this have been published in [23].

- *Cross-talk experiments*: Perturbations in the other DOFs contributed to the dynamic along the x-axis, so it was also necessary to perform several injections of sinusoidal signals to calibrate the parameters that described these couplings.

- *Charge experiments*: In the space, the random arrival of cosmic rays and solar energetic particles penetrated the spacecraft, charging the TMs, which in turn produced electrostatic forces on them. The way to discharge them in LPF was to illuminate with UV light from Mercury vapor lamps and transferred charge by the photo-electric effect. By injecting sinusoidal voltages on the x-axis electrodes, the TM charge was measured. Results about this have been published in [19].

- *Laser frequency noise experiments*: The laser frequency noise was converted into phase shift of the interferometric distance between both TMs. The frequency interferometer measured it, being the signal coming from this interferometer used by a digital nested control loop to stabilise the frequency [42, 68].

- *Laser amplitude noise experiments*: The laser amplitude also had to be stabilised in two frequency ranges. On the one hand, from 1 mHz to 30 mHz, laser power fluctuations produced radiation pressure on the TMs, producing direct forces on them. These fluctuations were suppressed in the phasemeter. On the other hand, the Relative Intensity Noise (RIN) at the heterodyne frequency, roughly 1 kHz, coupled into the phase. This noise contribution could be removed by balance detection [42].

- *Thermal experiments*: Thermal fluctuations in some locations of LPF produced both direct forces on the TMs and coupling with the phase of the interferometric signal. By means of the heaters located on these places we injected thermal signals which produced thermal fluctuations that in turn produced changes in the interferometric differential distance [46, 64].

- *Magnetic experiments*: Magnetic field in the environment of the TMs produced forces on them. By injecting currents with the coils (there were two coils), which were placed as seen in Figure 2.12, we induced magnetic field on the TMs, which produced a magnetic force that changed their positions [34].

2.3.1 Differential acceleration Δg

The main scientific magnitude in LPF was the differential acceleration between both TMs. Taking into account Figure 2.13, we can define this differential acceleration Δg as follows:

$$\Delta g \equiv g_2 - g_1, \tag{2.3}$$

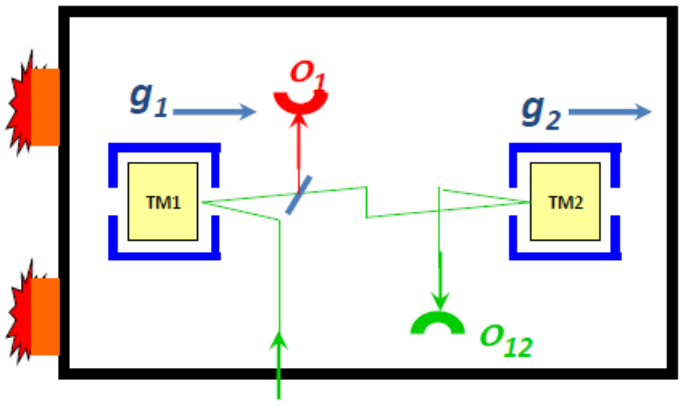

Figure 2.13: Scheme that represents the force per unit mass on each TM, g_1 for TM1 and g_2 for TM2. The differential acceleration between both is the main measurement of the LPF mission. Image obtained from [101].

where $g_1 = F_1/m_{\mathrm{TM}}$ and $g_2 = F_2/m_{\mathrm{TM}}$ are the forces per unit mass on TM1 and TM2 respectively ($m_{\mathrm{TM}} = 1.928 \pm 0.001$ kg).

Now, we are going to consider Newton's equations of motion for each TM:

$$m_{\mathrm{TM}} \cdot \ddot{x}_1(t) = F_1(t) - m_{\mathrm{TM}} \cdot \omega_1^2 \cdot (x_1(t) - x_{\mathrm{SC}}(t)), \tag{2.4}$$

$$m_{\mathrm{TM}} \cdot \ddot{x}_2(t) = F_2(t) - m_{\mathrm{TM}} \cdot \omega_2^2 \cdot (x_2(t) - x_{\mathrm{SC}}(t)) + F_{\mathrm{ES}}(t), \tag{2.5}$$

where $x_1(t)$ and $x_2(t)$ are the displacement of the TM1 and the TM2 with respect to the inertial frame along the x-axis, respectively, $\ddot{x}_1(t)$ and $\ddot{x}_2(t)$ their second derivatives, $x_{\mathrm{SC}}(t)$ is the displacement of the spacecraft, ω_1^2 and ω_2^2 are the total stiffness per unit mass between each TM and the spacecraft, which couple spacecraft motion into force, and, finally, $F_{\mathrm{ES}}(t)$ are all the forces acting on the spacecraft. If we take into account the following interferometer read-outs:

$$o_{12}(t) = x_2(t) - x_1(t) + n_{12}(t), \tag{2.6}$$

$$o_1(t) = x_1(t) - x_{\rm SC}(t) + n_1(t), \tag{2.7}$$

where $o_{12}(t)$ is the read-out associated to the differential position between the TMs, $o_1(t)$ is the read-out associated to the TM1 position, n_{12} is the noise read-out of the interferometer o_{12}, and n_1 is the noise read-out of the interferometer o_1, and we introduce these last four equations in Eq. (2.3), we get:

$$\Delta g(t) \equiv \ddot{o}_{12}(t) - \frac{F_{\rm ES}(t)}{m_{\rm TM}} + \Delta\omega_{12}^2 \cdot o_1(t) + \omega_2^2 \cdot o_{12}(t) - \Delta g(t)_{\rm IFO}, \tag{2.8}$$

where $\Delta\omega_{12}^2 = \omega_2^2 - \omega_1^2$ couples spacecraft motion into Δg and $\Delta g(t)_{\rm IFO} = n_{12}(t) + \Delta\omega_{12}^2 \cdot n_1(t) + \omega_2^2 \cdot n_{12}(t)$ is the interferometer noise.

To extract the calibration parameters, guidance signals were injected into the electrostatic suspension control loop and the drag-free loop. The farmer modulated the relative displacements of TM2 relative to TM1 and to the spacecraft, calibrating ω_2^2, and also introduced relatively large commanded forces, $\frac{F_{\rm ES}(t)}{m_{\rm TM}}$. The latter modulated the relative displacements of the spacecraft relative to TM1, calibrating $\Delta\omega_{12}^2$ [23]. These parameters were evaluated by fitting $\Delta\ddot{o}_{12}$ using the following model [17]:

$$\Delta\ddot{o}_{12}(t) = (1+\lambda)\frac{F_{\rm ES}(t)}{m_{\rm TM}} - \omega_2^2 \cdot o_{12}(t) - \Delta\omega_{12}^2 \cdot o_1(t), \tag{2.9}$$

where λ, ω_2^2 and $\Delta\omega_{12}^2$ are free parameters in the fit.

Besides, we have to take into account that misalignment between the TMs, the sensors, and the spacecraft produced cross-coupling effects, which in turn introduced cross-talk signals in the interferometer read-outs. It generated a bulge in the Δg spectrum from 20 mHz to 200 mHz [17]. The subtraction of this effect can be made by fitting the following model to the measured acceleration noise [23]:

$$\delta g_{\rm cross-talk} = C_1\ddot{\bar{\phi}}(t) + C_2\ddot{\bar{\eta}}(t) + C_3\ddot{\bar{y}}(t) + C_4\ddot{\bar{z}}(t) + C_5\bar{y}(t) + C_6\bar{z}(t), \tag{2.10}$$

where $\bar{()}$ denotes the mean displacement or rotation of both TMs along the given coordinate: ϕ, η, y or z —see Figure 2.9. However, although the model subtracts the "bump", the C_i parameters do not give us much information about the underlying physical processes of cross-coupling of the system. The work for a deeper understanding is still in progress [97].

Finally, it is necessary to make other correction, $g_{\rm rot}$, since LPF was a rotating reference frame that introduced inertial forces along the x-axis. There were two types of these forces: centrifugal forces due to the spacecraft angular velocity (Ω) with respect the reference frame, and Euler forces due to a non-zero spacecraft rotational acceleration ($\dot{\Omega}$) [23].

Hence, the LPF observable, for the differential force per unit mass relevant to the LISA TM acceleration, taking into account both the cross-coupling effects and the contributions of the inertial forces will be given by [21, 23]:

$$\Delta g(t) \equiv \ddot{o}_{12}(t) - \frac{F_{\rm ES}(t)}{m_{\rm TM}} + \Delta\omega_{12}^2 \cdot o_1(t) + \omega_2^2 \cdot o_{12}(t) - \Delta g(t)_{\rm IFO} - \delta g_{\rm cross-talk} - g_{\rm rot}. \tag{2.11}$$

2.3.2 LISA Pathfinder results on free fall

The first results of LPF were published in June 2016 [17]. In this paper, the measurements carried out for 6.5 days (April 2016) starting 127 Days After Launch (DAL) are presented. Figure 2.14 shows the Amplitude Spectral Density (ASD) of Δg, averaging 26 periodograms of 40000 s each, using a 50% overlapping data and a Blackmann-Harris spectral window (Welchs averaged periodogram method [95]), with the first four frequency bins of the averaged periodogram discarded. It produces a relative error of 1σ of 10% in $S_{\Delta g}^{1/2}$, with an effective spectral resolution of $\pm 50\,\mu$Hz.

As seen in Figure 2.14, from 0.7 mHz until 10 mHz, the LPF require-

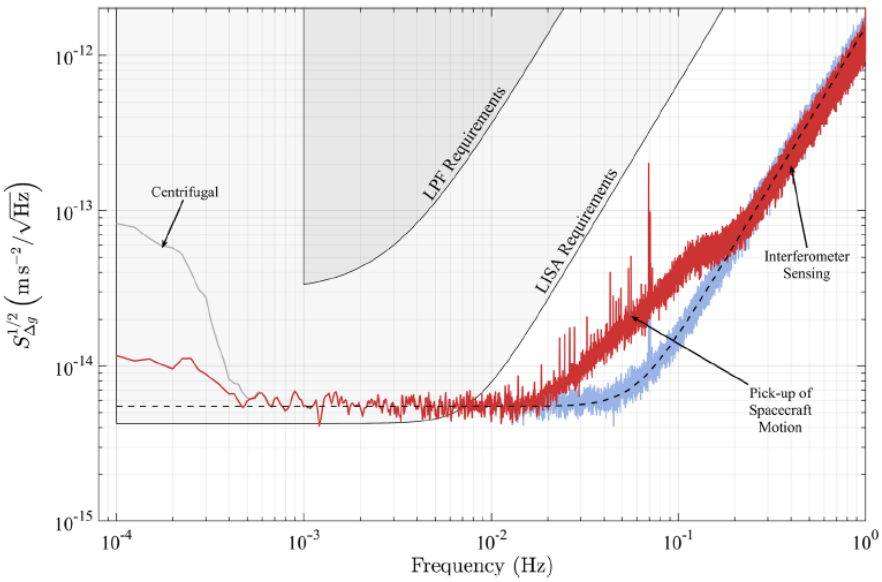

Figure 2.14: *Shaded areas*: LISA and LISA Pathfinder requirements. *Gray curve*: ASD for Δg. *Red curve*: ASD of the same time series as the one used to obtain the gray curve after the correction of the centrifugal force. *Blue curve*: ASD after the correction for the pickup of spacecraft motion by the interferometer (IFO). *Dashed black line*: $S_{\Delta g}(f) = S_0 + S_{\mathrm{IFO}}(2\pi f)^4(f)$, being $S_0^{1/2} = (5.57 \pm 0.04)\ \mathrm{fm\ s^{-2}}/\sqrt{\mathrm{Hz}}$ and $S_{\mathrm{IFO}}^{1/2} = (34.8 \pm 0.3)\ \mathrm{fm}/\sqrt{\mathrm{Hz}}$. Image obtained from [17].

ment was improved, $S_{\Delta g}^{1/2}$ is a factor 5 below the requirement. Regarding the LISA requirement, $S_{\Delta g}^{1/2}$ is below it at frequencies higher than 10 mHz and is above the requirement for frequencies between 0.5 mHz and 10 mHz but only a factor 1.4.

The classical definition for Δg (Eq. (2.8)) has been used to compute its ASD, obtaining the gray line in Figure 2.14. It was corrected by suppressing two effects: the pickup of the noisy spacecraft motion in the o_{12} interferometric read-out, that appears as a bulge from 20 mHz to 200 mHz; and the centrifugal force produced by the spacecraft rotation, whose y and z components also introduce a noise in o_{12}, which appears in the spectrum below 0.5 mHz. The blue line is obtained by subtracting both effects.

Looking at Figure 2.14 we distinguish three parts in the spectrum, each of which is dominated by different physical mechanisms:

- *Brownian noise*, noise that appears as a consequence of residual gas inside the EHs whose particles damp the TM motion. It is a nearly frequency-independent noise, being its contribution:

$$S_0^{1/2} = (5.57 \pm 0.04)\ \mathrm{fm\,s^{-2}}/\sqrt{\mathrm{Hz}}. \tag{2.12}$$

  This noise depends on the internal pressure within the EH in such a way that it decreased throughout the mission as a consequence of gas venting into space with the vacuum subsystem [32]. Brownian noise dominates in the frequency range from 0.7 mHz to 20 mHz.

- *Interferometer read-out noise*, noise that dominates at frequencies higher than 60 mHz. It contributes as $S_{\mathrm{IFO}}^{1/2}(2\pi f)^2$ [49, 50], where:

$$S_{\mathrm{IFO}}^{1/2} = (34.8 \pm 0.3)\ \mathrm{fm\,s^{-2}}/\sqrt{\mathrm{Hz}}. \tag{2.13}$$

- At frequencies lower than 0.5 mHz, we observe an increase of the noise when the frequency decreases, which got lower over time, as we can

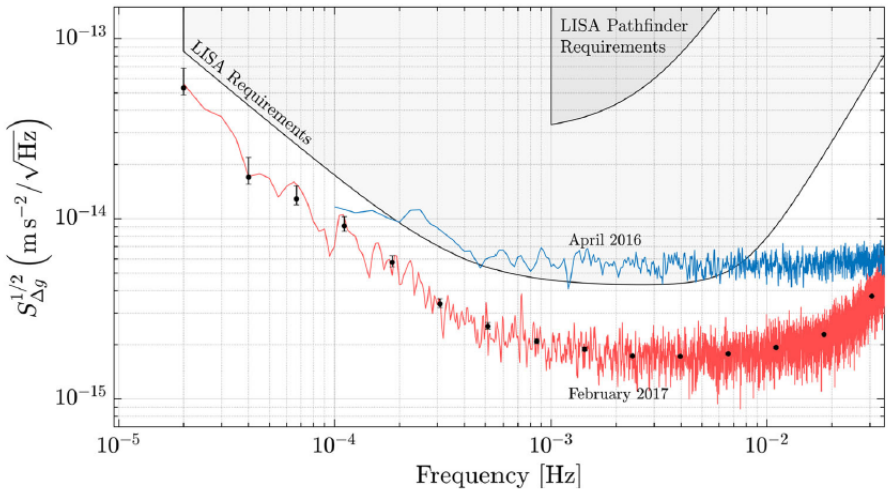

Figure 2.15: *Shaded areas*: LISA and LISA Pathfinder requirements. *Blue curve*: ASD for Δg that corresponds to the blue line in Figure 2.14. *Red curve*: ASD for Δg obtained during noise measurements in February 2017, during the extension phase. Image obtained from [21].

observe in Figure 2.15 [21]. The reason of this tail is still under study.

In Figure 2.15 we can see the best measurement achieved during the mission, which was published in February 2018 [21]. This figure shows the ASD of Δg (red curve) —see Eq. (2.11)— measured for 13 days (February 2017) at a temperature of 11°C, averaging 10 periodograms of 2×10^5 s each, using a 50% overlapping data and a Blackmann-Harris spectral window (Welchs averaged periodogram method [95]), with the first four frequency bins of the averaged periodogram discarded. In addition, the ASD was also estimated using other method which uses Bayesian inference (black points with error bars), that allows to modify the length of the periodograms for each of the selected frequencies, getting more precision [22]. The blue curve is the blue curve in Figure 2.14.

Comparing both curves, the first thing we observe is that the curve

obtained for the second noise run is below the other one. The ASD for the range of frequency from 1 mHz to 10 mHz is a factor 3 lower than the ASD for the first noise run (April 2016). The cooling down carried out during the second noise run when we passed from the $22\,^{o}\mathrm{C} - 23\,^{o}\mathrm{C}$ range to the $11\,^{o}\mathrm{C} - 12\,^{o}\mathrm{C}$ range, together with the evacuation of residual gas by the vacuum system, reduced the pressure inside the EHs (roughly a factor 10 since the beginning of operations). It also in turn reduced the Brownian noise. As seen in Figure 2.15, for the new line:

$$S_0^{1/2} = (1.74 \pm 0.05)\,\mathrm{fm\,s^{-2}}/\sqrt{\mathrm{Hz}}. \tag{2.14}$$

On the other side, there is an increase of the interferometer read-out noise in the ASD obtained in February 2017. We passed from $35\,\mathrm{fm}/\sqrt{Hz}$ (April 2016) to $100\,\mathrm{fm}/\sqrt{\mathrm{Hz}}$ (February 2017). It was due to the change of the positions of the TMs and attitude control points, hence, there was no an intrinsic increase of the interferometer noise.

By increasing the duration of the noise runs, it reaches frequencies down $20\,\mu$Hz. From 1 mHz to lower frequencies, we see how the ASD rises with decreasing frequency as seen before for the April 2016 case, but now we are below the requirements of LISA Pathfinder and LISA. This improvement was obtained because of two reasons, namely a more accurate calculation of the actuation force, and the identification of another inertial force from the LPF spacecraft rotation, both subtracted —see Eq. (2.11). However, as commented before, there is an excess noise in the low-frequency tail that is currently being investigated.

Chapter 3

Thermal effects and thermal diagnostics subsystem in LISA Pathfinder

Enabling a new observing window in the gravitational sky requires facing new technological challenges. The coupling of low-frequency temperature perturbations to instrument performance is one of these challenges. Indeed, temperature fluctuations will play an important role in space-borne gravitational detectors since typically their most significant contribution is in the low-frequency (sub-milliHertz) part of the measurement window where temperature-driven effects may even limit the overall instrument sensitivity. Moreover, at such time-scales —temperature changes that can last for hours— they are ubiquitous to the satellite with a potential to impact different stages and subsystems of the measuring chain, e.g. thermally-induced forces [31] acting on the GRS [36], temperature-induced path-length variations [44, 65, 66] in the OMS [50], and thermal effects in all associated electronics.

Unlike most space missions, where the satellite house-keeping system is in charge of monitoring the environment, LPF included a precision diagnostics subsystem [29] designed with a two-fold objective. First, to monitor

noise disturbances and, second, to study the contribution of these disturbances to the instrument noise budget. The diagnostics subsystem was composed of sensors (magnetometers, temperature sensors, and a particle counter) and actuators (heaters and coils). The latter were used to induce controlled perturbations, which allowed to derive coupling factors and transfer functions between thermal and magnetic perturbations and the outputs of the GRSs and the OMS.

In this chapter we will see the different thermal effects that can couple into differential acceleration measurements as well as the thermal diagnostics subsystem which was used to evaluate these contributions.

3.1 Thermal effects

We have commented that we can distinguish two kinds of temperature-induced effects depending on whether they produce direct forces on the TMs or path-length variations. The former appears as a consequence of thermal gradient fluctuations on the EHs, while the latter appears because of thermal fluctuations on the mechanical structure (thermo-elastic contributions) and on optical components such as the OWs (thermo-optical contributions).

3.1.1 Thermal effects inside the Gravitational Reference Sensor

As stated above, thermal gradient fluctuations in the EHs produce direct forces (and torques) on the TMs which in turn modify the differential acceleration between both. In addition, there are effects that depend on changes in the absolute temperature, such as the Brownian noise.

Radiation pressure effect

According to the electromagnetic theory, considering the case of an infinite plate, the pressure exerted by the radiation coming from a surface at an

absolute temperature T on another surface is given by [31, 46, 64]:

$$P_{\mathrm{rp}} = \frac{2}{3}\frac{\sigma}{c}T^4, \tag{3.1}$$

where $\sigma = 5.67 \cdot 10^{-8}\,\mathrm{W\,m^{-2}\,K^{-4}}$ is the Stefan-Boltzmann constant, c is the speed of light, and the factor $\frac{2}{3}$ comes from the projection of the radiation flux contribution on the perpendicular direction to the surface. Therefore, if there are thermal gradient fluctuations around the TMs, as a consequence of this pressure, there will be a net force on it. By using Eq. (3.1) we obtain that the difference of pressure between the sides of the TMs in the direction where the thermal gradient appears is:

$$\Delta P_{\mathrm{rp}} = \frac{8}{3}\frac{\sigma}{c}\kappa_{\mathrm{rp}}T^3\Delta T, \tag{3.2}$$

where κ_{rp} is a factor that includes the optical properties of the surfaces involved and their geometries, whose value, for the case of the high reflectivity surfaces, is 0.32 [31]. Multiplying Eq. (3.2) by the TM surface area, A_{TM}, we have that the force exerted on the TM is:

$$F_{\mathrm{rp}} = \frac{8}{3}\frac{\sigma}{c}\kappa_{\mathrm{rp}}A_{\mathrm{TM}}T^3\Delta T, \tag{3.3}$$

$$\alpha_{\mathrm{rp}} = \frac{F_{\mathrm{rp}}}{\Delta T} = \frac{8}{3}\frac{\sigma}{c}\kappa_{\mathrm{rp}}A_{\mathrm{TM}}T^3. \tag{3.4}$$

On-ground experiments with torsion pendulums lead to an estimate of this effect for the LPF geometry given by [31]:

$$\alpha_{\mathrm{rp}} = 27\kappa_{\mathrm{rp}}\ \mathrm{pN/K}. \tag{3.5}$$

Radiometer effect

Crookes's light mill radiometer is based on this effect, which appears in rarefied environments where the gas particles have a mean free path longer than the dimensions of the containing vessel, as inside the EH. In this case,

the equilibrium conditions are given when [31, 46, 64]:

$$\frac{P_1}{\sqrt{T_1}} = \frac{P_2}{\sqrt{T_2}}, \tag{3.6}$$

where P_1 and T_1 are the pressure and the temperature in one side of the EH, and P_2 and T_2 the pressure and the temperature in the opposite side. In the presence of thermal gradient fluctuations, a net force appears acting on the TM such as follows:

$$F_{\mathrm{r}} = \kappa_{\mathrm{r}} \frac{A_{\mathrm{TM}} P}{4T} \Delta T, \tag{3.7}$$

$$\alpha_{\mathrm{r}} = \frac{F_{\mathrm{r}}}{\Delta T} = \kappa_{\mathrm{r}} \frac{A_{\mathrm{TM}} P}{4T}, \tag{3.8}$$

where P and T are the pressure and the temperature for a particle reservoir, A_{TM} is the TM surface area, κ_{r} is a geometrical factor, and ΔT is the thermal gradient between both opposite internal sides of the EH.

As in the previous case, on-ground experiments with torsion pendulums lead to an estimate of this effect given by [31]:

$$\alpha_{\mathrm{r}} = 18 \kappa_{\mathrm{r}} \text{ pN/K}, \tag{3.9}$$

at 10^{-5} Pa and 293 K. In this paper appears that the value for κ_{r} is 1.25 for the LPF case.

The radiometer effect depends on the pressure, being the only effect that has a dependence on it. This allowed to estimate the Brownian noise inside the EHs, that is the dominant effect in the flat part of the differential acceleration spectrum, as seen in Section 2.3.2.

Outgassing effect

The absorption of molecules by the surfaces of a closed system as the GRS produces an increase of the pressure around the TM. Furthermore, an asymmetry in the molecular outflow can appear by temperature of the outgassing, which in turn couples into differential pressure. Besides the temperature, asymmetric outgassing also depends on the type of particles we have.

The outgassing rate can be modelled as [31, 46, 64]:

$$Q(T) = Q_0 e^{-\frac{\Theta_{\mathrm{og}}}{T}}, \tag{3.10}$$

where Q_0 is a flow prefactor and Θ_{og} the activation temperature of the molecular species that we are considering. As seen, Eq. (3.10) depends on the molecular species under consideration, but if we take into account averaged values for all these species, we can approximate the pressure gradient that appears as a consequence of the different outgassing rates at both side of the TMs as:

$$\Delta P = \frac{Q(T)}{T^2}\frac{\Theta_{\mathrm{og}}}{C_{\mathrm{eff}}}\Delta T, \tag{3.11}$$

where C_{eff} is a geometrical factor resulting from a combination of the conductance of the paths around the TM and through the EH venting holes [31]. Multiplying by the TM surface area we get the following force coming from this effect:

$$F_{\mathrm{og}} = A_{\mathrm{TM}}\frac{Q(T)}{T^2}\frac{\Theta_{\mathrm{og}}}{C_{\mathrm{eff}}}\Delta T, \tag{3.12}$$

$$\alpha_{\mathrm{og}} = \frac{F_{\mathrm{og}}}{\Delta T} = A_{\mathrm{TM}}\frac{Q(T)}{T^2}\frac{\Theta_{\mathrm{og}}}{C_{\mathrm{eff}}}. \tag{3.13}$$

An estimate for this contribution has been obtained by means of on-ground experiments with torsion pendulums [31]:

$$\alpha_{\mathrm{og}} = 40\ \mathrm{pN/K}, \tag{3.14}$$

where a value of $\Theta_{\mathrm{og}} = 30000\ \mathrm{K}$ has been taken into account.

Total thermal gradient noise contribution

Once we have seen all the thermal gradient contributions, we can consider the following equation which contains all this information [31, 46, 64]:

$$S_F^{1/2}(\omega) = A_{\mathrm{TM}}[\frac{8}{3}\frac{\sigma}{c}\kappa_{\mathrm{rp}}T^3 + \kappa_{\mathrm{r}}\frac{P}{4T} + \frac{Q(T)}{T^2}\frac{\Theta_{\mathrm{og}}}{C_{\mathrm{eff}}}]S_{\Delta T}^{1/2}(\omega). \tag{3.15}$$

Considering the values obtained for each contribution in [31], the total contribution would be $\approx 70\,\mathrm{pN/K}$.

Apart from these main three contributions related to the thermal gradients inside the EHs, there were other thermal noise sources [46, 64] such as the TM surface reflectivity reduction over time, which in turn produced a reduction of the radiation absorbed by the TM, or the thermal expansion of the housing, which changed the relative position between the electrodes and the TMs, which in turn changed the distance read-outs.

Brownian noise

As stated in Section 2.3.2, Brownian noise appears as a consequence of residual gas inside the EHs whose particles damp the TM motion. The fluctuation-dissipation theorem [30] states that the fluctuations produced in a system with dissipation can be represented by a force, whose noise will be given by [32]:

$$S_F(\omega) = 4kTRe[Z(\omega)], \tag{3.16}$$

where k is the Boltzmann constant, T is the temperature of the system, and $Re[Z(\omega)]$ is the real part of the mechanical impedance of the system. With on-ground experiments with torsion pendulums, it has been estimated, for a system like LPF and based on Eq. (3.16), that the acceleration noise that comes from the Brownian noise depends on pressure as follows [32]:

$$S_{\mathrm{a,Brownian}}^{1/2} = 1.3 \cdot 10^{-15}(\frac{P}{10^{-6}\,\mathrm{Pa}})^{1/2}\,\mathrm{m\,s^{-2}\,Hz^{-1/2}}. \tag{3.17}$$

This noise dominated the milliHertz range of the spectrum of the differential acceleration and decreased with time by ejecting residual gas via the vacuum system. In Section 2.3.2 was commented that during the long noise run in February 2017, where the system was cooled down, the part of the differential acceleration spectrum dominated by Brownian noise reached a value of $(1.74 \pm 0.05)\,\mathrm{fm\,s^{-2}}/\sqrt{\mathrm{Hz}}$.

3.1.2 Thermal effects on the Optical Metrology Subsystem

We have described the thermal effects inside the GRS that produced real forces on the TMs. Now we are going to see the thermo-optical and thermo-elastic effects that coupled into phase shift of the interferometric read-out producing the actuation of the control system although there were no real forces on the TMs.

Thermo-optical effects induced path-length variations

Several optical elements were integrated as a part of the optical subsystem, all of them susceptible to temperature-dependent effects with a potential impact on the instrument performance. However, the dominant contribution from temperature-dependent effects came from the two OWs. These plane parallel elements acted as the optical interface between the OB and the clean volume inside the vacuum enclosure. Their sensitivity to temperature relies in the fact that, opposite to the rest of elements, the OW were not bounded to the OB by hydroxy-catalysis [80, 81] but clamped in a Titanium flange.

As described in the following, two different kinds of thermal effects have been identified as sources of changes in the optical path length of a light beam traversing a plane-parallel piece of glass as the ones in the OWs [64, 65]:

- *Temperature-induced change of the refractive index*: The first effect is

quantified by the expression

$$\frac{ds}{dT} = \frac{2\pi L}{\lambda}\,[\frac{dn}{dT} + (n-1)\alpha_{\mathrm{E}}], \tag{3.18}$$

which describes the path-length variation of a beam of light traversing a glass slab of thickness L and (nominal) refractive index n; λ is the wavelength of the used light, and α_{E} is the linear thermal expansion factor of the glass, $\alpha_{\mathrm{E}} = L^{-1}\, dL/dT$.

The ds/dT effect is most prominent at very low frequencies and DC. The reason is that it happens even if the temperature of the window is homogeneous, and without mechanical stresses. The latter is most associated with rapid temperature increases that, introducing gradients across the window, can produce variations in the path length through birefringence, as we discuss in the following point.

The ds/dT effect has been measured on OW samples in the laboratory with a result of 25 mrad/K ($\approx 4.25 \cdot 10^{-9}$ m/K) [43, 64], a figure very well matching the one given by estimates if data-sheet properties of the OHARA S-PHM52 glass used in the experiment are used to calculate the path-length variations in the OW glass due to changes in the refractive index [43].

- *Thermo-mechanically-induced change of the refractive index*: A laser beam can also experience a path-length change due to mechanical stress. This effect is relevant for the OW since the glass is clamped by a Titanium flange to the vacuum enclosure and, therefore, subjected to stress because of the differing thermal expansion coefficients of the glass and the metal. Stress-related effects on the laser phase are difficult to measure and model. Even though an expression can be derived for the particular geometry of the OW by assuming an equilibrium between glass and metal forces —see Figure 3.1. The

strain on the window can then be expressed in terms of the thermo-mechanical properties of Titanium and glass and the temperatures in both, leading to [86]:

$$\sigma_{\text{Glass}} = \frac{\alpha_{\text{Ti}}\Delta T_{\text{Ti}} - \alpha_{\text{Glass}}\Delta T_{\text{Glass}}}{E_{\text{Ti}}^{-1} + (h/r)\, E_{\text{Glass}}^{-1}}, \tag{3.19}$$

where α is the linear thermal expansion factor, E is the Young modulus, h is the wide of the Titanium ring edge, and r the radius of the window glass.

Following the previous derivation, we can distinguish two different ranges: the *low-frequency* (LF) range and the *high-frequency* (HF) range. The first corresponds to long-duration thermal fluctuations on the Titanium flange, actually long enough that the temperatures of the glass and the Titanium equal each other, or $\Delta T_{\text{Ti}} = \Delta T_{\text{Glass}} \equiv \Delta T$. In this case, and taking into account Eq. (3.19), the stress-based contribution to the ds/dT effect is given by

$$\left.\frac{d\phi}{dT}\right|_{\text{LF}} = \beta \frac{2\pi d}{\lambda_{\text{laser}}} \frac{\alpha_{\text{Ti}} - \alpha_{\text{Glass}}}{E_{\text{Ti}}^{-1} + (h/r)\, E_{\text{Glass}}^{-1}}. \tag{3.20}$$

On the opposite, when the thermal fluctuations are fast enough to induce a temperature increase in the Titanium but not in the glass, we consider $\Delta T \equiv \Delta T_{\text{Ti}} \gg \Delta T_{\text{Glass}}$ and therefore we obtain an equivalent expression for the high frequency expressed as

$$\left.\frac{d\phi}{dT}\right|_{\text{HF}} = \beta \frac{2\pi d}{\lambda_{\text{laser}}} \frac{\alpha_{\text{Ti}}}{E_{\text{Ti}}^{-1} + (h/r)\, E_{\text{Glass}}^{-1}}. \tag{3.21}$$

Estimates using data-sheet values provide a contribution of 2.5 mrad/K ($\approx 4.25 \cdot 10^{-10}$ m/K) for the low-frequency contribution and 15 mrad/K ($\approx 2.5 \cdot 10^{-9}$ m/K) for the high-frequency one [64, 65].

From the two previously described effects, it is possible to conclude that

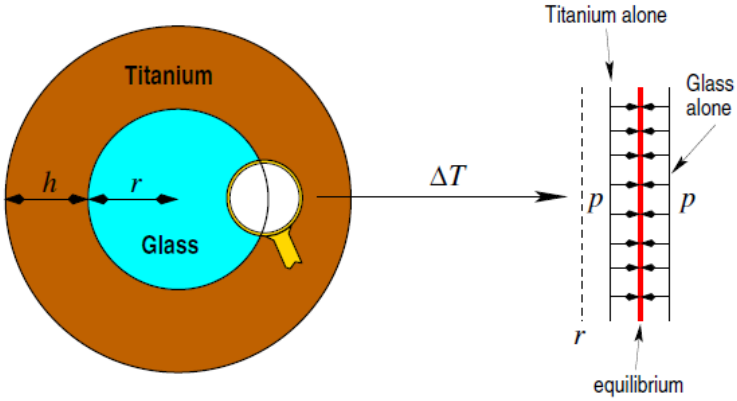

Figure 3.1: Scheme of the mechanical stress exerted between the glass and the Titanium flange. Image obtained from [65].

the ds/dT response due to the OW consists on a transfer function dominated at low frequencies by the dn/dT contribution while effects originated on stress only show up in the higher frequency band.

Thermo-elastic effects induced path-length variations

Mechanical relaxation mechanisms –creep-like effects– are unavoidable in a complex structure as the one onboard LPF. Their impact are sudden glitches in the time series that need to be identified and, when possible, extracted from the data.

Although appearing in the main measurement onboard, these effects are not a major impact in low-frequency GW detectors since they are high-frequency events. Instead, if the structural distortion is driven by environmental temperature fluctuations, low-frequency temperature perturbations can leak in the instrument frequency band as displacement noise.

A natural candidate for this noise source were suspension struts —see Figure 3.2. These were Carbon Fiber Reinforced Polymer (CFRP) elements

with two Titanium end fittings that held the main instrument composite –GRSs and OB– inside the thermal shield, isolating the main instrument from external temperature fluctuations. Suspension struts were also the thermal link from the main instrument to the satellite, hence the main path from intrinsic satellite temperature fluctuations to the core instrument.

Thermo-elastically-induced effects by the suspension struts were already studied during on-ground validation. During those campaigns thermal loads were injected by means of heaters attached to the struts [44]. The results showed a coupling of 1 pm/K from temperature in the struts to longitudinal displacement between TMs.

On the other hand, thermo-elastic distortions were also produced when there was relative movement between the GRSs and the OB, which implied a change on the stiffness forces that acted on the TMs, but in this case, this movement produced real forces on the TMs, not just path-length variations —see Chapter 5.

3.2 Thermal diagnostics subsystem

In order to measure the temperature in different positions of the spacecraft as well as estimate the level of noise introduced by the thermal effects described in Section 3.1, the LTP was equipped with 24 thermal sensors and 14 heaters distributed as follows: two heaters and two sensors for each $\pm x$ side of each EH, two heaters and three sensors on the Titanium flange of each OW, one heater and one sensor on six of the eight struts, and four sensors on the edges of the OB. Using thermal sensors, the temperature in different locations was measured, and using heaters, thermal signals were injected in critical positions to stimulate the thermal effects described in Section 3.1. In Figure 3.3 and Figure 3.4 we can see the distribution of thermal sensors and heaters of the thermal diagnostics subsystem.

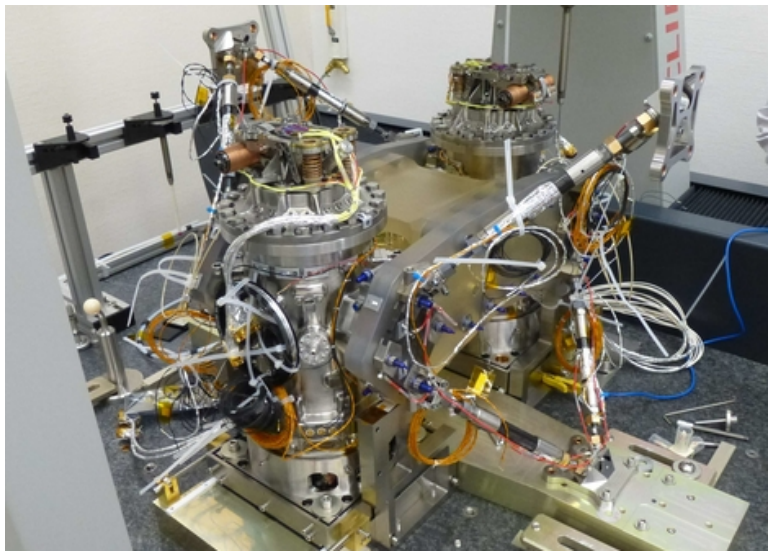

Figure 3.2: Real picture of the LTP with the struts which held the LTP inside the LCA. Image obtained from [92].

The satellite also included sensors for each of the different units in the platform. These were located outside the thermal shield containing the instrument and were primarily for monitoring unit health so had a less stringent requirement in terms of precision or stability than the sensors of the temperature diagnostics subsystem. They are however indicative of the thermal fluctuations of the electronic units and, hence, useful as a reference of the temperature environment surrounding the instrument. In Figure 3.5 we can see the distribution of thermal sensors on the thermal shield.

3.2.1 Thermal sensors

The requirement for the frequency range from 1 mHz to 30 mHz was set to $10^{-5}\,\mathrm{K\,Hz^{-1/2}}$. Negative Temperature Coefficient (NTC) sensors (Betatherm G10K4D372) with a nominal resistance of $10\,\mathrm{k\Omega}$ and operational range $7.7\,^{\mathrm{o}}\mathrm{C} - 32\,^{\mathrm{o}}\mathrm{C}$ were tested and, finally, chosen to go onboard [63, 74].

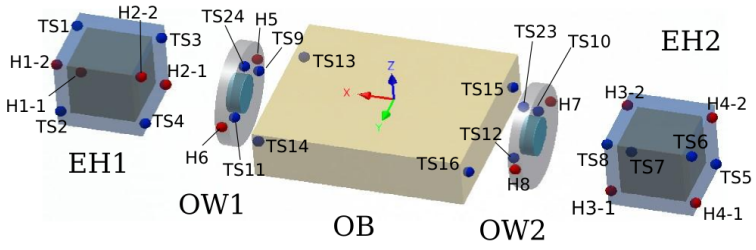

Figure 3.3: Schematic of the thermal sensors and heaters on the LTP. Image obtained from [25].

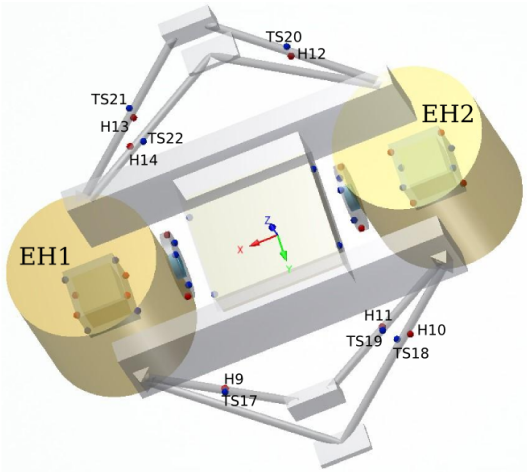

Figure 3.4: Schematic of the thermal sensors and heaters on the struts. Image obtained from [25].

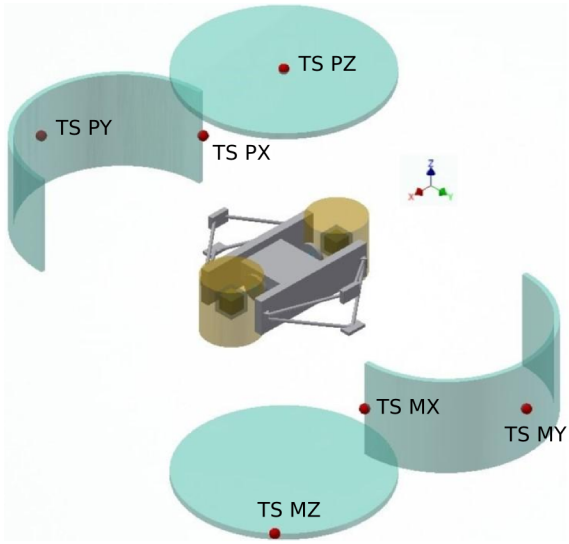

Figure 3.5: Schematic of the thermal sensors on the LCA. Image obtained from [25].

By means of demagnetization procedures, any effect coming from the magnetization remaining in the materials of the thermistors was eliminated [75]. NTC sensors have an accuracy of $\pm 0.5\,\mathrm{K}$ in the absolute temperature measurement.

In addition, the dissipated power in the thermal sensors was limited to $10\,\mu\mathrm{W}$ in order to prevent thermal effects on locations where the sensors were attached and avoid self-heating errors in the sensor.

The principle of measurement was based on the Wheatstone Bridge (WB) measurement of a resistance [63, 74]. The idea is to measure the resistance by estimating how the voltage falls between both sides of the bridge.

To maximise the sensitivity, six scales were defined with center temper-

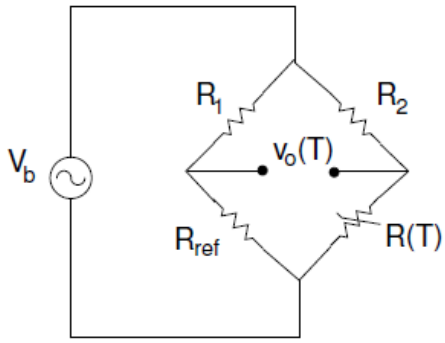

Figure 3.6: Schematic of a WB scheme, where $R(T)$ is the resistiance of the sensor, R_{ref} is an array of resistors that determines the centre of the temperature scale in the absolute measurements, and R_1 and R_2 are fixed resistances. Image obtained from [63].

atures 12 °C, 15 °C, 20 °C, 22.5 °C, 25 °C, and 27.5 °C, which, at the same time, kept the output voltage of the bridge close to zero.

The output voltage of the WB was sampled by the Analog-to-Digital Converter (ADC) which provided 8000 initial samples accumulated into a 32-bit signed integer value (4000 positives and 4000 negatives), D_{acc}.

D_{acc} and the temperature scale were sent to ground for each thermal sensor, and, once there, the ADC converted D_{acc} to counts [46, 61, 63]:

$$C_{\text{ADC}} = \frac{D_{\text{acc}}}{8000}. \tag{3.22}$$

So, taking into account the 10 V scale range of the 16-bit ADC, the voltage measured is given by:

$$V_0 = \frac{10}{2^{16}} C_{\text{ADC}}. \tag{3.23}$$

Temperature scale	$R_{\rm ref}(\Omega)$
0	ref0=17500
1	ref1=15000
2	ref2=12500
3	ref3=11000
4	ref4=10000
5	ref5=9000

Table 3.1: Temperature scale to $R_{\rm ref}$.

With this, the NTC resistance is expressed as:

$$R_{\rm out} = \frac{R}{\frac{1}{\frac{V_0}{GV_{\rm b}}+\frac{R_{\rm ref}}{R+R_{\rm ref}}} - 1}, \tag{3.24}$$

where $R = 10\,{\rm k}\Omega$, $V_{\rm b} = 0.6201\,{\rm V}$ is the WB voltage supply, $G = 198.6$ is the gain of the instrumentation amplifier, and $R_{\rm ref}$ is the resistance associated to the current scale —see Table 3.1.

Finally, by means of the Steinhart-Hart formula, $R_{\rm out}$ is converted to temperature (in $^{\rm o}$C) as follows:

$$T_{\rm NTC,TSa} = \frac{1}{\alpha + \beta ln R_{\rm out} + \gamma ln^3 R_{\rm out}} - 273.15, \tag{3.25}$$

where the characteristic coefficients obtained by a dedicated calibration are [46, 61, 73]:

$$\alpha = 0.00114209584913\,{\rm k}^{-1}$$

$$\beta = 0.000219282310365\,{\rm k}^{-1}$$

$$\gamma = 0.000000240184960\,{\rm k}^{-1}$$

Changes in temperature scales produced spikes in the read-out as a consequence of the different zero in each temperature scale. These spikes only appeared during phases of high-temperature drifts, for example tem-

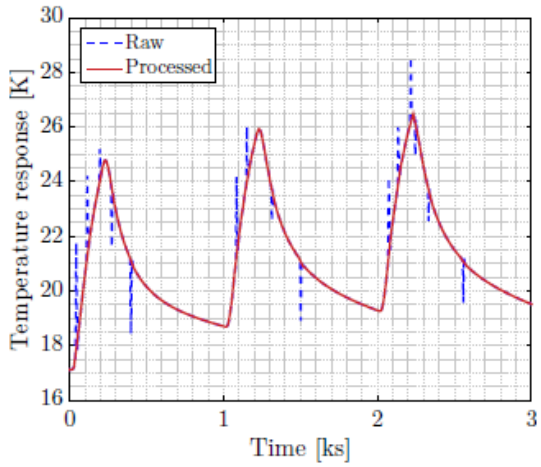

Figure 3.7: Thermal measurement with spikes (blue dashed line) and without spikes once post-processing was performed. Image obtained from [46].

perature experiments or changes in the spacecraft configuration, and never during phases of scientific runs where the instrument was kept unperturbed to achieve the highest degree of free fall. The spikes were suppressed from the time series by means of data analysis post-processing.

In addition to the absolute temperature measurements, two other measurements were performed, namely differential temperatures and reference temperatures.

- *Differential temperature measurements*: They were obtained by substituting R_{ref} by another thermal sensor in such a way that the environment temperature fluctuation was removed. The differential temperature is defined as [61]:

$$\delta T_{\text{NTC,ab}} \doteq T_{\text{NTC,TSa}} - T_{\text{NTC,TSb}}, \tag{3.26}$$

being $T_{\text{NTC,TSb}}$ the temperature for the sensor b. To obtain this tem-

perature, it is necessary to introduce the following resistance [61]:

$$R_{\mathrm{out,TSb}} = \frac{R[(GV_{\mathrm{b}} - V_0)e^{(x_{\mathrm{a}}-y_{\mathrm{a}}/2)^{1/3}-(x_{\mathrm{a}}+y_{\mathrm{a}}/2)^{1/3}} - V_0 R]}{R(GV_{\mathrm{b}} + V_0) + V_0 e^{(x_{\mathrm{a}}-y_{\mathrm{a}}/2)^{1/3}-(x_{\mathrm{a}}+y_{\mathrm{a}}/2)^{1/3}}}, \tag{3.27}$$

$$y_{\mathrm{a}} = \frac{\alpha - \frac{1}{T_{\mathrm{NTC,TSa}}}}{\gamma}, \tag{3.28}$$

$$x_{\mathrm{a}} = \sqrt{(\beta/3\gamma)^3 + y_{\mathrm{a}}^2/4}, \tag{3.29}$$

in Eq. (3.25), in this case for the sensor b. Introducing the result in Eq. (3.26), the differential measurement is obtained.

- *Reference temperature measurements*: Reference measurements are calculated like the absolute ones described above, but changing the thermistor in the WB by a high-stability resistances that do not vary with temperature. Hence, any variation comes from the read-out. This measurement gives an idea about the stability of each bridge.

3.2.2 Heaters

As commented before, the thermal diagnostics subsystem was equipped with heaters by means of which it was possible to apply thermal injections on critical points in order to maximise the different thermal effects seen in Section 3.1. Two types of heaters were attached to different locations, namely [46]:

- On the one hand, Kapton heaters with a nominal resistance of 45 Ω and maximum power of 2 W located on the lateral side of the OW Titanium flange (two for each OW) and on six struts (one for each strut) —see Figure 3.3 and Figure 3.4.

- On the other hand, NTC thermal sensors acting as heaters (2 kΩ resistors) with a maximum power of 45 mW, located on each $\pm\, x$ side of the EHs (two for each side, in total eight, although they were commanded by pairs). This type was used due to the stringent cleanliness requirements inside the EHs.

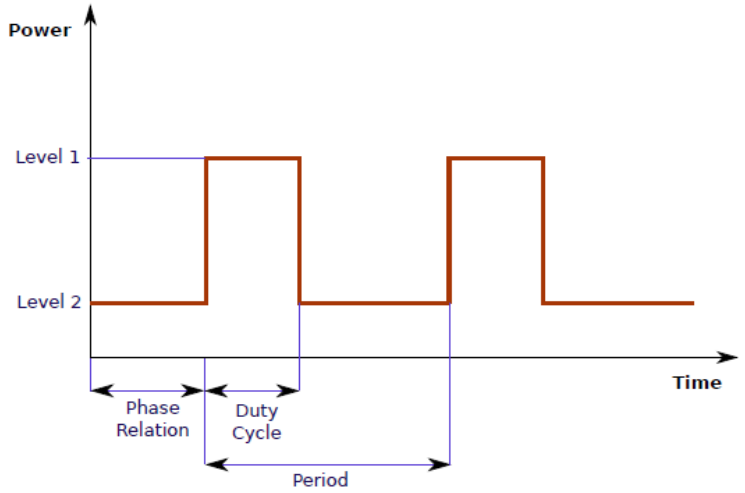

Figure 3.8: Parameters that were defined in the telecommand. Image obtained from [46].

Heaters were switched on/off using telecommands that were sent to the spacecraft where they were managed by the DMU [46, 83]. Four independent signals to four heaters could be commanded by one telecommand, two heaters for each DAU. Nevertheless, as a consequence of each DAU could only control one heater, a time multiplexing scheme was implemented (multiplexing between two outputs at 2 Hz), so that if two heaters were activated with the same DAU, the average power supplied per heater was half of the commanded power. Powers applied by the heaters were square signals whose following parameters could be defined in the telecommand: Level 1, Level 2, Phase Relation, Duty Cycle, and period, as seen in Figure 3.8.

Chapter 4

Thermal environment and temperature stability in LISA Pathfinder

In Chapter 3 we have seen which are the main physical mechanisms that introduce disturbances in the LPF measurement band due to thermal fluctuations. Furthermore, we have described the components of the thermal diagnostics subsystem by means of which not only the temperature in different locations was measured (with the thermal sensors), but also the thermally critical positions were stimulated by injecting temperature signals (with the heaters). In this chapter we describe the thermal environment during the LPF mission and the thermal stability achieved in flight [25], which is crucial to remove spurious effects arising from a large variety of thermal coupling phenomena. For this, there is an increasing demand for very controlled and stable environments in a wide range of experiments, both on ground and in space. Examples include geodesy missions [78], ongoing or proposed fundamental physics missions [11, 58] to on-ground experiments aiming at exoplanet detection [82].

Event	Date (DAL)
(a) Propulsion module released	22 Jan '16 (50)
(b) TMs released	15 Feb '16 (75)
(c) DMU SW crash	05 May '16 (154)
(d) Cluster-2 DCIU anomaly	09 Jul '16 (219)
(e) LTP safe mode	24 Sept '16 (296)
(f) DMU SW crash and reboot	21 Oct '16 (323)
(g) Thruster-4 anomaly	27 Oct '16 (329)
(h) TMs grabbed and TMs released	15 Jan '17 (409)
(i) Cooling down	23 Jan '17 (417)
(j) Cooling down	29 Apr '17 (513)
(k) Switch of SAU	02 Jul '17 (577)

Table 4.1: Dates associated with events that had an impact on the thermal balance onboard LPF. Table obtained from [25].

4.1 Thermal environment during the LISA Pathfinder mission

LPF took approximately a month –including LEOP (Launch and Early Orbit/Operations Phase) and apogee increase manoeuvres– to reach the L1 orbit and start the commissioning phase. LTP commissioning started on January 11th, 2016 and lasted until March 1st, 2016 when the mission started the operations phase. LPF underwent different phases during scientific operations which included nominal operations for the two experiments onboard, the LTP and the DRS, and an extended period of operations for both of them. Figure 4.1 shows the temperature as measured during all the mission by the diagnostics subsystem thermistors located on the LTP (top panel) and by the platform sensors attached to the external face of the thermal shield surrounding the LTP instrument (bottom panel). In this section we show the temperature measurements throughout the mission measured by the sensors explained in Section 3.2 at the different positions where they were located [25].

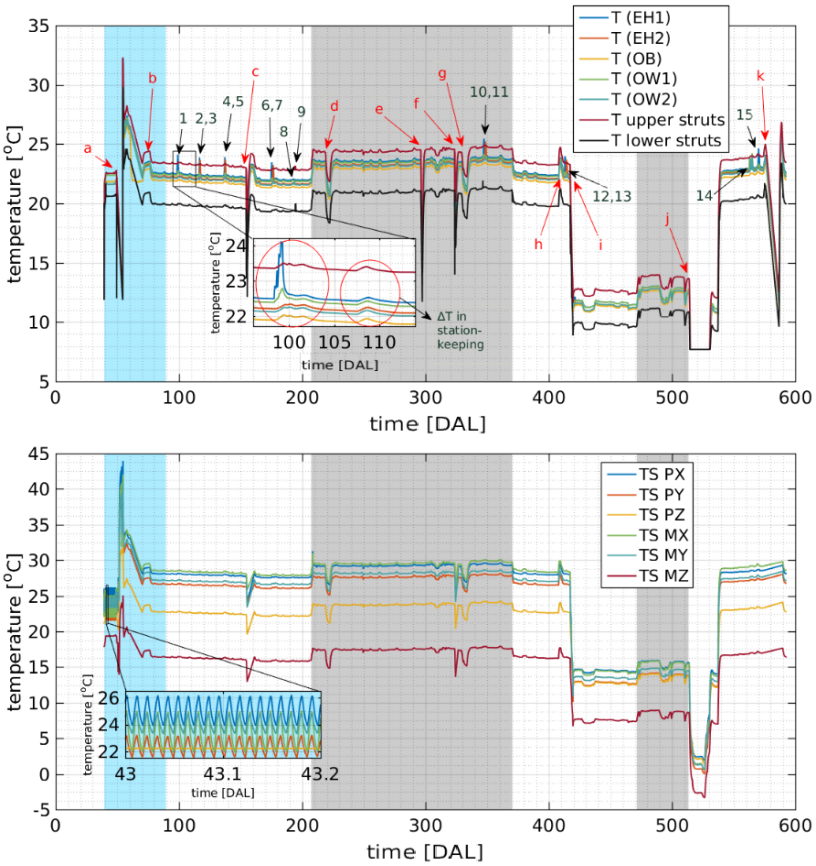

Figure 4.1: Temperature evolution during the whole LPF mission timeline. The initial cyan area (DAL 40-90) corresponds to the commissioning. The two grey shaded areas (DAL 210-370 and 470-510) correspond to the DRS operations, and the rest are LTP operations. The numbers and letters indicate events in which large temperature changes occurred —see Table 4.1 and Table 4.2. Images obtained from [25]. *Top:* Temperature as measured by the diagnostics subsystem located in sensitive locations of the LTP instrument, namely the OWs, the OB, the EHs, and the struts holding the LTP inside the thermal shield. The traces show the average temperature in locations with more than one sensor (4 in the EH, 3 in the OW, and 4 in the OB). *Bottom:* Temperature evolution during the whole mission timeline as measured by the platform sensors attached to the outer face of the thermal shield surrounding the LTP. Image obtained from [25].

4.1.1 Commissioning phase

The commissioning was a particularly active period in terms of temperature variations. It started during the first days of January 2016, after a cruise phase to L1. The first set of operations relevant from the temperature point of view was the *bang-bang* temperature control active during the first days of operations. As we can see in the inset of the Figure 4.1, lower panel, it produced $\sim 2\,^{o}$C peak-to-peak variations with a frequency around 1 mHz as measured by the platform sensors which was also measured, after the thermal shield attenuation, by the higher precision diagnostics sensors inside. As we will see in Section 4.2.2, this allows an experimental determination of the thermal shield thermal transfer function.

After this first phase and once in the desired orbit around L1, the propulsion module was ejected. This corresponds to the data gap in the commissioning phase —see the marked event in Figure 4.1— since the LTP instrument was switched off during this action. The sudden temperature increase afterward is a heating of the instrument intended to increase the outgassing rate and improve the cleanliness conditions before the release of the TMs and the start of free-fall operations. The release of the TMs took place on February 15th (TM2) and 16th (TM1), and it appears in the temperature read-out as a temperature increase due to associated satellite operations.

4.1.2 LISA Technology Package operations

The two periods of LTP operations took place from March 1st, 2016 to June 26th, 2016 within the nominal phase, and from December 8th, 2016 to March 17th, 2017 and May 1st, 2017 to June 30th, 2017 during the extended phase. A first characteristic to notice —see Figure 4.1— is a constant 3.5 ^{o}C gradient between the upper and lower struts during the whole mission, which only goes below the 3 ^{o}C during the cool down phase that will be explained below. A much lower temperature difference is also observed between the temperature sensors located in the rest of LTP locations. In

analysing these, it has to be taken into account that the temperature sensors of the LTP diagnostics subsystem were optimised for precision and not for accuracy, showing typically an absolute uncertainty of $\sim 0.2\,^{o}$C as mentioned in Section 3.2.1. Therefore, the differences in absolute temperature below this value must be considered within the error of the temperature read-out.

The temperature evolution during the LTP operations phase shows a series of sudden decreases of temperature together with some other, smaller, temperature increases. In Table 4.1 we gather the main features that caused the temperature decreases in the timeline. Most of these correspond to pauses in normal satellite operations, for example anomalies of the thruster subsystem during DRS operations or reboots of the DMU in the LTP operations phase. These events can trigger the satellite safe mode, which switches off some electronic units onboard, causing a consequent change in the satellite thermal balance.

The period of operations at lower temperature starting 430 DAL corresponds to an intended cooling down of the spacecraft with the objective of studying the instrument performance at a different temperature working point. The series of measurements that took place during these weeks could successfully determine a decrease in the instrument acceleration floor noise due to a suppression of the Brownian noise contribution due to gas particles hitting the TMs [21]. There were two cooling down phases —see the dates in Table 4.1. The first one decreased the temperature $\sim 10\,^{o}$C leaving the housing surrounding the TMs at $\sim 12\,^{o}$C. The second cooling down went below the design range of the temperature diagnostics subsystem and therefore appears as a saturated line in the temperature read-out in the upper panel of Figure 4.1. The lower panel in the same figure shows however the temperature in the thermal shield and how the coolest sensor in this structure reached $\sim -3\,^{o}$C. Given the complete time series and from the surrounding temperatures, we can estimate a temperature in the TM

position of $\sim 2\,^{o}$C for this period.

The LPF operations timeline was planned to get the maximum scientific yield from its capabilities as technology demonstrator. As such, an important fraction of the operations time was dedicated to experiments to gain insight in the different mechanisms that can perturb the state of free fall. Thermal fluctuations were a relevant part of the noise budget and, hence, several experiments were planned during the mission duration. Table 4.2 shows the list of executed experiments in the different locations where the instrument included heaters from the diagnostics subsystem, as it can be seen in Section 3.2.2. These experiments —with temperature increases $\sim 2\,^{o}$C and some of them lasting days— had an important impact in the temperature profile and for that reason were carefully planned in advance. The typical impact is shown in the inset of the top panel of Figure 4.1. The increase in temperature when injecting thermal signals in one EH is $\sim 2\,^{o}$C for the sensors located on the same EH and $\sim 0.1\,^{o}$C for the sensors on the other EH, $\sim 0.2\,^{o}$C for the sensors on the OB, $\sim 0.4\,^{o}$C for the sensors on the nearest OW and $\sim 0.15\,^{o}$C on the farther OW. In comparison, heaters located on the OWs and struts produced a temperature increase of $\sim 1\,^{o}$C, as measured by thermal sensors on these locations.

For the particular case shown in Figure 4.1, a series of thermal modulations were applied to one EH producing a modulating force in the TM that was used to derive the amount of coupling of the thermal-induced forces in the TM motion. The modulation pattern was repeated at different absolute temperatures —increasing the applied DC power— producing a stair-like profile. The total experiment duration was about a day and it took the LTP 2-3 days to recover from this disturbance.

The metastable orbit in L1 forced periodic station-keeping manoeuvres to keep the satellite in the predetermined orbit. Once the propulsion module was jettisoned —during the commissioning phase— the microNewton

subsystem was the only available thrusting system in LPF. The low thrust available required prolonged operations of the thrusters, initially set to one 12 h period each week. In thermal terms, the result of this operation is shown again in the inset of the top panel of Figure 4.1, i.e. the operation of the thruster subsystem in wide range mode (with less precision but higher thrust) for station keeping turned into a $\sim 0.1\,^{\circ}$C homogeneous increase in the different locations of the satellite. Although not representing an operational inconvenience, this mode of operations resulted in a reduction of the mission effective duty cycle since the scientific runs required a extremely quiet environment. Hence, the scientific runs duration were limited by the long time-scales needed for the thermal environment to recover the steady state after station keeping. Later in the mission, this limitation was overcome by allowing longer, less frequent station keepings. That way, week-long scientific runs were executed which allowed the estimation of the instrument acceleration noise down to the 20 μHz regime [21]. We can also see a thermal gradient between the temperatures measured by the sensors located on the LCA, being the maximum gradient of $\sim 13\,^{\circ}$C, as shown Figure 4.1 (bottom). During the first cooling down, the lower temperature given by the sensor TS MZ reaches a temperature of $\sim 7\,^{\circ}$C, while during the second cooling down it reaches a negative value, $\sim -3\,^{\circ}$C, the only temperature registered below zero.

4.1.3 Disturbance Reduction System operations

DRS operations took place from June 27th, 2016 to December 7th, 2016 in its nominal phase, and from March 18th, 2017 to April 30th, 2017 in its extended phase. The hand over of the spacecraft control to the DRS team required a series of configuration changes that had an impact on the thermal environment. As thoroughly described in [14], the hand over to the DRS team implied that, while the LTP instrument was still providing measurements of spacecraft and TMs attitude, this information was sent to the Integrated Avionics Unit (IAU), which determined the forces and torques to be applied to the TMs and to the satellite. The first were delivered again

Event	Date (DAL)
(1) Thermal injections in EH1	10 Mar '16 (98)
(2) Thermal injections in EH1	28 Mar '16 (116)
(3) Thermal injections in EH2	28 Mar '16 (116)
(4) Thermal injections in EH1	17 Apr '16 (136)
(5) Thermal injections in EH2	18 Apr '16 (137)
(6) Thermal injections in EH1	25 May '16 (174)
(7) Thermal injections in EH2	27 May '16 (176)
(8) Thermal injections in OWs	13 Jun '16 (193)
(9) Thermal injections in STRs	13 Jun '16 (193)
(10) Thermal injections in EH1	14 Nov '16 (347)
(11) Thermal injections in EH2	15 Nov '16 (348)
(12) Thermal injections in EH1	18 Jan '17 (412)
(13) Thermal injections in EH2	19 Jan '17 (413)
(14) Thermal injections in OWs	17 Jun '17 (562)
(15) Thermal injections in EH1	24 Jun '17 (569)

Table 4.2: Dates associated with thermal experiments onboard LISA Pathfinder. Table obtained from [25].

to the LTP while the second were sent to the colloidal thrusters. Both IAU and the colloidal thrusters were inactive during LTP operations.

As seen in Figure 4.1, the continuous operations of these two units (gray shaded areas) changed the thermal balance in the satellite, raising the overall temperature by $\sim 2^{\circ}$C with respect to the LTP operations. The DRS operations phase shows some pronounced decays in temperature corresponding to short interruptions of operations due to detected anomalies in the thruster subsystem. More details about this phase have been published in [14].

4.2 Thermal stability in LISA Pathfinder

Achieving the scientific goal in LPF was a complex endeavour that required excellent design and performance of several sensors and actuators. In Section 3.1 we have seen that temperature stability is a crucial one among them since it impacted in several ways the measurement chain. The aim of this section is to quantitatively assess the temperature stability of the instrument which goes in parallel with the determination of the performance of the temperature diagnostics subsystem [25].

In Figure 4.2 we can see the typical stability measured in LPF during a scientific run, in this case the one in February 2017. We use a sensor in the OB to show the typical evolution of the temperature during a quiet interval. A histogram with the temperature derivative for a sensor in the OB during the whole mission duration is included in the middle panel of Figure 4.2. The histogram shows that, overall, the instrument spent nearly 250 days with temperature drifts in the range $\pm 1\,\mu\,^{\circ}\mathrm{C\,s^{-1}}$. Additionally, it is included in the bottom panel of Figure 4.2 a histogram with the temperature derivative for the same sensor during three noise runs. Temperature drifts are not only an important figure for the platform stability but, as it is commented below, they have an important role in the evaluation of the performance of the sensors.

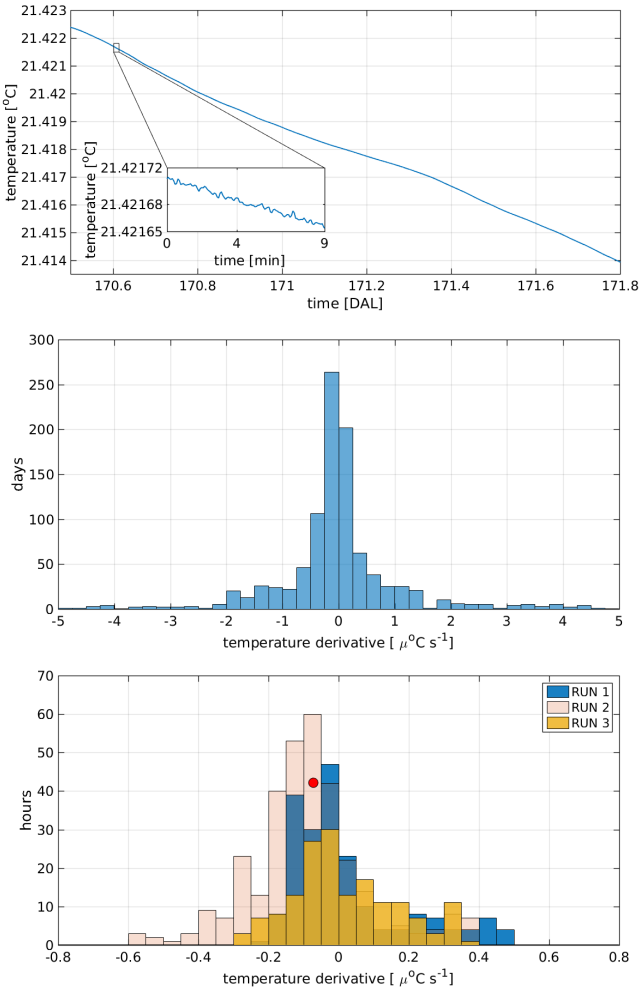

Figure 4.2: *Top*: Typical temperature evolution of a sensor located in the OB during a quiet noise run. Image obtained from [25]. *Middle*: Histogram showing the number of days with a given temperature drift for a sensor in the OB (TS13) for the whole mission duration. *Bottom*: Histogram showing the number of days with a given temperature drift for a sensor in the OB (TS13) for three different noise runs, with RUN 1 from November 17th to November 26th (2016), RUN 2 from February 14th to February 27th (2017) and RUN 3 from May 29th to June 5th (2017). The dot indicates the temperature derivative that corresponds to the time series at the top of the plot. Image obtained from [25].

4.2.1 Temperature fluctuations amplitude spectral density

In order to evaluate the temperature stability in the instrument we start evaluating the stability of the environment surrounding the instrument. The LTP was encapsulated in a thermal shield to suppress thermal fluctuations arising in the electronics surrounding the experiment. A series of sensors —not belonging to the diagnostics subsystem— monitored the thermal fluctuations in several locations around the satellite. These sensors were not designed for precise measurements of thermal stability, and therefore their floor noise, $50\,\mathrm{mK}/\sqrt{\mathrm{Hz}}$, is orders of magnitude above the ones belonging to the diagnostics subsystem. Despite its reduced precision, the temperature fluctuations of the spacecraft were high enough at low frequencies to measure them.

To evaluate thermal fluctuations, the ASD —the square root of the power spectral density— has been computed by means of the Welch averaged periodogram [95]. We have used segments of 400000 s and applied the Blackman-Harris window to prevent spectral leakage. To make sure that the window is not biasing our estimate, we get rid of the lowest four frequency bins of the spectra. With the remaining spectra we evaluate the power at low frequencies by means of a power-law fit at the four lowest frequency bins. In the locations where we have more than one sensor we use an average over the sensors when considering the power-law fit. For the struts, where each sensor is attached to a different strut, we use the TS17 sensor as a typical case to evaluate the low-frequency power. The coefficients of the fit obtained in each individual location are shown in Appendix A.

In Figure 4.3 we show the results for a long stable run on February 2017. In the top panel we can distinguish a thermally induced $f^{-1.34\pm0.05}$ power law below 100μHz in all the six sensors attached to the thermal shield. These low-frequency fluctuations are transmitted to the instrument through the thermal shield and the struts. As the spacecraft induced temperature

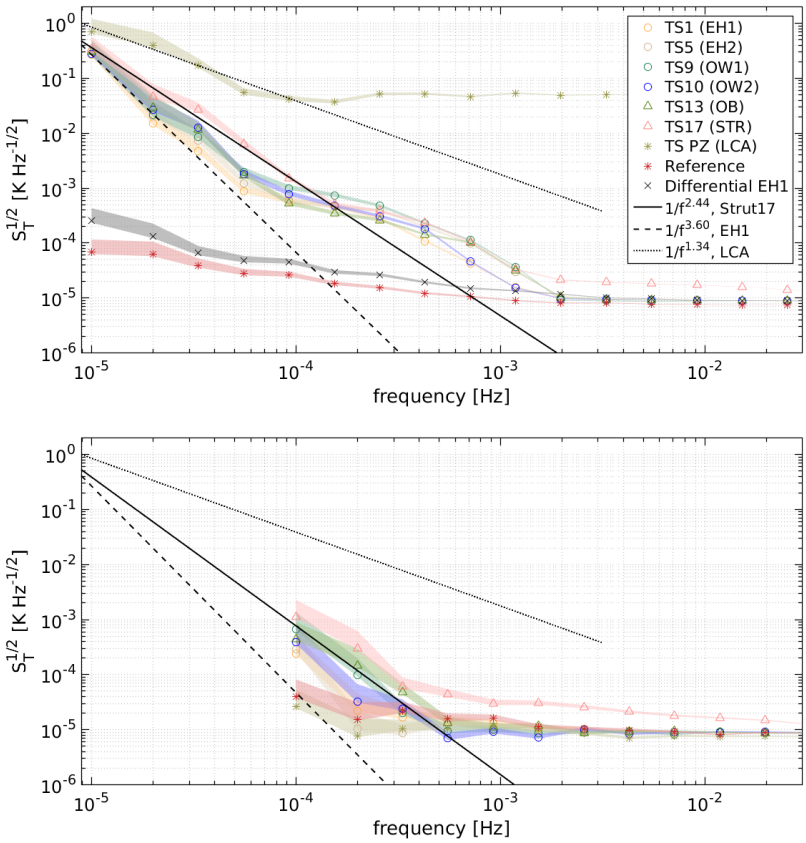

Figure 4.3: Temperature stability measured as ASD in different locations at the LTP during the period February 14th-27th, 2017. Images obtained from [25]. *Top*: Different locations inside the LTP as measured by the temperature diagnostics subsystem. When different sensors were available, the mean value of the measurements is used to obtain the fit at low frequencies. In addition, it shows the temperature given by one spacecraft temperature sensor in the outer face of the instrument thermal shield, also showing the fit for low frequencies taking into account the mean value of the measurements given by all the sensors located on the shield. Differential and reference measurements are also shown. *Bottom*: The same as before but evaluated using a shorter segment (February 19th-20th, 2017) with lower temperature drift.

fluctuations leak into the instrument they are successively suppressed, since each stage acts as a thermal low-pass filter. This can be appreciated when comparing the different slopes of the power-law fits in Figure 4.3. We notice how low-frequency power has decreased from the original $f^{-1.34\pm0.05}$ on the outer layer of the thermal shield to $f^{-2.44\pm0.06}$ in the struts and even further to $f^{-3.60\pm0.04}$ if we continue to the EH sensors. The cause of the decrease in power at lower frequencies is, as previously said, the different layers of materials that the heat flow needs to cross, which act as a series of consecutive thermal low-pass filters.

So far the analysis focused on the February 2017 science run. However, in order to evaluate the non-stationarities in temperature fluctuations it is possible to compare these results to other science runs where the instrument was kept unperturbed in its most sensitive configuration for several days. Since we are purely interested in the temperature contribution, for each of these we compute the ASD in the $10-30\,\mu$Hz band. The results are shown in Figure 4.4. The amplitude of temperature fluctuations in the lowest bins of the LISA frequency band is maintained in the $50-100\,\mathrm{mK}/\sqrt{\mathrm{Hz}}$ range for most of the runs in the OB, OW, and EH locations. As expected, the ASD can increase up to $180\,\mathrm{mK}/\sqrt{\mathrm{Hz}}$ in some runs for the temperature in the struts as shown in the bottom panel of Figure 4.4. The analysis shows therefore a considerable level of stationarity in the amplitude of thermal fluctuations in the $10-30\,\mu$Hz band for the whole duration of the mission. The same conclusion could be drawn by comparing the power-law fits for each of the runs we have analysed. In Appendix A it is provided a table with the fits to power laws for each of these runs together with its dates of occurrence.

Thermal fluctuations in these locations are hence described by the power-law fits shown in the Figure 4.3. The rest of features appearing in the plot do not describe thermal fluctuations but are instead related to the temperature read-out. At higher frequencies the LPF temperature front-end is

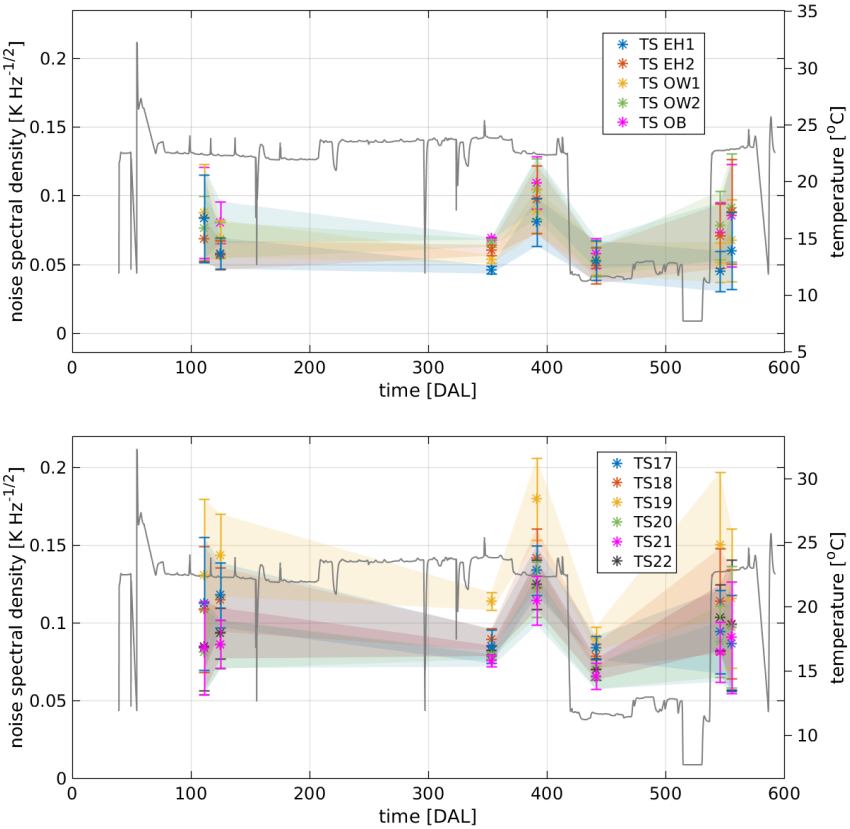

Figure 4.4: Time evolution for the amplitude spectra of temperature fluctuations in the $10 - 30\,\mu$Hz frequency range. Only noise runs with several days of stable conditions. In grey we can see the temperature profile of the mission for comparison. Images obtained from [25]. *Top:* OB, OW, and EH sensors. *Bottom:* Temperature sensors at the struts.

limited by read-out noise, which is fundamentally dominated by the WB noise. The in-flight measurements reached the design limit of $10\,\mu\mathrm{K}/\sqrt{\mathrm{Hz}}$, a level that was also achieved during on-ground testing [59, 74]. This noise floor goes down to nearly 1 mHz which was the LPF measuring bandwidth.

The frequency regime from 0.2 mHz to 2 mHz is dominated by read-out

noise arising from non-linearities in the temperature diagnostics, ADC [76]. Although being studied and characterised during the design phase, this read-out noise source was not considered critical for the mission success since it was limited to frequencies below the LPF band. This contribution can be modelled and subtracted to some extent [72]. Nevertheless, the design of the future LISA thermal diagnostics subsystem will need to overcome this noise source that otherwise would affect the discrimination of temperature induced disturbances in the sub-milliHertz band. Since the ADC-induced noise increases with wider excursion in the ADC range, a segment that explores less range will show a reduced impact of such a noise. The bottom plot in Figure 4.3 confirms this by evaluating the ASD of thermal fluctuations in a shorter segment with less temperature drift.

Apart from the absolute temperature measurements, the temperature diagnostics front-end included some other channels to help disentangle noise sources in the actual temperature read-out —see Section 3.2.1. By one side, the so-called *reference* measurements were used to unambiguously determine the floor noise of the read-out. These measurements were obtained by means of high stability resistors mounted on the same WB used for the temperature sensing, allowing a direct measurement of the bridge electronics noise. On the other side, for some designated couple of sensors the electronics implemented a direct differential measurement by comparing directly them in the WB, that is a direct hardware differential measurement. These were called *differential* measurements —see Section 3.2.1. Both are shown in Figure 4.3. The differential measurements are, in particular, a second cross-check to confirm the non-thermal origin of the excess noise observed in the mid-band. Indeed, due to its nature the differential measurements are closer to zero and, hence, use less range of the ADC. As a consequence they are less exposed to ADC non-linearities induced noise, as it is shown in the plots.

4.2.2 Thermal transfer functions

In the previous section the behaviour of thermal fluctuations has been evaluated, having quantified the noise spectra at different locations and its temporal evolution. Now, we are going to explore the correlation between thermal fluctuations at different locations. This is an important exercise to understand the thermal link between the different subsystems onboard, a key aspect for instruments like LPF and LISA. We saw that the temperature diagnostics subsystem onboard included heaters in thermally sensitive locations such as the EHs, the OWs, and the struts. The aim of injecting temperature pulses at these locations was to study the instrument response to thermal disturbances in terms of forces exerted on the TMs or displacements measured by the optical read-out. The results of these experiments are of interest for the design of the future LISA mission. However, as a side product, we can experimentally derive thermal transfer functions between different locations, as shown below [25].

To do so, different heat pulses that were injected in the different locations during the mission timeline have been used. We have taken into account some injections shown in Table 4.2 as well as the injections carried out by platform heaters during the *bang-bang* control phase during the commissioning —with temperature variations $\sim 2\,^{\circ}$C. While the former will characterise point-to-point correlations between locations inside the experiment, the latter will tell us about the response of the diagnostics subsystem sensors to external perturbations.

For each of these phases where an active thermal stimulus was present in the satellite, the transfer functions have been derived comparing the Discrete Fourier Transform (DFT) of the temperature time series at two different locations. The result of this operation is a complex value (expressed as magnitude and phase) shown by the dots in Figure 4.5. The lines in the same plot correspond to the best fit models in the frequency domain.

In Appendix B it is presented the estimation and modelling of the transfer functions and provided the parameters describing the models obtained during the analysis. It is important to keep in mind when interpreting these results that thermal injections were not intended for the purpose of our current study and, therefore, neither the amplitude nor the frequency of the applied signal are the optimal ones.

Figure 4.5 summarises these results. We can see in the different panels the thermal transfer functions for each different location where the thermal injection was applied. The top panel describes the effect of the thermal shield surrounding the main instrument onboard. We notice that the attenuation of thermal fluctuations from the external environment to the LPF instrument is better than 10^{-2} for fluctuations with frequencies above 1 mHz. Thermal fluctuations are then further attenuated on their way to the inner part of the instrument when crossing the struts holding the instrument inside the thermal shield. Indeed, the second panel shows the temperature suppression factor from the different struts to the rest of the locations in the inner core of the instrument. Any temperature fluctuation moving through this path in milliHertz equivalent time-scales is attenuated by a factor of $5 \cdot 10^{-5}$. In this case, the CFRP (Carbon Fiber Reinforced Polymer) struts and the massive OB Zerodur structure are acting as equivalent thermal low-pass filters.

The last two panels describe the impact of thermal experiments —as measured by surrounding sensors— in the inner core of the instrument, i.e. the OWs and the EHs, respectively. A first point to take into account in understanding these figures is that, while the experiments in the OWs reached temperature increases of $\sim 2\,^{\circ}\mathrm{C}$, the temperature modulations in the EHs —being these a much more thermal sensitive locations— were instead in the milliKelvin range. Consequently, the temperature increases due to the EH experiments in the surrounding sensors are not so clearly measured and, therefore, these transfer functions are measured with lower precision. Even

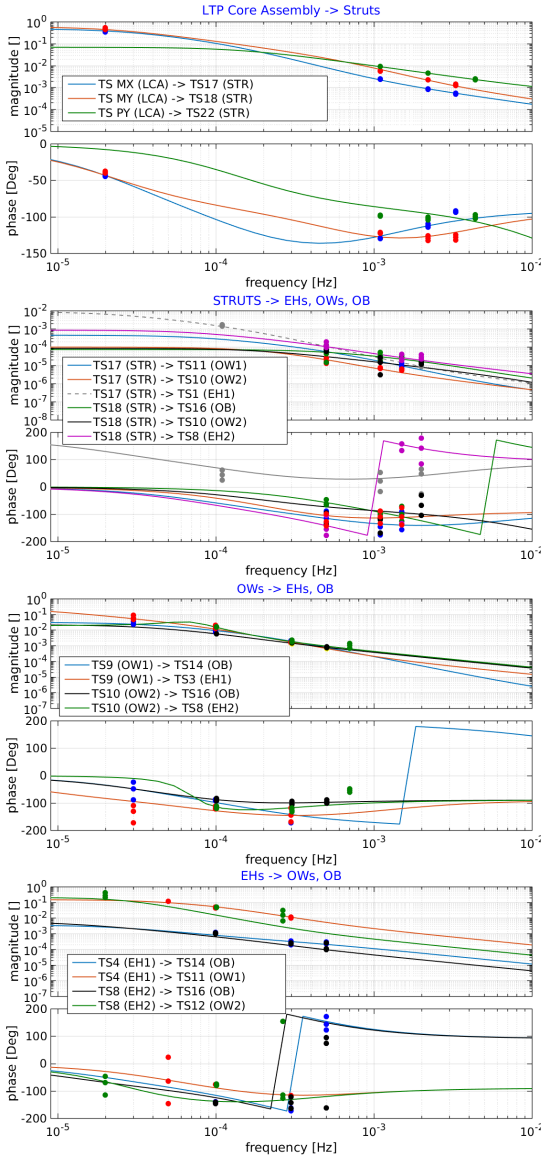

Figure 4.5: Transfer functions between sensors in different locations. The points show these transfer functions at a certain frequency while the lines represent the fit to these functions. Images obtained from [25].

though, thanks to the high precision of the temperature sensors we are able to estimate a 10^{-4} attenuation in the LPF measuring band for temperature fluctuations being transferred from the EH to the OB. The time-scales characterising the thermal path for these fluctuations is ~ 2 days which makes it easier to distinguish from other decorrelated thermal fluctuations.

Although not shown in the figures, we can get an estimate of the thermal transfer function at even lower frequencies. When taking into account the complete temperature series we observe a year modulation of the spacecraft solar array temperature of $\sim 3.5\,^{o}$C, which is proportional to the variation of the spacecraft solid angle with respect to the Sun throughout this period. The same modulation can be traced to the EH with an amplitude of $\sim 0.35^{o}$C, from where it is possible to derive a factor 10 attenuation to external thermal fluctuations in the frequency $3 \cdot 10^{-8}$ Hz, a year period.

4.3 Implications for LISA

Looking towards LISA, the most evident lesson learned from the LPF operations refers to the station-keeping manoeuvres. These were mandatory to keep the satellite in the Lissajous orbit around L1. However, the low thrust available in the propulsion system forced a several hours manoeuvre that produced an overall ~ 100 mK temperature increase. Originally, this operation was repeated each weekend which, after the long thermal transient, left a few days for science runs in stable conditions. This periodic station keeping is ruled out for LISA given that it would seriously impact its performance in the low-frequency regime. Each LISA spacecraft will be injected in its individual orbit avoiding the need of periodic corrections. Other thermal perturbations, like the thermal experiments that were repeated frequently in a technology demonstrator as LPF will be kept to the commissioning phase for LISA.

In terms of performance, the diagnostics subsystem achieved the re-

quired performance of $10\mu K/\sqrt{Hz}$ in the mission band, 1mHz < f < 30mHz, showing only a slight deviation in the lowest frequency bin. The latter is due to a coupling of the temperature drift onboard with non-linearities in the ADC. The effect was already known to affect the sub-milliHertz band during the design phase but the extensive operations period in a extremely quiet environment has allowed a precise characterisation. This will allow an improved design overcoming this read-out noise contribution for the future LISA temperature diagnostics subsystem.

The low-frequency band below the 100 μHz is dominated by temperature fluctuations that, in this band, exceed the noise contribution from the ADC non-linearities. Thanks to the extensive data set we have been able to determine a noise level of $50 - 100\ mK/\sqrt{Hz}$ in the lowest bins of the LISA frequency band, $10 - 30\ \mu$Hz, for those locations in the inner core of the experiment [25]. This noise level was maintained during the different science runs throughout the mission, which provides an important insight of the stationarity of the thermal fluctuations in the very low frequency domain during flight operations.

It has been also determined a $f^{-3.60\pm0.04}$ power law for the temperature fluctuations in the EH dominating the lowest frequency bins, below the 100 μHz [25]. The cause of these fluctuations must be sought in the electronic units surrounding the main instrument in the satellite. We have also determined fluctuations outside the thermal shield to be characterised by a $f^{-1.34\pm0.05}$ power law [25]. The characterisation of these low-frequency temperature fluctuations is relevant for LISA since this corresponds to the lowest frequency bins of the mission, where temperature variations are expected to provide a significant limit to the instrument's performance.

These figures are however not directly applicable to LISA, being the mission still in its definition phase, but they are an important asset since they can serve as an anchoring point for the thermal design. In the same line

of paving the way for the thermal design of the future LISA mission, we took advantage of the different thermal experiments in the mission timeline to determine the thermal transfer function between locations, thereby deriving the attenuation factors due to the different shielding layers that can be used as guidance for the future LISA design.

Chapter 5

Path-length variations due to thermo-optical and thermo-elastic effects

In Chapter 3 we describe the thermal effects that produced disturbances in the differential acceleration between the TMs in the LPF frequency band. There were two ways of perturbing the main measurement:

- By means of direct forces on the TMs, forces that were produced, among others, by radiation pressure or outgassing effect —see Section 3.1.1.

- By means of coupling with the optical path length of the interferometric signal. This did not produce real forces on the TMs but modified the interferometric distance between them, which was seen as a force by the satellite —see Section 3.1.2. Critical components responsible of introducing these perturbations as a consequence of thermal fluctuations were the two OWs and the struts. Temperatures changes on the former caused thermo-optical effects while temperatures changes on the latter caused thermo-elastic effects.

In this chapter we study the experiments carried out in flight during the LPF mission in order to estimate what part of the differential acceleration comes from thermo-optical and themo-elastic effects, that is, from path-length variations which do not imply real forces on the TMs. To that end, thermal signals were injected with the heaters located on the OWs and the struts, enhancing these effects and their contribution on the differential acceleration.

5.1 Differential acceleration

As stated in Section 2.3.1, the main scientific magnitude considered was Δg, the differential acceleration between both TMs. The standard Δg equation in Eq. (2.8) takes into account dynamical terms. However, if we want to study the thermal contributions that produce path-length variations but not real forces on the TMs, new terms have to be introduced into the Δg expression. These terms will account for the contribution of the effects we have previously described in Section 3.1.2, and, therefore, will be the ones used in our analysis. In addition, we can consider two new stiffness terms that can be specially important when changes in the temperature appear, which are related with the relative positions between the GRSs and the OB. These relative positions can vary as a consequence of a thermo-mechanical expansion. Taking into account all the above, we have —see Appendix C for a detailed derivation [35]:

$$\Delta g_0 = \Delta g_{\rm te} + \ddot{o}_{\rm OW1} + \ddot{o}_{\rm OW2} + \ddot{o}_{\rm STR} + \ddot{o}_{\rm OB}$$

$$-\omega_2^2 \cdot (x_{\rm GRS2} - x_{\rm GRS1} - o_{12}) - \Delta\omega_{12}^2 \cdot (x_{\rm GRS1} - o_1). \qquad (5.1)$$

where Δg_0 is the standard definition of Δg —see Section 2.3.1. The quantities $\ddot{o}_{\rm OW1}$, $\ddot{o}_{\rm OW2}$, $\ddot{o}_{\rm STR}$, and $\ddot{o}_{\rm OB}$ describe the thermo-elastic and thermo-optical contributions that come from the OWs, the struts, and the OB, respectively, so we have to consider any of them as long as there are thermal fluctuations on these components. The contribution from the struts,

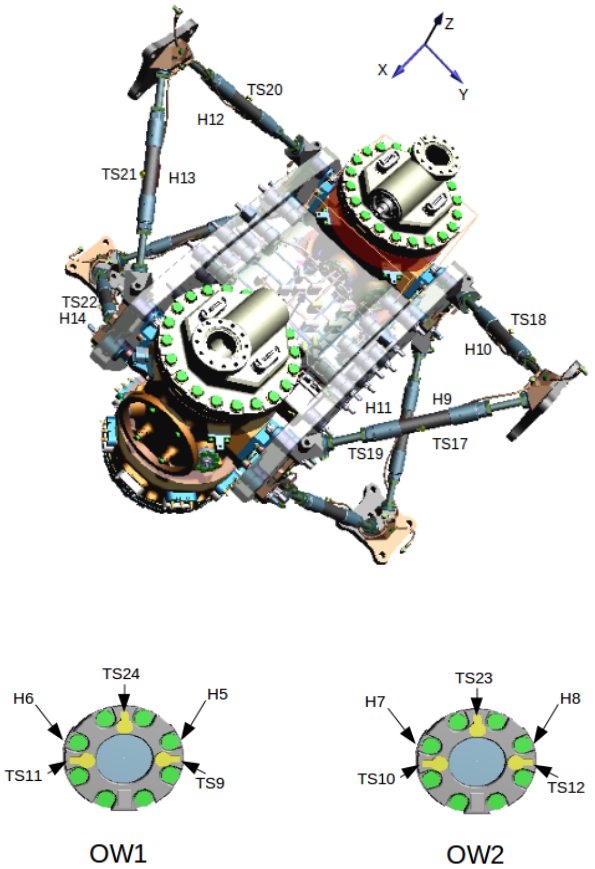

Figure 5.1: Schematic of the temperature sensors and heaters on the struts and on the OWs. The positions of these heaters and sensors can also be seen in Section 3.2, together with the rest of the heaters and sensors.

$\ddot{o}_{\mathrm{STR}}$, is directly correlated to the OB contribution, $\ddot{o}_{\mathrm{OB}}$. The reason being that thermal fluctuations on the struts perturbed the OB that in turn introduced deviations in the path length. However, we introduce two different terms to distinguish the perturbations on the OB from the ones coming from the struts (during the mission we carried out experiments using the heaters on the struts, there were no heaters on the OB). In addition, the equation includes terms coming from displacements between the GRSs and the OB, $\omega_2^2 \cdot (x_{\mathrm{GRS2}} - x_{\mathrm{GRS1}} - o_{12})$ and $\Delta\omega_{12}^2 \cdot (x_{\mathrm{GRS1}} - o_1)$ —see Appendix C—, although the second one is negligible because $\Delta\omega_{12}^2 \ll \omega_2^2$.

Thus Δg_0 includes the path-length variation introduced by $\ddot{o}_{\mathrm{OW1}}$, $\ddot{o}_{\mathrm{OW2}}$, $\ddot{o}_{\mathrm{STR}}$, and $\ddot{o}_{\mathrm{OB}}$, and the thermo-mechanical distortion between the GRSs and the OB expressed through the terms $\omega_2^2 \cdot (x_{\mathrm{GRS2}} - x_{\mathrm{GRS1}} - o_{12})$ and $\Delta\omega_{12}^2 \cdot (x_{\mathrm{GRS1}} - o_1)$. Hence, Δg_{te} is the Δg free of these effects. For the case of the experiments that are seen in this chapter, we use $\omega_2^2 = (-4.90 \pm 0.05) \cdot 10^{-7}\ \mathrm{s}^{-2}$ (the stiffness term as estimated by dedicated experiments [23]).

5.2 In-flight experiments

Several series of injections were carried out by means of the heaters on the OWs and struts to characterise the thermo-optical and thermo-elastic effects as well as estimate their contributions to the total differential acceleration noise.

5.2.1 Optical Window thermal experiment

As stated in Section 3.1.2, thermal fluctuations on the OWs could produce path-length variations as a consequence of two physical mechanisms, namely change in the refractive index of the glass and stress between the glass and the Titanium flange. In order to quantify and describe these phenomena which caused thermo-optical effects, the following signals were injected on the OWs (experiments carried out between June 17th and June 20th, 2017) —see Table 4.2 and Table 5.1:

Heater	Powers (mW)	Number of pulses	Pulse frequency (mHz)	Duty Cycle (%)
H5 and H6	50 × 2	5	0.1	50
H6 and H7	50 × 2	5	0.1	50
H5	20, 50 and 100	5	1	50
H7	20, 50 and 100	5	1	50
H6	20, 50 and 100	5	1	50
H8	20, 50 and 100	5	1	50
H5 and H6	20 × 2, 50 × 2 and 100 × 2	5	1	50
H7 and H8	20 × 2, 50 × 2 and 100 × 2	5	1	50
H5	160, 130, 100, 70 and 50	20	20	50
H7	160, 130, 100, 70 and 50	20	20	50
H6	160, 130, 100, 70 and 50	20	20	50
H8	160, 130, 100, 70 and 50	20	20	50
H5 and H6	160 × 2, 130 × 2, 100 × 2, 70 × 2 and 50 × 2	20	20	50
H7 and H8	160 × 2, 130 × 2, 100 × 2, 70 × 2 and 50 × 2	20	20	50

Table 5.1: Parameters of the square signals injected by the heaters during the OW experiment (experiments carried out between June 17th and June 20th, 2017).

- Both heaters were switched on simultaneously for the OW1 injecting five 5000 s square waves at approximately 50 mW (10000 s period or 0.1 mHz frequency with 50% Duty Cycle) —see Section 3.2.2. When this first sequence finished, the same injection was made for the OW2. These low-frequency injections aimed to stimulate the thermo-optical effect that appears due to the change in the refractive index of the glass —see Section 3.1.2. However, we will see in the following sections that when the OWs were heated for so long, this produced real forces on the TMs, not only path-length variations of the laser beam —see Figure 5.4.

- An individual heater for the OW1 was activated, and after this, an individual heater for the OW2. Next, the same sequence with the other heater for each OW. Finally, both heaters for the OW1, and, after, both heaters for the OW2. Five 500 s square waves (1000 s period or 1 mHz frequency with 50% Duty Cycle) were injected with each heater at each activation. This complete sequence was made by injecting signals at three different powers (20, 50 and 100 mW). These injections were intended to maximise both the thermo-optical effect that appears due to the change in the refractive index of the glass and the thermo-optical effect that appears due to the stress between the Titanium flange and the glass —see Section 3.1.2. With the different powers applied, it was sought to see if there was any relationship between these effects and the power of the signals.

- Similar to the injections at 1 mHz but at five different powers (160, 130, 100, 70 and 50 mW), and injecting twenty 25 s square waves (50 s period or 20 mHz frequency with 50% Duty Cycle) with each heater at each activation. These signals were mainly injected to analyse the causes of the very fast peaks that appear when the heaters were switched on and off —see Figure 5.4. Several powers were injected to see if the peaks depended on them or not.

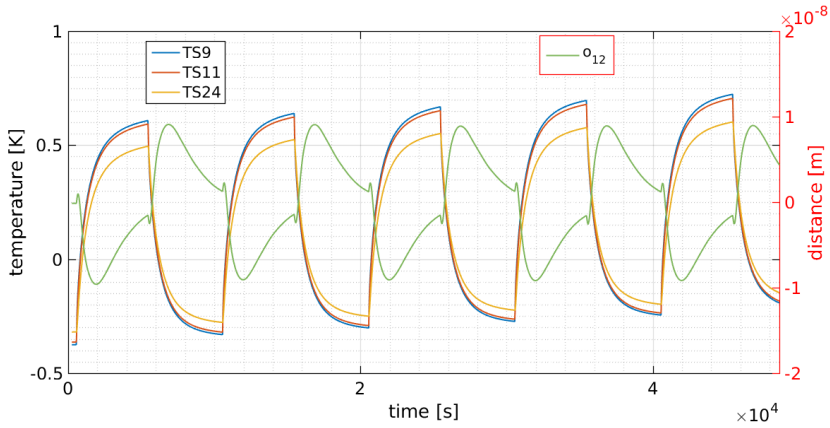

Figure 5.2: Thermal response of the OW1 thermal sensors for the injections at 0.1 mHz and interferometric differential distance between both TMs produced by these temperature fluctuations.

Figure 5.2 shows the thermal fluctuations and the changes in the interferometric differential distance for the injections at 0.1 mHz.

5.2.2 Strut thermal experiment

In Section 3.1.2 we saw that thermal fluctuations on the struts could produce structural distortions because these were the link between the LTP and the thermal shield. For this reason, several stimuli were injected using the heaters attached to them between June 13th and June 14th, 2016 — see Table 4.2. The experiment consisted of three 100 s square waves at approximately 250 mW (2000 s period or 0.5 mHz frequency with 10% Duty Cycle) for each heater, that produced the temperature fluctuations and the changes in the interferometric differential distance plotted in Figure 5.3.

5.3 Optical Window thermal experiment results

The aim of the set of runs explained in the previous section was to produce changes in Δg_0 coming from thermo-optical effects, estimating the contribution of $\ddot{o}_{\mathrm{OW1}}$ and $\ddot{o}_{\mathrm{OW2}}$ in Eq. (5.1). However, while the OWs were

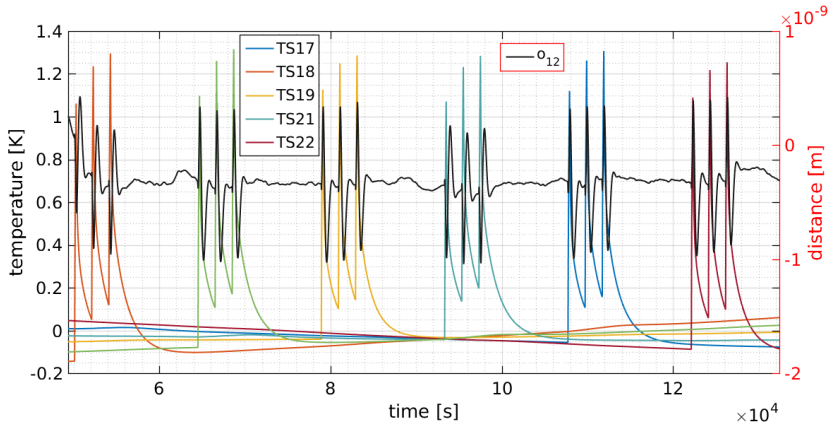

Figure 5.3: Thermal response of the different struts thermal sensors and interferometric differential distance between both TMs produced by these temperature fluctuations.

heated, there were other effects in other time-scales that acted on the system. Looking at Figure 5.4, we observe that Δg_0 seems to show three effects with different time-scales, namely:

- At the beginning and at the end of each pulse we observe that a glitch is produced (the glitch at the switch on has the opposite sign as compared to the glitch produced at the switch off). The effect that causes these peaks seems to be non-thermal because the time-scale is very short (few seconds). The most plausible origin of these features is a magnetic field induced when the heaters were switched on and off, which in turn induced an eddy current in the TM that caused a force on it [55].

- After the glitches we observe a modulation (time-scale of 50 s) that we consider to be due to thermo-optical effects on the OW: stress between the Titanium flange and the glass, and thermal changes of the refractive index [65] —see Section 3.1.2. In Section 3.1.2 we have seen that these thermo-optical effects produced a path-length variation but not real forces on the TMs.

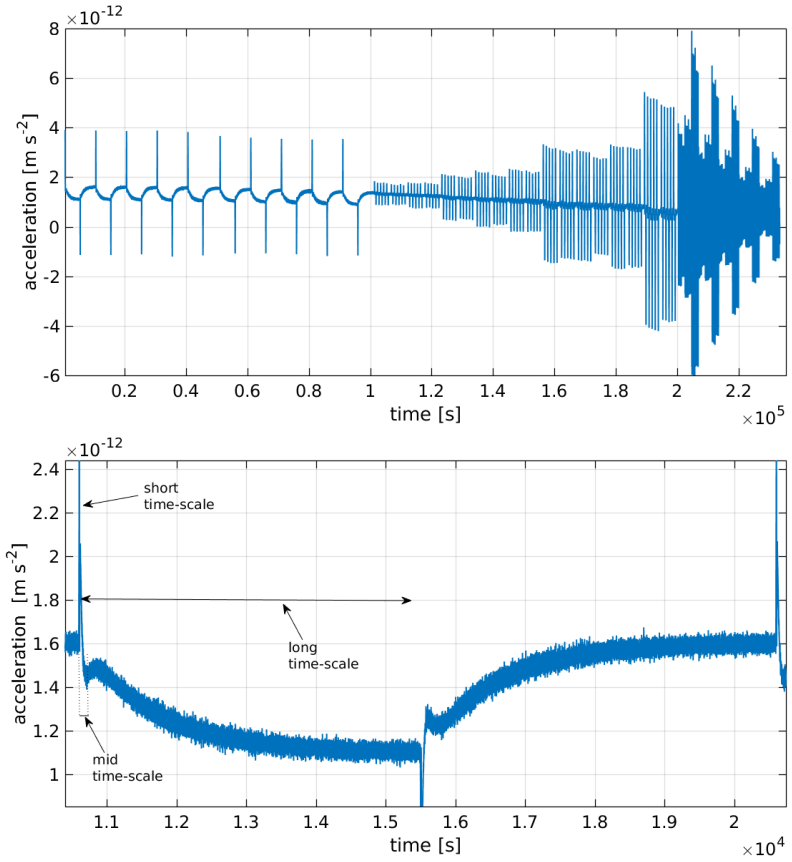

Figure 5.4: *Top*: Complete Δg_0 for the OW injections. We have applied a low-pass filter of order 1 at 0.1 Hz as cut-off frequency. *Bottom*: Three differents time-scales in Δg_0 for the injections at 0.1 mHz. In the figure it is possible to distinguish a first very short time-scale (few seconds), which corresponds to the peak, followed by a longer time-scale (50 s) for the small modulation after the glitch, and finally, a long time-scale (5000 s).

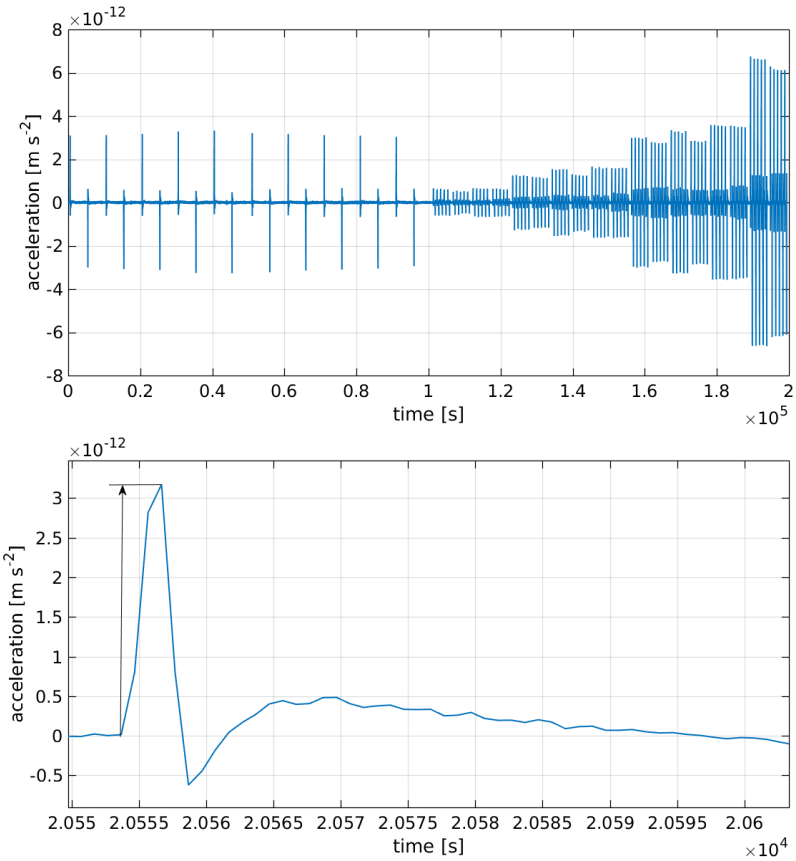

Figure 5.5: *Top*: $\frac{d^2 o_{12}}{dt^2}$ for the injections at 0.1 mHz and 1 mHz. *Bottom*: Amplitude selected for $\frac{d^2 o_{12}}{dt^2}$.

- On a large time-scale (5000 s) we appreciate a behaviour that seems to be related to the OW average temperature. This shape could be due to some effect inside the GRSs like outgassing or radiation pressure, effects that produce real forces on the TMs — see Section 3.1.1.

5.3.1 Short-term effect: Glitches

This effect corresponds to the glitches appearing when we switched on and off the heaters, as shown in Figure 5.4. These glitches appeared with posi-

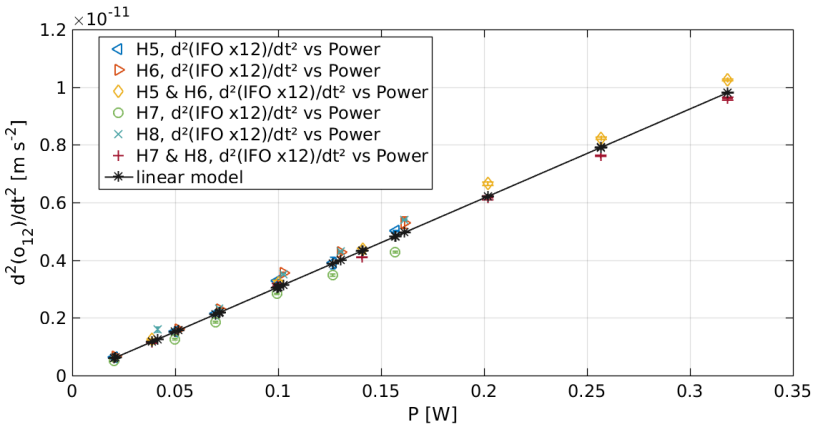

Figure 5.6: Linear fit between Power and $\frac{d^2 o_{12}}{dt^2}$ for both OWs.

tive sign when the heater was switched on and with the opposite sign when the heat pulse was switched off. The same behaviour applies to both windows.

In the analysis of the glitches, $\frac{d^2 o_{12}}{dt^2}$ has been considered because is a cleaner signal than Δg_0, and for this time-scale, the interferometric differential distance, o_{12}, is not modified by the spacecraft's performance —see Section 2.3.1.

We base the analysis on the amplitude of the pulses as tagged in Figure 5.5. We have represented the amplitude of these glitches with the power injected by the heaters. We do a linear fit for the complete set of points including both OWs —see Figure 5.6— obtaining the following coefficients:

$$\frac{d^2 o_{12}}{dt^2} = a + b \cdot P, \tag{5.2}$$

$$a = (-2.7 \pm 0.7) \cdot 10^{-14}\ \mathrm{m\,s^{-2}}, \tag{5.3}$$

$$b = (3.010 \pm 0.005) \cdot 10^{-11}\ \mathrm{m\,s^{-2}\,W^{-1}}, \tag{5.4}$$

where the parameter b shows the coupling between both magnitudes, power and $\frac{d^2 o_{12}}{dt^2}$.

The next step in trying to understand the physical origin of the glitches is to set up a model which, as previously explained, will be based upon the assumption that the observed glitches are produced by forces induced by electromagnetic induction. In order to do so, we consider the heater as a small coil and that eddy currents can appear in the TMs [94] as a consequence of variations of magnetic flux (Lenz and Faraday's laws). We can write the peak of acceleration produced when we switch on/off the heaters as a function of the maximum power $P_{\max}$ reached in the injection as follows —see Appendix E:

$$\Delta g_{\text{induc}} = \frac{10^2 \cdot 3\mu_0^2}{4} \frac{\rho^4 z}{(\rho^2 + z^2)^4} \frac{(N \cdot S)^2}{R \cdot (t_{\text{h}} - t_{\text{TM}})} \cdot \frac{1}{R_{\text{h}} \cdot m_{\text{TM}}} \cdot$$

$$\cdot (1 - e^{-t/t_{\text{h}}}) \cdot (e^{-t/t_{\text{h}}} - e^{-t/t_{\text{TM}}}) \cdot P_{\max}, \tag{5.5}$$

where μ_0 is the magnetic permeability, ρ is the radius of the ring (the TM is considered like a ring), z is the distance between the heater and the TM, N the number of turns of the coil (heater), S is the modulus of the vector area of the coil, R_{h} is the resistance of the heater, R is the resistance of the TM, m_{TM} is the mass of the TM, t_{h} is the RC-time constant of the heater, and, finally, $t_{\text{TM}} = L/R$, with L the self-inductance of the TM.

Using the values for these parameters shown in Appendix E, we get the following equation:

$$\Delta g_{\text{induc}} = c_{\text{P}} \cdot P_{\max} \simeq 2.5 \cdot 10^{-12} \cdot P_{\max}. \tag{5.6}$$

Eq. (5.6) shows a linear relation between Δg_{induc} and the power injected by the heaters, $P_{\max}$, such as shown in Figure 5.6. As we see, the experimental value for the coupling between both magnitudes given in Eq. (5.4) is an order of magnitude bigger than the theoretical value shown in Eq. (5.6).

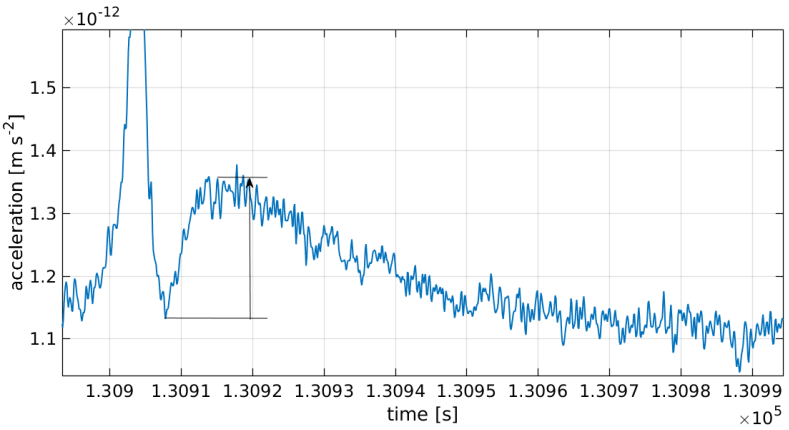

Figure 5.7: Δg_0 amplitude selected to be represented as a function of $\frac{d^2T}{dt^2}$, the second temperature derivative.

The model we have used is however based on several simplifications, as for instance the dipole approximation of the heater. A more refined numerical model should be put forward to completely check or discard the viability of the proposed hypothesis for the origin of the observed glitches.

5.3.2 Mid-term effect: Thermo-optical effect

In a 50 s time-scale we observe a response which, given the temperature profiles observed —see Figure 5.2—, can not be associated with the temperature itself but to the change in temperature. In Figure 5.7 we label the contribution being studied. The analysis was based on the amplitude as marked by these two labels for each one of the different runs. The points in Figure 5.8 have been obtained representing the second temperature derivative with the Δg_0 amplitude marked. T is the average temperature of the three temperatures measured with the three thermal sensors on the OW. Each point belongs to an independent heat pulse. In particular, only the runs at 0.1 and 1 mHz were taken into account since the effect was not measurable in the 20 mHz runs because the stimuli applied by the heaters were too fast.

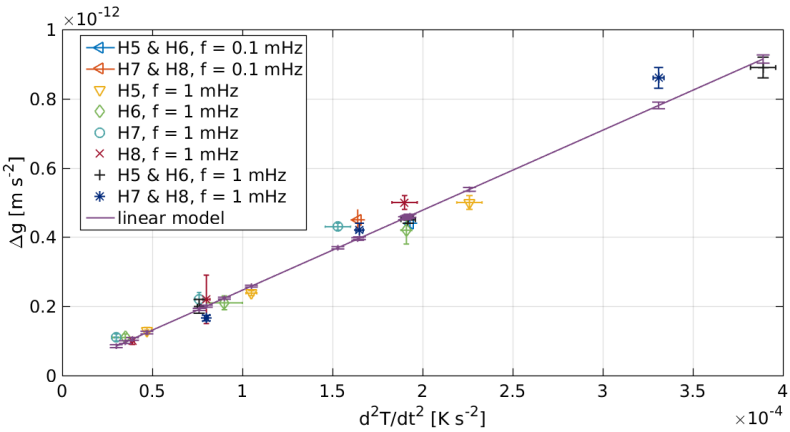

Figure 5.8: Linear fit between Δg_0 amplitude versus $\frac{d^2T}{dt^2}$ at 1 mHz and 0.1 mHz taking into account all the points for both OWs.

The following coefficients are obtained by means of a simple linear fit of the data —Figure 5.8:

$$\Delta g_0 = a + b \cdot \frac{d^2T}{dt^2}, \tag{5.7}$$

$$a = (1.5 \pm 0.5) \cdot 10^{-14}\ \mathrm{m\,s^{-2}}, \tag{5.8}$$

$$b = (2.31 \pm 0.04) \cdot 10^{-9}\ \mathrm{m\,K^{-1}}. \tag{5.9}$$

It is important to notice that the coupling obtained (the slope b) is in terms of displacement since Δg_0 is compared to double derivative of temperature. According to this, the effect would not be associated to a force contribution but to a displacement. This parameter b shows a number that would include the thermo-optical effects produced both by the stress between the Titanium flange and the glass, and by the refractive index change —see Section 3.1.2.

In order to get more accurate results we can not only consider each OW separately but also we can use a model that shows, separately as well, the two physical mechanisms that produce thermo-optical effects. Eqs. (5.10, 5.11) show the differential acceleration produced as a consequence of the

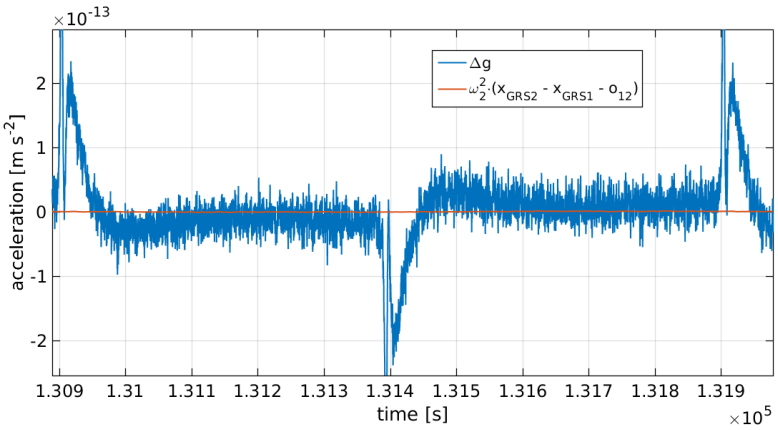

Figure 5.9: Δg_0 compared to the contribution given by the stiffness term $\omega_2^2 \cdot (x_{\mathrm{GRS2}} - x_{\mathrm{GRS1}} - o_{12})$ when we perform with both heaters an injection of 20 mW at 1 mHz on the OW2.

phase shift (path-length variation) suffered by stress between the Titanium ring and the glass of the OW, and the change of the refractive index of the glass when there are thermal fluctuations on the OWs. These are the terms $\ddot{o}_{\mathrm{OW1}}$ and $\ddot{o}_{\mathrm{OW2}}$ that appear in Eq. (5.1):

$$\ddot{o}_{\mathrm{OW1}} = c_{1,\mathrm{OW1}} \cdot \frac{d^2 TS_{\mathrm{cl,OW1}}}{dt^2} + c_{2,\mathrm{OW1}} \cdot \frac{d^2 TS24}{dt^2}, \tag{5.10}$$

$$\ddot{o}_{\mathrm{OW2}} = c_{1,\mathrm{OW2}} \cdot \frac{d^2 TS_{\mathrm{cl,OW2}}}{dt^2} + c_{2,\mathrm{OW2}} \cdot \frac{d^2 TS23}{dt^2}, \tag{5.11}$$

where $TS_{\mathrm{cl,OW1}}$ and $TS_{\mathrm{cl,OW2}}$ are either the temperature measured by the closest thermistor to the heater on when we activate one heater or the sum of the temperature measured by the two closest thermistors to the heaters when both heaters are activated —see Figure 5.1.

This model is composed of two terms, namely:

- The first term, since the temperatures are given by the closest thermistors to the heaters, allows to do a good estimation of the stress effect contribution because this physical mechanism is dominated mainly

Heater	Power [W]	c_1 [nm/K]	c_2 [nm/K]
H5 , H6 (OW1)	0.02×2	(0.97 ± 0.06)	(10.6 ± 0.7)
	0.05×2	(0.98 ± 0.06)	(10.7 ± 0.7)
	0.10×2	(0.99 ± 0.06)	(10.7 ± 0.7)
H5 (OW1)	0.02	(0.89 ± 0.05)	(11.4 ± 0.6)
	0.05	(0.89 ± 0.05)	(11.5 ± 0.6)
	0.10	(0.89 ± 0.05)	(11.5 ± 0.6)
H6 (OW1)	0.02	(1.01 ± 0.08)	(10.0 ± 0.8)
	0.05	(1.04 ± 0.08)	(10.4 ± 0.8)
	0.10	(1.05 ± 0.07)	(10.5 ± 0.8)
H7 , H8 (OW2)	0.02×2	(1.08 ± 0.06)	(9.4 ± 0.6)
	0.05×2	(1.08 ± 0.06)	(9.4 ± 0.6)
	0.10×2	(1.06 ± 0.07)	(9.1 ± 0.7)
H7 (OW2)	0.02	(1.16 ± 0.07)	(10.6 ± 0.6)
	0.05	(1.16 ± 0.07)	(10.9 ± 0.6)
	0.10	(1.17 ± 0.07)	(10.8 ± 0.6)
H8 (OW2)	0.02	(0.99 ± 0.06)	(9.1 ± 0.6)
	0.05	(1.00 ± 0.06)	(9.1 ± 0.6)
	0.10	(1.01 ± 0.06)	(9.1 ± 0.6)

Table 5.2: Fit between the second temperature derivative and $\Delta g_0 + \omega_2^2 \cdot (x_{\mathrm{GRS2}} - x_{\mathrm{GRS1}} - o_{12})$ (we have subtracted $\omega_2^2 \cdot (x_{\mathrm{GRS2}} - x_{\mathrm{GRS1}} - o_{12})$) for different thermal injections at 1 mHz on the OW1 and the OW2. In the case of $c_{1,\mathrm{OW1}}$ and $c_{1,\mathrm{OW2}}$, we consider the temperature of the closest thermistor to the switched-on heater when we activate one heater, and the sum of temperatures of the two closest thermistors to the heaters when we activate both heaters. In the case of $c_{2,\mathrm{OW1}}$ and $c_{2,\mathrm{OW2}}$, we consider the temperature measured by the thermistor on the top of the OW —see Figure 5.1.

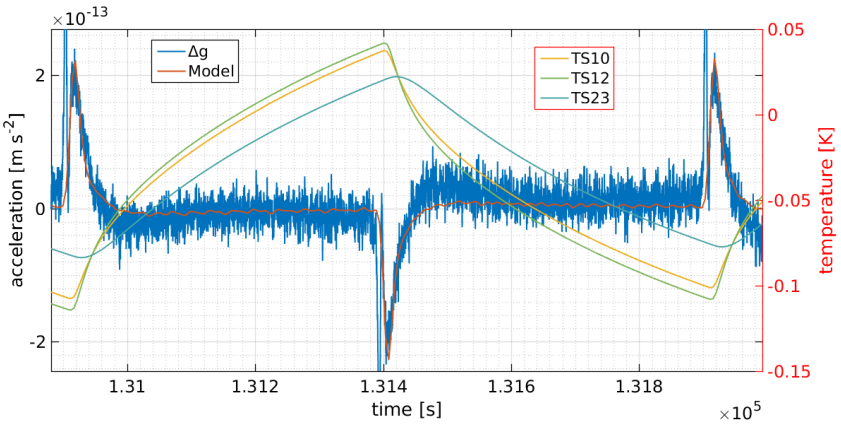

Figure 5.10: Fit for one pulse of $\Delta g_0 + \omega_2^2 \cdot (x_{\mathrm{GRS2}} - x_{\mathrm{GRS1}} - o_{12})$ (we have subtracted $\omega_2^2 \cdot (x_{\mathrm{GRS2}} - x_{\mathrm{GRS1}} - o_{12})$) when we do with both heaters an injection of 20 mW at 1 mHz on the OW2. We have put the sampling frequency for doing the fit at 0.2 Hz because is the sampling frequency of the temperature. We have applied a low-pass filter of order 1 at 0.1 Hz as cut-off frequency to the signal Δg_0, obtaining the blue line of this figure.

by the Titanium temperature and not by the glass temperature. As we saw in Section 3.1.2, this effect would be more prominent in the first moments since the injection, when the temperature fluctuations appear on the Titanium and not on the glass.

- The second term gives a good approximation to the contribution given by changes of the refractive index of the glass since the considered sensor is further away from the heater. This thermistor gives a measurement that is a low-pass version of the measurement obtained with the two closest sensors. Hence, the temperature considered in this term would resemble to the glass temperature (once the thermal fluctuations reach it) and this temperature dominates the thermo-optical effect produced by changes in the refractive index. A part of stress effect will also appear in this term because there is a small component when the thermal fluctuations are uniform throughout the window —see Section 3.1.2.

Therefore, we can use the previous equations to obtain the coupling factors by means of a fit to the differential acceleration, Δg_0 — see Figure 5.4. Before fitting, the term $\omega_2^2 \cdot (x_{\mathrm{GRS2}} - x_{\mathrm{GRS1}} - o_{12})$ (stiffness between the GRSs and the OB) that appears in Eq. (5.1) has been subtracted of Δg_0 to have a cleaner signal, although this term is very small, as we can see in Figure 5.9. Results on Table 5.2 have been obtained for the injections at 1 mHz (where this thermo-optical contribution is clearer than for the other injections). On the one hand, the parameters $c_{1,\mathrm{OW1}}$ and $c_{1,\mathrm{OW2}}$ show the path-length variation induced by the stress mechanism. We previously stated that this mechanism is dominated by the Titanium temperature, being more relevant when the temperature fluctuations appear on the Titanium and not on the glass, in the first moments since the injection. The values obtained are in agreement with the measurements from ground experiments, which give values for this contribution between $8.5 \cdot 10^{-10} - 5.1 \cdot 10^{-9}$ m/K considering that the beam passes twice through the window [65]. On the other hand, the parameters $c_{2,\mathrm{OW1}}$ and $c_{2,\mathrm{OW2}}$ show the path-length variation induced by the change of the refractive index. These parameters depend on a temperature that, as mentioned before, we can resemble to the glass temperature, which dominates that physical mechanism. The stress effect will also appear because there is a small component when the thermal fluctuations are uniform throughout the window. Again, the values obtained are in agreement with the ones obtained by on-ground experiments($\approx 1 \cdot 10^{-8}$ m/K considering that the beam passes twice through the window) [65].

5.3.3 Long-term effect: Force on the Test Masses

We performed the same simple analysis but now for the 5000 s variation in Δg_0. In Figure 5.11 we can see that the response in terms of differential acceleration has a profile very similar to the temperature profile measured by the thermistors, hence, in this case, we look for coupling between Δg_0 and temperature. This contribution would be included in Δg_0 in Eq. (5.1) because it produces real forces on the TMs.

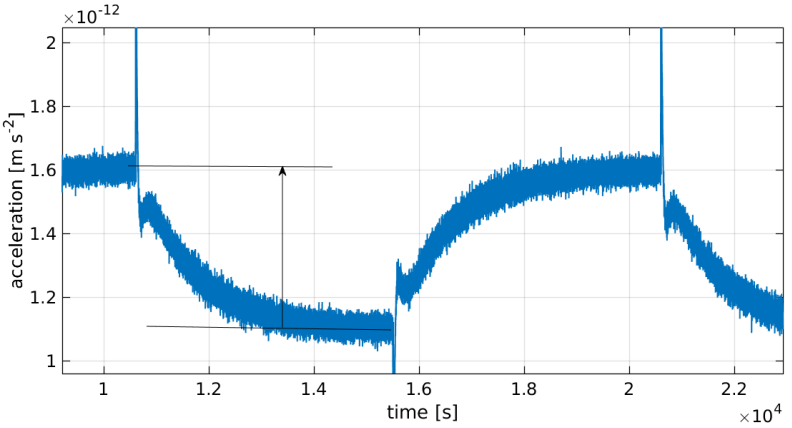

Figure 5.11: Δg_0 amplitude selected to be represented as a function of T.

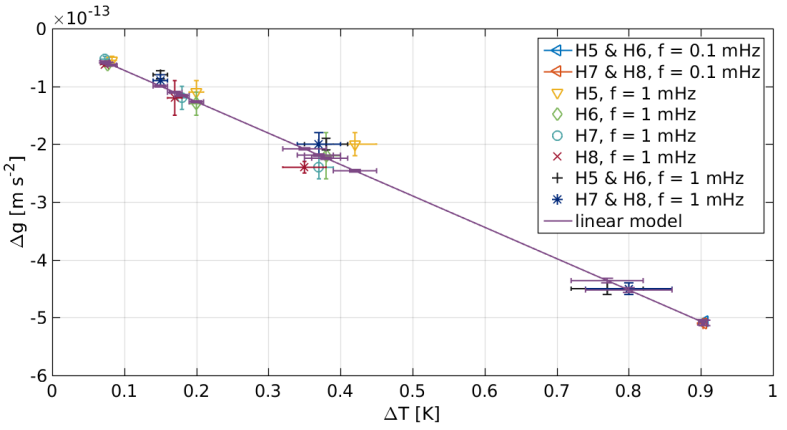

Figure 5.12: Linear fit between Δg_0 amplitude versus temperature amplitude at 1 mHz and 0.1 mHz taking into account all the points for both OWs.

As we did in the previous section, we represent each heat pulse Δg_0 as a function, in this case of T, being T the amplitude of the average temperature of the three thermistors at each OW. A linear fit —Figure 5.12— can be made using:

$$\Delta g_0 = a + b \cdot T. \tag{5.12}$$

The following coefficients are obtained from the fit:

$$a = (-1.8 \pm 0.2) \cdot 10^{-14}\,\mathrm{m\,s^{-2}}, \tag{5.13}$$

$$b = (-5.43 \pm 0.06) \cdot 10^{-13}\,\mathrm{m\,s^{-2}\,K^{-1}}, \tag{5.14}$$

being the parameter b the coupling between both magnitudes. This relationship shows a coupling factor with the temperature that produces a real force contribution (it will appear in Δg_{te} —see Eq. (5.1)).

We can perform a fit of Δg_0 for the injections at 0.1 mHz, where this effect appears clearer, using the average temperature of the three sensors but, to be more precise, considering each OW separately. In addition, we subtract the term $\omega_2^2 \cdot (x_{\mathrm{GRS2}} - x_{\mathrm{GRS1}} - o_{12})$ (stiffness between the GRSs and the OB) that appears in Eq. (5.1). In this case this term is more relevant in the sense that its time-scale is the time-scale of the effect considered in this section. However, it is smaller than the complete perturbation observed, as seen in Figure 5.13. The origin of this stiffness term is discussed taking into account several noise runs as well as these injections carried out at 0.1 mHz on the OWs in Appendix **??** . The conclusion derived from this study is that the heating of the slab that joins the GRSs with the OB is the main responsible for producing the relative displacements between both. The following coefficients are obtained from the fit:

OW1:

$$\Delta g_0 = c_{\mathrm{long,OW1}} \cdot T_{\mathrm{OW1}} \qquad T_{\mathrm{OW1}} = \frac{TS9 + TS11 + TS24}{3}, \tag{5.15}$$

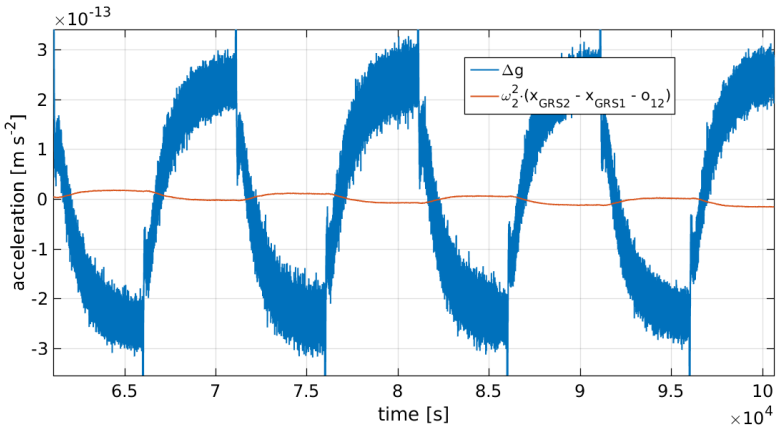

Figure 5.13: Δg_0 compared to the contribution given for the stiffness term $\omega_2^2 \cdot (x_{\mathrm{GRS2}} - x_{\mathrm{GRS1}} - o_{12})$ for the runs at 0.1 mHz for the OW2.

$$c_{\mathrm{long,OW1}} = \frac{d\Delta g_0}{dT_{\mathrm{OW1}}} = \frac{d\Delta g_{\mathrm{te}}}{dT_{\mathrm{OW1}}} =$$
$$= (-5.27 \pm 0.02) \cdot 10^{-13}\,\mathrm{m\,s^{-2}\,K^{-1}}. \tag{5.16}$$

OW2:

$$\Delta g_0 = c_{\mathrm{long,OW2}} \cdot T \qquad T = \frac{TS10 + TS12 + TS23}{3}, \tag{5.17}$$

$$c_{\mathrm{long,OW2}} = \frac{d\Delta g_0}{dT_{\mathrm{OW2}}} = \frac{d\Delta g_{\mathrm{te}}}{dT_{\mathrm{OW2}}} =$$
$$= (-5.07 \pm 0.02) \cdot 10^{-13}\,\mathrm{m\,s^{-2}\,K^{-1}}. \tag{5.18}$$

Figure 5.14 shows the fit. Some physical mechanisms inside the EH like outgassing could explain this contribution at low frequencies [31]. Indeed, the outgassing in the vacuum enclosures produced pressure gradients that fluctuated with temperature, and that could explain what we observe when the OWs are heated. It is important to notice that this effect appeared only during OW heating. Hence, in conditions where a gradient is introduced across the enclosure. There was no experiment heating the vacuum enclosure from where we could draw conclusions of what this effect would be in

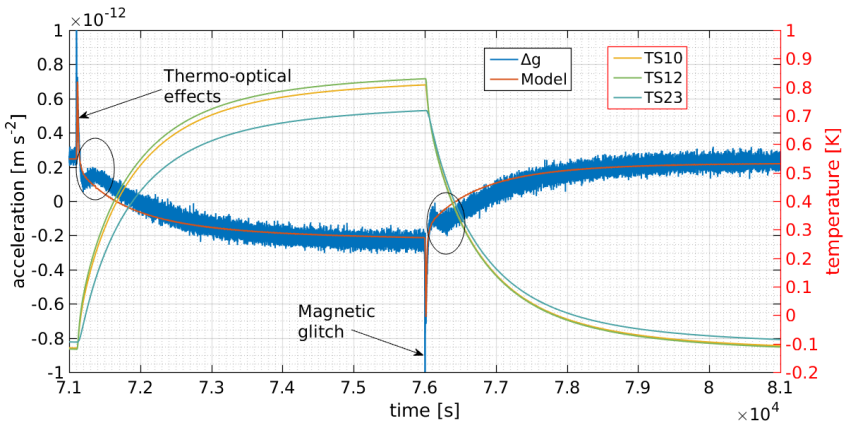

Figure 5.14: Fit (red line) between $\Delta g_0 + \omega_2^2 \cdot (x_{\mathrm{GRS2}} - x_{\mathrm{GRS1}} - o_{12})$ (we have subtracted $\omega_2^2 \cdot (x_{\mathrm{GRS2}} - x_{\mathrm{GRS1}} - o_{12})$) and the OW2 average temperature for the runs at 0.1 mHz for the OW2 —see Eqs. (5.15, 5.17). We have put the sampling frequency for doing the fit at 0.2 Hz because is the sampling frequency of the temperature. We have applied a low-pass filter of order 1 at 0.1 Hz as cut-off frequency to the signal Δg_0, obtaining the blue line of this figure. In addition, we can see red glitches in the model that correspond to the thermo-optical effects fitted by using the Eq. (5.11).

that case. Also, in Figure 5.14 we can see the thermo-optical effects that we have fitted taking into account the model shown in the previous section (red spikes) —see Eq. (5.11).

However, we do not have a complete fit of the signal because when we pass from the mid time-scale to the long time-scale —see Figure 5.14— there is a modulation (inside the black circles in the plot) that we do not get to explain with the Eqs. (5.11, 5.18). In the following subsection we present a phenomenological model to fit the complete Δg signal.

5.3.4 Phenomenological model for the Optical Windows

In order to fit the complete Δg signal produced when there were thermal fluctuations on the OWs, we can use the following phenomenological model for each OW:

$$\Delta g_0 + \omega_2^2 \cdot (x_{\mathrm{GRS2}} - x_{\mathrm{GRS1}} - o_{12}) = c_{1,\mathrm{OW1}} \cdot \frac{d^2 TS_{\mathrm{cl,OW1}}}{dt^2} + c_{2,\mathrm{OW1}} \cdot \frac{d^2 TS24}{dt^2}$$

$$+k_{1,\mathrm{OW1}} \cdot \frac{dTS24}{dt} + k_{2,\mathrm{OW1}} \cdot TS_{\mathrm{cl,OW1}} + k_{3,\mathrm{OW1}} \cdot TS24, \tag{5.19}$$

$$\Delta g_0 + \omega_2^2 \cdot (x_{\mathrm{GRS2}} - x_{\mathrm{GRS1}} - o_{12}) = c_{1,\mathrm{OW2}} \cdot \frac{d^2 TS_{\mathrm{cl,OW2}}}{dt^2} + c_{2,\mathrm{OW2}} \cdot \frac{d^2 TS23}{dt^2}$$

$$+k_{1,\mathrm{OW2}} \cdot \frac{dTS23}{dt} + k_{2,\mathrm{OW2}} \cdot TS_{\mathrm{cl,OW2}} + k_{3,\mathrm{OW2}} \cdot TS23, \tag{5.20}$$

where the first two terms in the right side are those shown in Eqs. (5.11, 5.11). The coefficients $k_{1,\mathrm{OW2}}$ and $k_{1,\mathrm{OW2}}$ show a relationship with the first temperature derivative measured at the top of each OW. These terms could indicate that when the stress between the glass and the Titanium disappears, these materials try to return to their initial state before the thermal fluctuation, but this recovery is attenuated with respect to the deformation process they have suffered. Finally, the last two coefficients, $k_{2,\mathrm{OW1}}$ and $k_{3,\mathrm{OW1}}$ for the OW1, and $k_{2,\mathrm{OW2}}$ and $k_{3,\mathrm{OW2}}$ for the OW2, depend on the temperature given by the sum of the temperature measured by the two

	c_1 [nm K^{-1}]	c_2 [nm K^{-1}]	k_1 [nm s^{-1} K^{-1}]	k_2 [pm s^{-2} K^{-1}]	k_3 [pm s^{-2} K^{-1}]
OW1	(0.75 ± 0.06)	(6.6 ± 0.7)	(-0.66 ± 0.01)	(2.50 ± 0.05)	(-6.6 ± 0.1)
OW2	(0.85 ± 0.02)	(7.4 ± 0.2)	(-0.61 ± 0.01)	(2.70 ± 0.05)	(-6.8 ± 0.1)

Table 5.3: Parameters of the fit obtained using the phenomenological model given by Eqs. (5.19, 5.20). We have taken into account the injections at 0.1 mHz.

closest thermistors to the heaters ($k_{2,\mathrm{OW1}}$ and $k_{2,\mathrm{OW2}}$) and the temperature given by the sensor at the top of the OW ($k_{2,\mathrm{OW1}}$ and $k_{2,\mathrm{OW2}}$). These terms, being proportional to the temperature, would be related to some physical mechanism within the vacuum chamber that would produce a real force on the TMs.

Using the Eqs. (5.19, 5.20), we have obtained the coefficients shown in Table 5.3 when we fit $\Delta g_0 + \omega_2^2 \cdot (x_{\mathrm{GRS2}} - x_{\mathrm{GRS1}} - o_{12})$ (Δg signal to which we have subtracted $\omega_2^2 \cdot (x_{\mathrm{GRS2}} - x_{\mathrm{GRS1}} - o_{12})$). We have considered the injections at 0.1 mHz since in these injections we clearly observe all the effects involved —see Figure 5.14. Figure 5.15 has been obtained by means of this fit.

Looking at Table 5.3, we can see how the first two parameters of these fits are slightly smaller than those observed in Table 5.2, when we only fitted the signal with the model given by Eqs. (5.10, 5.11) (thermo-optical effects). This is an indication that both the proportional term to the first temperature derivative as the two terms proportional to the second temperature derivative are mixed, that is, there are moments where the different physical effects occur at the same time. The same applies to the terms proportional to k_2 and k_3 that also influence the part of the signal inside the circles shown in Figure 5.14. These last terms have to replace the term seen in Eqs. (5.15, 5.17) because there seems to be some effect related to the thermal gradient of the temperatures $TS_{\mathrm{cl,OW1}}$ and $TS24$ for the OW1, and $TS_{\mathrm{cl,OW2}}$ and $TS23$ for the OW2.

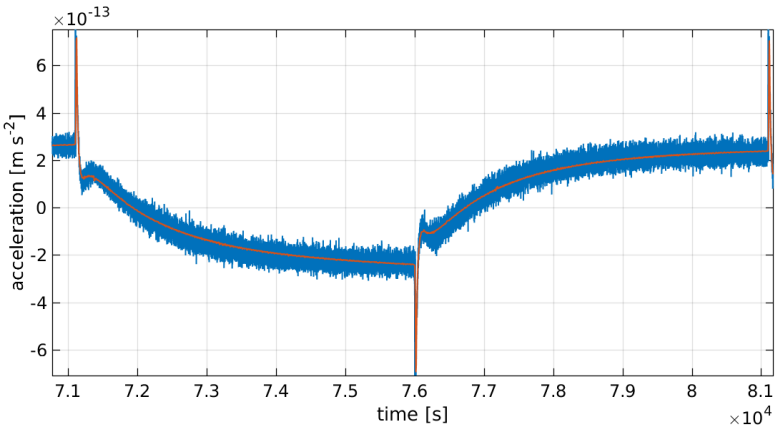

Figure 5.15: Fit (red line) using the phenomenological model to $\Delta g_0 + \omega_2^2 \cdot (x_{\mathrm{GRS2}} - x_{\mathrm{GRS1}} - o_{12})$ (we have subtracted $\omega_2^2 \cdot (x_{\mathrm{GRS2}} - x_{\mathrm{GRS1}} - o_{12})$) for the runs at 0.1 mHz for the OW2 —see Eqs. (5.19, 5.20). We have put the sampling frequency for doing the fit at 0.2 Hz because is the sampling frequency of the temperature. We have applied a low-pass filter of order 1 at 0.1 Hz as cut-off frequency to the signal Δg_0, obtaining the blue line of this figure.

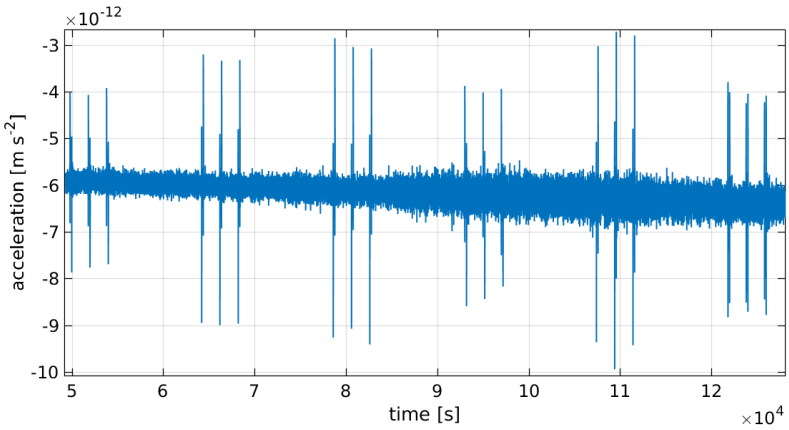

Figure 5.16: Complete Δg_0 for the strut experiment.

This model seems to fit the entire signal completely, including the parts inside the circles in Figure 5.14. Nevertheless, this is a phenomenological model that needs to be studied more deeply and from which we can try to disentangle everything that seems to occur when there are thermal fluctuations in the OWs, especially for injections at very low frequencies (0.1 mHz in our case).

5.4 Strut thermal experiment results

The aim of this set of runs was to produce changes in Δg_0 coming from thermo-elastic effects, estimating the contribution of $\ddot{o}_{\mathrm{STR}}$ in Eq. (5.1). As in the OW case, when heating the struts there were other effects acting on the system. In this case, by looking at Figure 5.16 we observe that Δg_0 shows two effects with different time-scales, namely:

- A pronounced glitch when we switch on and when we switch off the heater, which, as previously described, we assign to eddy currents on the TM that appeared because of the variation of the magnetic flux. These eddy currents induced a magnetic field on the TM that opposed

TS	Power [W]	d^2o_{12}/dt^2 [ms^{-2}]	d^2o_{12}/dt^2/Power [ms^{-2}W^{-1}]
TS17	$(2.4416 \pm 0.0007) \cdot 10^{-1}$	$(-1.90 \pm 0.02) \cdot 10^{-12}$	$(-7.78 \pm 0.08) \cdot 10^{-12}$
TS18	$(2.5106 \pm 0.0004) \cdot 10^{-1}$	$(1.25 \pm 0.04) \cdot 10^{-12}$	$(5.0 \pm 0.2) \cdot 10^{-12}$
TS19	$(2.4412 \pm 0.0006) \cdot 10^{-1}$	$(-1.71 \pm 0.03) \cdot 10^{-12}$	$(-7.0 \pm 0.1) \cdot 10^{-12}$
TS20	$(2.5132 \pm 0.0007) \cdot 10^{-1}$	$(-1.79 \pm 0.03) \cdot 10^{-12}$	$(-7.1 \pm 0.1) \cdot 10^{-12}$
TS21	$(2.443 \pm 0.001) \cdot 10^{-2}$	$(1.376 \pm 0.006) \cdot 10^{-12}$	$(5.63 \pm 0.02) \cdot 10^{-12}$
TS22	$(2.5115 \pm 0.0007) \cdot 10^{-2}$	$(-1.71 \pm 0.05) \cdot 10^{-12}$	$(-7.0 \pm 0.2) \cdot 10^{-12}$

Table 5.4: Power, second derivative of o_{12}, and the coefficient between both for different thermal injections on the struts. As shown the coefficient signs, sometimes the force on the TMs has one direction and another times the opposite direction.

the incoming magnetic field and that generated a force on the mass. This effect is similar to what was observed for the OWs.

- The rest of the signal has a shape that we can relate either with thermo-elastic distortions along the struts or with the heating of other parts as the OB or junctions between struts and the OB, among others. Both possibilities generate motions of the OB that in turn change the path length of the interferometric signal producing an imaginary movement of the TM [44], and, hence, producing the actuation of the spacecraft.

5.4.1 Glitches

In the same way as in the OW case, the magnetic field generated on the TM during the switch on/off moments can produce a force on it —see Appendix E—, being the acceleration given by Eq. (5.5). The difference with respect to the OWs is the distance between the heaters (on the struts for this case) and the TMs. We could consider an average distance —see Figure 3.4— of 13 cm between the heater and the TM, which gives the following value for the coefficient c_{P} —see Appendix E—:

$$\Delta g_{\mathrm{induc}} = c_{\mathrm{P}} \cdot P_{\mathrm{max}} \simeq 2 \cdot 10^{-13} \cdot P_{\mathrm{max}}. \tag{5.21}$$

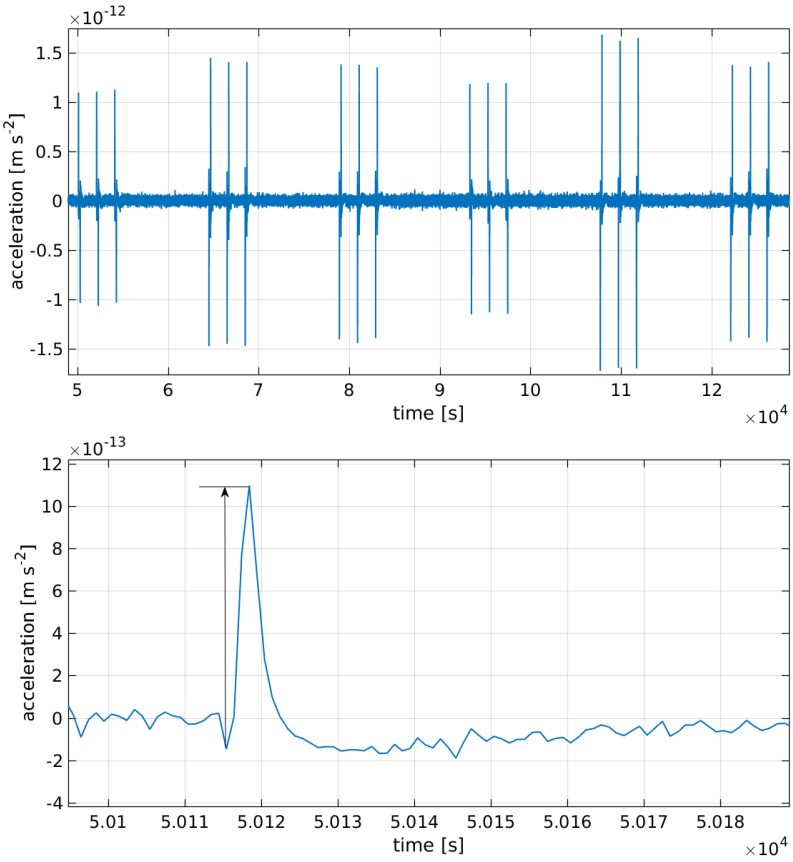

Figure 5.17: *Top*: $\frac{d^2 o_{12}}{dt^2}$ for the injections. *Bottom*: Amplitude selected for $\frac{d^2 o_{12}}{dt^2}$.

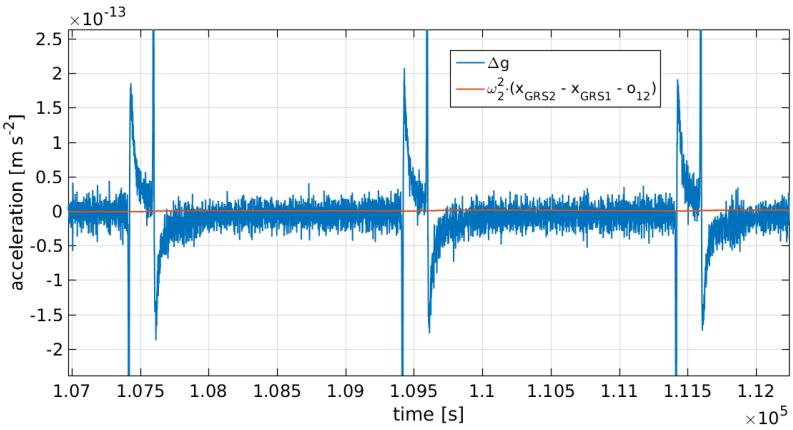

Figure 5.18: Δg_0 compared to the contribution given for the stiffness term $\omega_2^2 \cdot (x_{\mathrm{GRS2}} - x_{\mathrm{GRS1}} - o_{12})$ when we switched on and off the heater that was located on the strut where was the thermistor TS17.

It is important to notice that unlike the OW, where we had several injections with different powers, here we only had one injection at a single power, therefore, we can not get a line like the one plotted in Figure 5.6 but it is possible to calculate the different couplings between the amplitude of the glitches for $\frac{d^2 o_{12}}{dt^2}$ —see Figure 5.17— and the power injected by the heaters. We can observe that the order of magnitude for the parameter c_{P} in Eq. (5.21) is an order of magnitude smaller than the values shown in Table 5.4. It is due to the complexity of the real problem, as we commented for the OW case.

5.4.2 Thermo-elastic effects on the struts

In order to explain the thermo-elastic distortion, the following model has been used to perform a fit:

$$\ddot{o}_{\mathrm{STR}} = c_{\mathrm{STR}} \cdot \frac{d^2 lp(T, f_{\mathrm{c}})}{dt^2}, \tag{5.22}$$

where T is the temperature increase measured by the sensor closest to the heater during the injection, and f_{c} is the cut-off frequency of the low-pass

TS	c_{STR} [m/K]	f_{c} [Hz]
TS17	$(1.6 \pm 0.2) \cdot 10^{-9}$	$(1.0 \pm 0.2) \cdot 10^{-3}$
TS18	$(-1.3 \pm 0.1) \cdot 10^{-9}$	$(1.1 \pm 0.1) \cdot 10^{-3}$
TS19	$(1.5 \pm 0.1) \cdot 10^{-9}$	$(1.3 \pm 0.1) \cdot 10^{-3}$
TS20	$(1.4 \pm 0.2) \cdot 10^{-9}$	$(1.0 \pm 0.2) \cdot 10^{-3}$
TS21	$(-1.5 \pm 0.1) \cdot 10^{-9}$	$(1.3 \pm 0.1) \cdot 10^{-3}$
TS22	$(1.3 \pm 0.1) \cdot 10^{-9}$	$(1.3 \pm 0.1) \cdot 10^{-3}$

Table 5.5: Parameters obtained using the thermo-elastic strut model to perform a fit. The coefficient signs (there are four positives and two negatives) can be explained by means of an OB torsion along the y-axis produced by the elongation of the strut.

filter used in the model, such that if f_{c} is bigger than the characteristic frequency of the strut, the effect will be due to the elongation of the strut and not to the heating of other parts, and if it is smaller, the effect will be due to the heating of other parts. Hence, the low-pass filter will say us where the thermal fluctuation responsible of the path-length variation is acting —see Appendix F.

Therefore, by fitting the signal Δg_0, Table 5.5 has been obtained. This shows the value obtained for the two coefficients in Eq. (5.22) for each injection —see Figure 5.19. Before performing the fit, the term $\omega_2^2 \cdot (x_{\mathrm{GRS2}} - x_{\mathrm{GRS1}} - o_{12})$ has been subtracted to Δg_0 to have a cleaner signal —see Figure 5.18.

As seen in Table 5.5, $0.00081\,\mathrm{Hz} < f_{\mathrm{c}} < 0.0024\,\mathrm{Hz}$, being 0.00081 Hz —see Eq. (F.1)— the characteristic frequency for the complete strut (half of the central part of CFRP and one Titanium end fitting since the heaters are located in the strut center), and 0.0024 Hz —see Eq. (F.2)— the characteristic frequency considering only half of the CFRP part [46] —see Appendix F. Each of these characteristic frequencies is the cut-off frequency for the low-pass filter for every of the two parts commented before. Hence, our

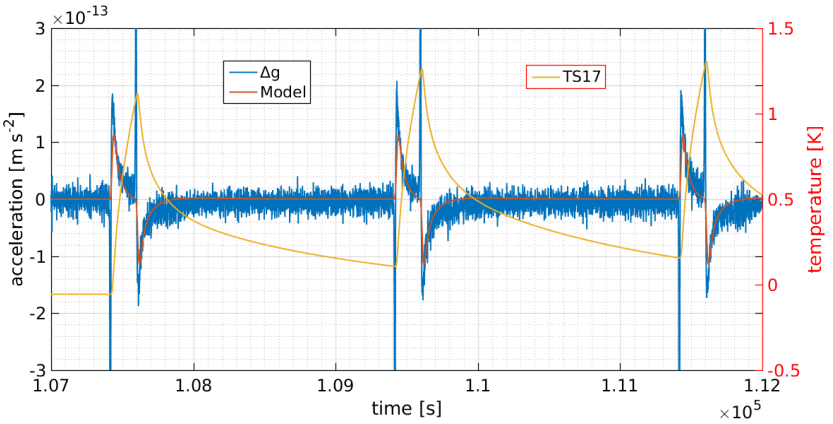

Figure 5.19: Fit for $\Delta g_0 + \omega_2^2 \cdot (x_{\mathrm{GRS2}} - x_{\mathrm{GRS1}} - o_{12})$ (we have subtracted $\omega_2^2 \cdot (x_{\mathrm{GRS2}} - x_{\mathrm{GRS1}} - o_{12})$) when we switched on and off the heater that was located on the strut where the TS17 thermistor was located. We have put the sampling frequency for doing the fit at 0.2 Hz because is the sampling frequency of the temperature. We have applied a low-pass filter of order 1 at 0.1 Hz as cut-off frequency to the signal Δg_0, obtaining the blue line of this figure.

analysis points towards the two Titanium end fittings as the responsible of the thermo-elastic distortion.

The values in Table 5.5, that for four cases are positives and for two cases are negatives, show that the elongation of the two Titanium end fittings produce an OB torsion along the y-axis. It is in agreement with the results found in [44].

5.4.3 Responses of the static interferometers

In Section 2.2.1 we commented that in the OB there were four different interferometer measurements. Two of them provided two distances: $x1$, the distance between the TM1 and the OB, and $x12$, the distance between both TMs. The other two were: the reference interferometer, which was sensitive to the path-length noise produced outside the OB and whose signal was removed in the rest of the interferometric measurements; and the frequency interferometer, sensitive to frequency fluctuations of the laser beam. Since the light does not go out of the bench, any variation in angles points towards a mechanical distortion.

The reference interferometer was used to stabilise the optical path-length difference (OPD) between fibres [48]. The bottom line in Figure 5.20 shows that the reference interferometer was sensitive to the thermal signals injected by the heaters, although these disturbances are removed in the final read-out, top plot in Figure 5.20. We also observe that the activation of H9 produces a larger response, what could be due to the fact that this heater was very close to optical fibres, as shown in Figure 5.21.

On the other hand, the top part in Figure 5.22 shows the frequency interferometer read-out once we subtract the reference measurement. We can observe a clear signal for each thermal injection. The bottom part in the figure provides the signal used by the two different ways to control the frequency fluctuations, namely: a piezoelectric transducer to stabilise

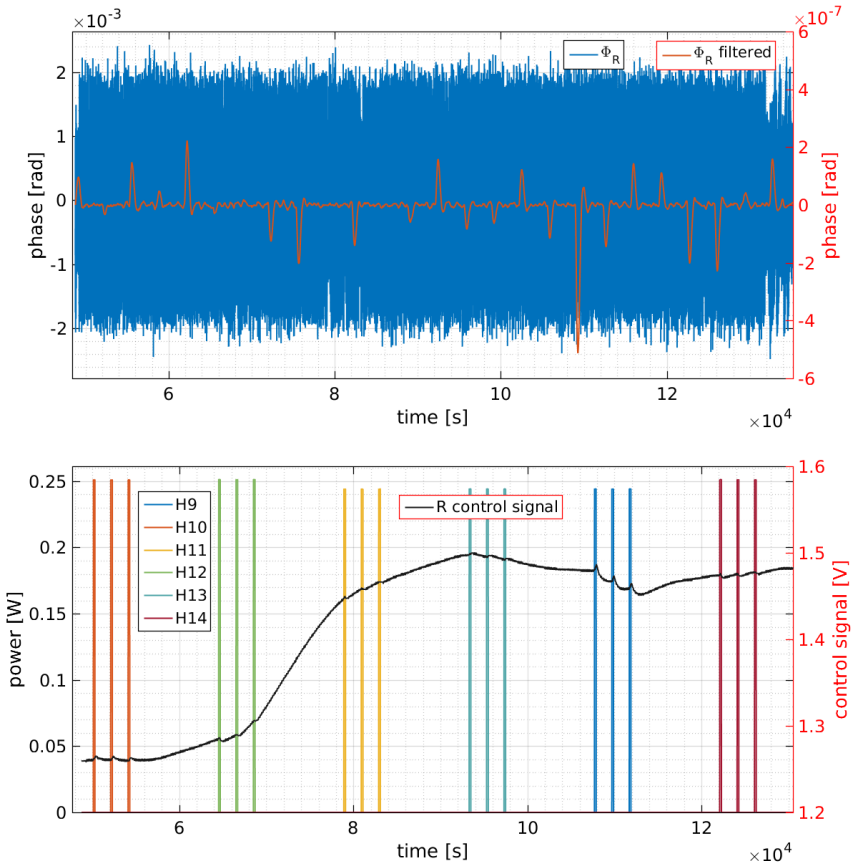

Figure 5.20: *Top*: Read-outs of the reference interferometer Φ_{R} and the same measurement filtered with a 3rd order low-pass filter with a cut-off frequency of 1 mHz. *Bottom*: OPD control signal applied to the piezo actuator that controls the differential optical path-length fluctuations.

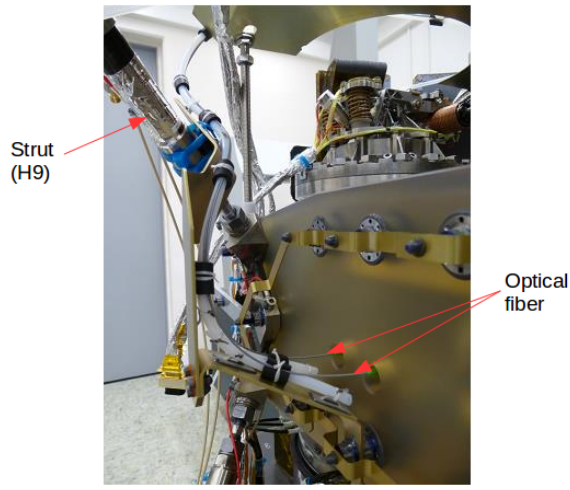

Figure 5.21: Detail of a lateral view of the LTP during integration. The picture shows the optical fiber routing and its close passage through the strut where the heater H9 was attached.

high-frequency fluctuations and a thermal control loop to regulate the low-frequency oscillations by controlling the temperature at the laser head, being the fast controller nested inside the loop of the slow controller [48]. The fact of observing signal produced by the heat injections for the frequency interferometer means that there was a disturbance in the OB since this interferometer only provides disturbances in the OB.

Figure 5.23 shows the DC vertical and horizontal angles of the reference and frequency interferometers —see Section 2.2.1. They show a pattern of signs, [- + + - + +], coherent with the observed one in Δg and o_{12}, which could be explained by means of an OB torsion along the y-axis produced by a force exerted by the strut —Figure 5.24— in turn caused by the elongation of itself [44]. Hence, by observing these responses of the static interferometers we conclude, as in the previous section, that an elongation in the strut is the main responsible of the path-length variation, in particular an elongation of the two Titanium end fittings.

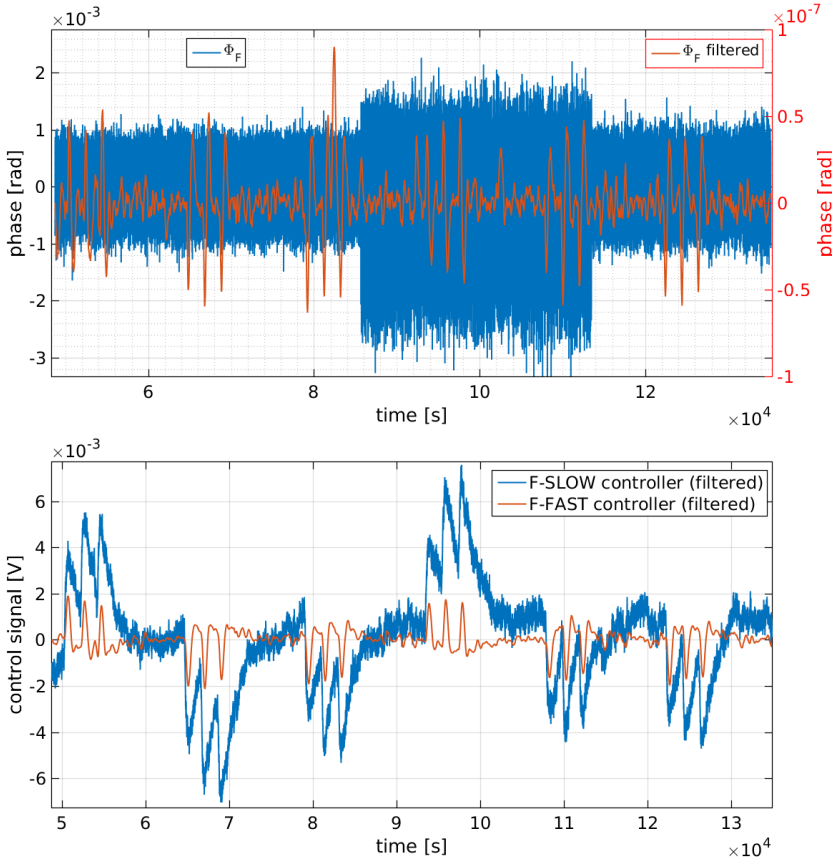

Figure 5.22: *Top*: Read-outs of the frequency interferometer Φ_F and the same measurement filtered with a 3rd order low-pass filter with a cut-off frequency of 1 mHz. *Bottom*: Control signals applied to the actuators for frequency noise stability.

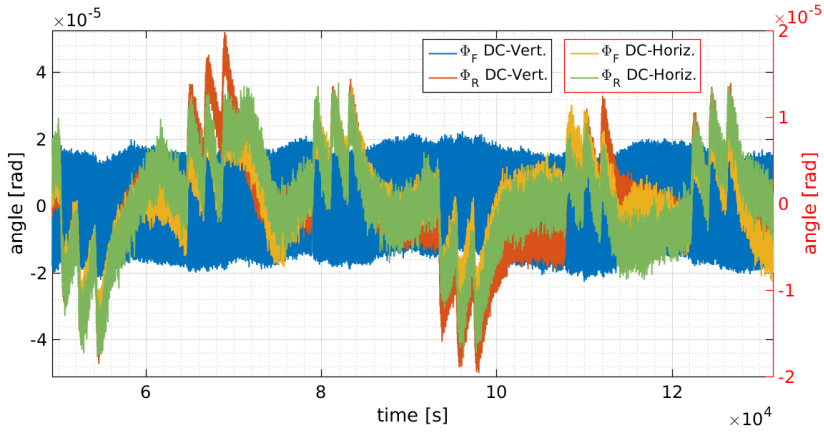

Figure 5.23: DC angles of the vertical and horizontal incident beams on the reference and frequency interferometers, after a 1st order detrend.

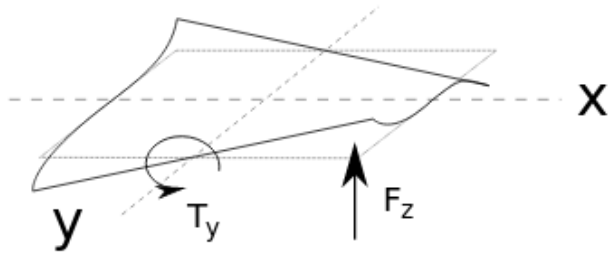

Figure 5.24: Schematic of the torsion mechanism on y produced by the vertical component of the force exerted by a heated strut. The case of the image would correspond to a lower strut heater activation such H11 or H14. This distortion mechanism is coherent with the observations. Image obtained from [44].

5.5 Thermo-elastic and thermo-optical noise projection

Considering the thermo-optical and the thermo-elastic contributions obtained by using Eqs. (5.10, 5.11) for the OWs and by using Eq. (5.22) for the struts, it is possible to estimate the noise contribution coming from these types of distortions.

The expressions to calculate the acceleration noise as a function of the noise measured by the thermistors in the case of the OWs are given by:

$$S^{1/2}_{\ddot{o}_{\mathrm{OW1}}}(f) = c_{1,\mathrm{OW1}}(2\pi f)^2 S^{1/2}_{TS_{\mathrm{cl,OW1}}}(f) + c_{2,\mathrm{OW1}}(2\pi f)^2 S^{1/2}_{TS24}(f), \tag{5.23}$$

$$S^{1/2}_{\ddot{o}_{\mathrm{OW2}}}(f) = c_{1,\mathrm{OW2}}(2\pi f)^2 S^{1/2}_{TS_{\mathrm{cl,OW2}}}(f) + c_{2,\mathrm{OW1}}(2\pi f)^2 S^{1/2}_{TS23}(f), \tag{5.24}$$

being $S^{1/2}_{\ddot{o}_{\mathrm{OW1}}}(f)$ and $S^{1/2}_{\ddot{o}_{\mathrm{OW2}}}(f)$ the ASD for each OW due to thermo-optical deformations, $S^{1/2}_{TS_{\mathrm{cl,OW1}}}(f)$ and $S^{1/2}_{TS_{\mathrm{cl,OW2}}}(f)$ the ASD for the sum of temperatures of the two closest sensors to the heaters for each OW, and $S^{1/2}_{TS23}$ and $S^{1/2}_{TS24}$ the ASD of the temperature measured by the sensor located on the top of the OW1 and OW2, respectively.

Regarding the coefficients used in these projections, we have considered the average amount of the values shown in Table 5.2. The values are shown in Table 5.6.

On the other hand, the equation to see the thermo-elastic noise produced by the struts is given by:

$$S^{1/2}_{\ddot{o}_{\mathrm{STR}}}(f) = c_{\mathrm{STR}}(2\pi f)^2 S^{1/2}_{TS}(f), \tag{5.25}$$

	c_1 [nm/K]	c_2 [nm/K]
OW1	(0.97 ± 0.02)	(10.8 ± 0.2)
OW2	(1.08 ± 0.02)	(9.7 ± 0.3)

Table 5.6: Average values of the coefficients of the thermo-optical model for both OWs —see Table 5.2.

being $S^{1/2}_{\ddot{o}_{\rm STR}}(f)$ the ASD for each strut coming from thermo-elastic deformations. For each strut we use the values shown in Table 5.5, doing a correlated sum to calculate the total noise coming from all struts.

Selecting a long segment of noise measured during February 14th-27th, 2017 and taking into account the temperature spectra explained in Section 4.2.1 and shown in Figure 4.3, we get the lines plotted in Figure 5.25. As seen, these thermo-optical and thermo-elastic contributions are not as relevant as, for example, the Brownian noise, but it is necessary to know them because the future LISA mission will be also affected by them. The thermo-elastic effect is more important than the contribution coming from thermo-optical effects, however, unlike the OWs that will be present in LISA, the link of the OB with the thermal shield (the struts for LPF) will not be as for LPF, although this analysis will serve to predict as best as possible what noise is introduced in the instrument as a result of thermo-elastic distortions.

Furthermore, Figure 5.25 includes the contribution discussed in Section 5.3.3 for both OWs. Taking into account the coefficients shown in Eqs. (5.16, 5.18), the noise contribution to the differential acceleration will be given by:

$$S^{1/2}_{\rm force,OW1}(f) = c_{\rm long,OW1} S^{1/2}_{TS_{\rm OW1}}(f), \tag{5.26}$$

$$S^{1/2}_{\rm force,OW1}(f) = c_{\rm long,OW2} S^{1/2}_{TS_{\rm OW2}}(f), \tag{5.27}$$

where $S^{1/2}_{TS_{\rm OW1}}(f)$ and $S^{1/2}_{TS_{\rm OW2}}(f)$ are the ASD for the average temperature of the temperatures measured with the three thermistors on the OW1 and

the OW2, respectively. These contributions are real forces on the TMs and, as we commented in Section 5.3.3, pressure gradients that fluctuate with temperature produced by outgasssing in the vacuum enclosures could explain these forces. We can see in Figure 5.25 that these contributions are very relevant, especially at lower frequencies. At 10^{-5} Hz, we can see that the lines reach a value of $10^{-14}\,\mathrm{m\,s^{-2}/\sqrt{Hz}}$, only a factor 5 smaller than the complete differential acceleration noise.

Finally, since at frequencies $\sim 10^{-5}$ Hz there is a clear correlation between temperatures and $\omega_2^2 \cdot (x_{\mathrm{GRS2}} - x_{\mathrm{GRS1}} - o_{12})$, which manifests motion between the GRSs and the OB, we have included this contribution. As discussed in Appendix D, we can express that stiffness as a function of an effective temperature, T_{eff}, as follows —see Eq. (5.1):

$$\frac{d\Delta g_0}{dT_{\mathrm{eff}}} = -\omega_2^2 \frac{d(x_{\mathrm{GRS2}} - x_{\mathrm{GRS1}} - o_{12})}{dT_{\mathrm{eff}}} = -k. \tag{5.28}$$

Thus, we can consider:

$$\omega_2^2 \cdot (x_{\mathrm{GRS2}} - x_{\mathrm{GRS1}} - o_{12}) = \omega_2^2 k T_{\mathrm{eff}}. \tag{5.29}$$

In Appendix D we have concluded that this T_{eff} seems to be the temperature at the interface between the lateral slab and the GRS vacuum chambers. However, for a noise run as the considered one here, the LTP temperature was roughly uniform, so we can take for example the average temperature of both OWs. Therefore, taking into account Eq. (5.29) , the noise contribution to this stiffness term will be given by:

$$S^{1/2}_{\mathrm{stiffness}}(f) = \omega_2^2 k S^{1/2}_{T_{\mathrm{eff}}}(f), \tag{5.30}$$

where $k \simeq 1.3\,\mu$m/K —see Table D.1— and $\omega_2^2 = (-4.19 \pm 0.04) \cdot 10^{-7}\,\mathrm{s^{-2}}$ (the stiffness term as estimated by dedicated experiments [23]).

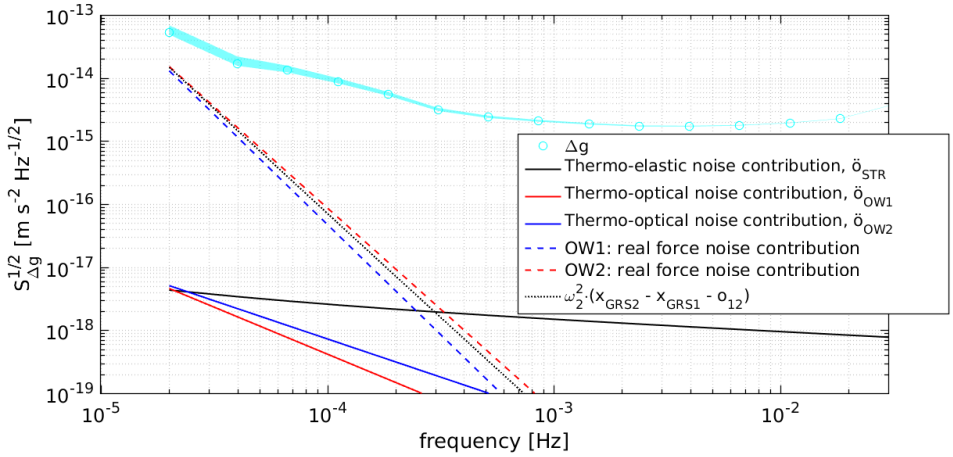

Figure 5.25: Thermo-elatic and thermo-optical noise contributions (continuous lines) coming from the OWs and the struts compared to the complete Δg noise for a segment of noise measured during February 14th-27th, 2017. To compute the spectrum, it has been used segments of 200000 s and applied a Blackman-Harris window, as in Figure 2.15. Also, we can see the contributions coming from both OWs (dashed line) that, unlike the other two ones, produce real forces on the TMs. To end, the black dotted line represents the stifness term $(\omega_2^2 \cdot (x_{\mathrm{GRS2}} - x_{\mathrm{GRS1}} - o_{12}))$ contribution that is plotted taking into account Eq. (5.30).

Chapter 6

Conclusions

In this thesis, we have focussed on temperature studies onboard the LPF mission. Specifically, we have analysed the thermal evolution during all the mission, and the experiments carried out in flight in order to estimate the residual differential acceleration contribution that comes from thermo-optical and thermo-elastic effects.

As we have shown in Chapter 4, in terms of thermal stability, the thermal sensors have reached what was proposed as a requirement in terms of amplitude spectral noise in the temperature measurement, 10 μK/$\sqrt{\text{Hz}}$ in the LPF band, 1 mHz $<$ f $<$ 30 mHz, showing only a slight deviation in the lowest frequency bin. Indeed, from 0.2 mHz to 2 mHz the temperature spectra are dominated by read-out noise arising from non-linearities in the temperature diagnostics ADC. There are methods to avoid this kind of issues, and thanks to the precise characterization made in flight, we can improve the design overcoming this read-out noise contribution for the future LISA temperature diagnostics subsystem. The low-frequency band below the 100 μHz is dominated by temperature fluctuations. We have determined a noise level of $50 - 100$ mK/$\sqrt{\text{Hz}}$ in the lowest bins of the LISA frequency band, $10 - 30$ μHz, for those locations in the inner core of the experiment. This noise level was maintained during the different science runs throughout

the mission, which provides an important insight into the degree of stationarity of the thermal fluctuations in the very low-frequency domain during flight operations.

We have also seen that LPF achieved residual acceleration noise levels of $(1.74 \pm 0.05)\,\mathrm{fm\,s^{-2}/\sqrt{Hz}}$ above 2 mHz, which is a factor 15 lower than the LPF requirement. A lot of sources such as magnetic fluctuations, laser frequency noise, charges on the TMs or temperature fluctuations contributed to this acceleration noise. In two different ways the temperature modified the relative acceleration, either producing real forces on the TMs when the thermal disturbances were located around them or changing the path-length of the optical read-out when the thermal disturbances were located in critical parts such as the OWs or the struts. In Chapter 5 we have shown the experiments carried out to analyse and estimate the second kind of thermal effects. Through thermal signals injected using the heaters located on the OWs and the struts, we produced temperature fluctuations at those locations which in turn produced thermo-optical distortions for the case of the OWs and thermo-elastic distortions for the case of the struts. We have used two models that gave us an estimation for both effects in term of the differential acceleration noise: roughly $10^{-18}\,\mathrm{m\,s^{-2}/\sqrt{Hz}}$ for the thermo-optical effects, and roughly $3 \cdot 10^{-18}\,\mathrm{m\,s^{-2}/\sqrt{Hz}}$ for the thermo-elastic effects at 0.05 mHz.

Furthermore, when the heaters on the OWs and the struts were switched on/off, it was observed that they produced a magnetic force on the TMs as a consequence of eddy currents induced on them. This effect has a short timescale but it has to be taken into account for the future LISA observatory, especially now, when we are developing the thermal diagnostics subsystem that will go onboard the LISA spacecrafts. On the other hand, the injections made with the heaters on the OWs, specially the injections at low frequencies, also produced real forces on the TMs by radiation pressure or outgassing effects, which is currently being studied in parallel with the

analysis of the thermal experiments in the EHs. Using a model that shows the relationship between the average temperature measured by the thermistors of each OW and the differential acceleration produced when there are thermal fluctuation on the windows, we have determined a contribution of $10^{-14}\,\mathrm{m\,s^{-2}}/\sqrt{\mathrm{Hz}}$ at 10^{-5} Hz for each OW. It is only a factor 5 smaller than the complete differential acceleration noise.

All these analyses and results can be transferred to the LISA mission:

- The thermal stability achieved with the thermistors, 10 $\mu\mathrm{K}/\sqrt{\mathrm{Hz}}$ in the LPF band, $1\,\mathrm{mHz} < \mathrm{f} < 30\,\mathrm{mHz}$, is the basis for the development of the future LISA thermistors whose stability requirement is an order of magnitude less, 1 $\mu\mathrm{K}/\sqrt{\mathrm{Hz}}$, in the same band.

- The characterization made in the low-frequency band for the temperature measured in the different locations will provide a significant limit to the instrument's performance because at those frequencies the temperature plays a crucial role.

- The thermal transfer functions estimated between locations when in some of them we injected thermal stimuli will be keys in order to know how the temperature is attenuated for the different components in LISA. It is especially interesting to see that there is an attenuation factor better than 10^{-2} for fluctuations with frequencies above 1 mHz between the thermal shield and the main scientific instrument (LTP). Although the spacecrafts of LISA will be different from LPF, these studies will help to understand how the temperature will change between the locations.

- The thermo-optical contribution estimated through the experiment carried out on the OWs will be the same in LISA because the structure of the vacuum chambers will be the same as in LPF. However, the thermo-elastic contribution estimated with the experiments carried out on the struts could be different because the support between the

main scientific instrument and the thermal shield will not be the same, although, as we stated in the previous point, it will allow us to perform good estimations about this kind of contributions.

Appendix A

Low-frequency temperature power-law fits

The ASD has been computed by means of the Welch averaged periodogram. We use segments of 400000 s and apply a Blackman-Harris window to prevent spectral leakage. After subtracting the lowest four frequency bins, we perform a power-law fit to the (remaining) four lowest frequency bins. The expression used for the fit is given by:

$$S^{1/2}(f) = b(2\pi f)^k, \tag{A.1}$$

where $S^{1/2}(f)$ is the ASD, and b and k are the parameters of the fit. In the locations where there is more than one sensor we use an average of sensors when considering the power-law fit. These are the EHs (EH1 and EH2) with four sensors in each of them; the OWs (OW1 and OW2) with three sensors in each; and the OB with four sensors, one at each corner. The six remaining sensors (TS17-TS22) correspond to sensors attached to different struts. Only six out of the eight struts had a pair heater/sensor attached.

In Table A.1 we can see the results of the fits for each of the noise runs during the LTP operations phase. These were periods where the instrument

Location	Parameters	Run #1	Run #2	Run #3	Run #4	Run #5	Run #6	Run #7
EH1	k	-3.67 ± 0.03	-3.71 ± 0.02	-3.46 ± 0.05	-3.75 ± 0.02	-3.60 ± 0.04	-3.89 ± 0.05	-3.47 ± 0.06
	b	$(9 \pm 3)\cdot10^{-17}$	$(9 \pm 2)\cdot10^{-17}$	$(5 \pm 3)\cdot10^{-16}$	$(4.4 \pm 0.7)\cdot10^{-17}$	$(2.0 \pm 0.8)\cdot10^{-16}$	$(1.2 \pm 0.5)\cdot10^{-17}$	$(5 \pm 3)\cdot10^{-16}$
EH2	k	-3.75 ± 0.05	-3.79 ± 0.03	-3.56 ± 0.06	-3.44 ± 0.03	-3.52 ± 0.04	-3.83 ± 0.08	-3.45 ± 0.02
	b	$(6 \pm 3)\cdot10^{-17}$	$(5 \pm 1)\cdot10^{-17}$	$(3 \pm 2)\cdot10^{-16}$	$(1.2 \pm 0.4)\cdot10^{-15}$	$(4 \pm 1)\cdot10^{-16}$	$(2 \pm 1)\cdot10^{-17}$	$(6 \pm 1)\cdot10^{-16}$
OB	k	-3.45 ± 0.09	-3.49 ± 0.05	-3.49 ± 0.05	-3.40 ± 0.04	-3.35 ± 0.05	-3.66 ± 0.06	-3.25 ± 0.06
	b	$9 \pm 8)\cdot10^{-16}$	$(1.0 \pm 0.5)\cdot10^{-15}$	$(9 \pm 5)\cdot10^{-16}$	$(1.9 \pm 0.8)\cdot10^{-15}$	$(2 \pm 1)\cdot10^{-15}$	$(1.3 \pm 0.7)\cdot10^{-16}$	$(5 \pm 3)\cdot10^{-15}$
OW1	k	-3.38 ± 0.04	-3.43 ± 0.03	-3.31 ± 0.07	-3.47 ± 0.03	-3.49 ± 0.04	-3.75 ± 0.07	-3.34 ± 0.04
	b	$(1.6 \pm 0.6)\cdot10^{-15}$	$(1.4 \pm 0.34)\cdot10^{-15}$	$(3 \pm 2)\cdot10^{-15}$	$(8 \pm 2)\cdot10^{-16}$	$(6 \pm 3)\cdot10^{-16}$	$(5 \pm 3)\cdot10^{-17}$	$(1.7 \pm 0.6)\cdot10^{-15}$
OW2	k	-3.70 ± 0.08	-3.50 ± 0.05	-3.34 ± 0.04	-3.20 ± 0.03	-3.21 ± 0.09	-3.80 ± 0.07	-3.29 ± 0.04
	b	$(1.0 \pm 0.7)\cdot10^{-16}$	$(8 \pm 4)\cdot10^{-16}$	$(3 \pm 1)\cdot10^{-15}$	$(1.2 \pm 0.4)\cdot10^{-14}$	$(9 \pm 7)\cdot10^{-15}$	$(3 \pm 2)\cdot10^{-17}$	$(3 \pm 1)\cdot10^{-15}$
TS17	k	-2.74 ± 0.07	-2.78 ± 0.04	-2.65 ± 0.05	-2.84 ± 0.03	-2.44 ± 0.06	-3.03 ± 0.09	-2.56 ± 0.06
	b	$(9 \pm 6)\cdot10^{-13}$	$(9 \pm 4)\cdot10^{-13}$	$(2 \pm 1)\cdot10^{-12}$	$(5 \pm 2)\cdot10^{-13}$	$(2 \pm 1)\cdot10^{-11}$	$(6 \pm 5)\cdot10^{-14}$	$(3 \pm 2)\cdot10^{-12}$
TS18	k	-2.73 ± 0.09	-2.81 ± 0.04	-2.73 ± 0.07	-2.85 ± 0.05	-2.54 ± 0.08	-2.92 ± 0.08	-2.42 ± 0.09
	b	$(1.0 \pm 0.9)\cdot10^{-12}$	$(7 \pm 3)\cdot10^{-13}$	$(1.1 \pm 0.8)\cdot10^{-12}$	$(5 \pm 2)\cdot10^{-13}$	$(7 \pm 2)\cdot10^{-12}$	$(2 \pm 1)\cdot10^{-13}$	$(2 \pm 1)\cdot10^{-11}$
TS19	k	-2.70 ± 0.07	-2.83 ± 0.05	-2.75 ± 0.06	-2.76 ± 0.07	-2.18 ± 0.06	-3.10 ± 0.08	-2.52 ± 0.08
	b	$(2 \pm 1)\cdot10^{-12}$	$(7 \pm 3)\cdot10^{-13}$	$(1.1 \pm 0.6)\cdot10^{-12}$	$(1.3 \pm 0.9)\cdot10^{-12}$	$(3 \pm 2)\cdot10^{-10}$	$(4 \pm 3)\cdot10^{-14}$	$(7 \pm 5)\cdot10^{-12}$
TS20	k	-2.83 ± 0.08	-2.98 ± 0.06	-2.88 ± 0.05	-2.89 ± 0.06	-2.53 ± 0.05	-2.93 ± 0.06	-2.47 ± 0.06
	b	$(4 \pm 3)\cdot10^{-13}$	$(1.3 \pm 0.7)\cdot10^{-13}$	$(3 \pm 1)\cdot10^{-13}$	$(3 \pm 2)\cdot10^{-13}$	$(7 \pm 4)\cdot10^{-12}$	$(2 \pm 1)\cdot10^{-13}$	$(9 \pm 5)\cdot10^{-12}$
TS21	k	-2.82 ± 0.07	-2.93 ± 0.02	-2.77 ± 0.06	-2.96 ± 0.02	-2.64 ± 0.05	-2.94 ± 0.05	-2.62 ± 0.07
	b	$(4 \pm 3)\cdot10^{-13}$	$(2.1 \pm 0.4)\cdot10^{-13}$	$(7 \pm 4)\cdot10^{-13}$	$(1.5 \pm 0.3)\cdot10^{-13}$	$(2 \pm 1)\cdot10^{-12}$	$(1.7 \pm 0.7)\cdot10^{-13}$	$(2 \pm 1)\cdot10^{-12}$
TS22	k	-2.82 ± 0.07	-2.94 ± 0.04	-2.80 ± 0.04	-2.88 ± 0.05	-2.50 ± 0.05	-2.87 ± 0.06	-2.55 ± 0.08
	b	$(4 \pm 3)\cdot10^{-13}$	$(1.9 \pm 0.7)\cdot10^{-13}$	$(5 \pm 2)\cdot10^{-13}$	$(3 \pm 2)\cdot10^{-13}$	$(1.0 \pm 0.4)\cdot10^{-11}$	$(4 \pm 2)\cdot10^{-13}$	$(4 \pm 3)\cdot10^{-12}$

Table A.1: Parameters for the power-law fit of the thermal fluctuations ASD at low frequencies. The model is given in Eq. (A.1) and the different runs are described in the text.

was configured in its optimal sensitivity configuration and left unperturbed during days and even weeks in some cases. The periods where these runs took place are listed below.

- Run #1 → from March 20th to March 26th (2016)
- Run #2 → from April 3rd to April 16th (2016)
- Run #3 → from November 17th to November 26th (2016)
- Run #4 → from December 26th (2016) to January 13th (2017)
- Run #5 → from February 14th to February 27th (2017)
- Run #6 → from May 29th to June 5th (2017)
- Run #7 → from June 8th to June 17th (2017)

The results of the power-law fits in Table A.1 support conclusions from the ones previously showed in Figure 4.4, that is, the time evolution for the amplitude spectra of thermal fluctuations in the $10 - 30\,\mu$Hz frequency range for the same noise runs.

Appendix B

Thermal transfer functions

The thermal transfer function between an origin location A and a final location B at a given frequency f is experimentally computed as

$$H_{A\to B}(f) = \frac{\widetilde{T}_B(f)}{\widetilde{T}_A(f)}, \tag{B.1}$$

where $\widetilde{T}_A(f)$ and $\widetilde{T}_B(f)$ are the Discrete Fourier Transform (DFT) of the temperatures at the location A and B at a given frequency f. Transfer functions are thus only computed between locations linked with pairs of sensors. In order to be representative of the heat flow between locations, these are just estimated when a heat input is active at the origin location, in which case we can make use of the temperature sensor close to the heater as representative of the heat injection. As previously discussed, the transfer functions from the outside the thermal shield to the inside are derived using the characterisation provided by the *bang-bang* controller during the commissioning. This was a homogeneous temperature modulation of all the spacecraft from where we can extract thermal transfer functions from a temperature sensor outside the thermal shield to its closest counterpart inside, typically attached to a strut.

Once we have obtained the points that experimentally define the transfer

function, we can fit them to a continuous model given by:

$$H_{A\to B}(s) = \frac{r_1}{s - p_1} + \frac{r_2}{s - p_2}, \tag{B.2}$$

where $H_{A\to B}(s)$ is the Laplace transform of the differential equation that describes the heat flow between points A and B. In this case, a second order transfer function model described by residuals, r_1 and r_2, and poles, p_1 and p_2. This expression corresponds to a differential equation that can be understood as an approximation to second order of the heat flow equation that describes the heat flow from the origin to the final location. The fit is done using the vector fit algorithm [45] implemented in the LTPDA toolbox [52]. In Table B.1 we show the values obtained for these fits.

Origin → End	r_1	p_1	r_2	p_2	Corner frequency (μHz)	DC gain
LCA4 → TS17	$-8 \cdot 10^{-5}$	$-9 \cdot 10^{-4}$	$9 \cdot 10^{-5}$	$-2 \cdot 10^{-4}$	36	$3.6 \cdot 10^{-1}$
LCA5 → TS18	$-7 \cdot 10^{-5}$	$-4 \cdot 10^{-3}$	$8 \cdot 10^{-5}$	$-1 \cdot 10^{-4}$	54	$7.8 \cdot 10^{-1}$
LCA2 → TS22	$-3 \cdot 10^{-4}$	$-3 \cdot 10^{-1}$	$6 \cdot 10^{-5}$	$-9 \cdot 10^{-4}$	140	$6.6 \cdot 10^{-2}$
TS17 → TS10	$-2 \cdot 10^{-7}$	$-2 \cdot 10^{-3}$	$2 \cdot 10^{-7}$	$-1 \cdot 10^{-3}$	122	$1.0 \cdot 10^{-4}$
TS17 → TS11	$-2 \cdot 10^{-7}$	$-4 \cdot 10^{-3}$	$2 \cdot 10^{-7}$	$-5 \cdot 10^{-4}$	350	$1.2 \cdot 10^{-4}$
TS17 → TS1	$1 \cdot 10^{-6}$	$-9 \cdot 10^{-4}$	$-1 \cdot 10^{-6}$	$-1 \cdot 10^{-4}$	26	$8.9 \cdot 10^{-3}$
TS18 → TS16	$-4 \cdot 10^{-7}$	$-2 \cdot 10^{-2}$	$3 \cdot 10^{-7}$	$-3 \cdot 10^{-3}$	1413	$9.6 \cdot 10^{-5}$
TS18 → TS10	$-1 \cdot 10^{-7}$	$-6 \cdot 10^{-2}$	$1 \cdot 10^{-7}$	$-1 \cdot 10^{-3}$	666	$9.8 \cdot 10^{-4}$
TS18 → TS8	$-7 \cdot 10^{-7}$	$-4 \cdot 10^{-3}$	$5 \cdot 10^{-7}$	$-5 \cdot 10^{-4}$	122	$8.3 \cdot 10^{-4}$
TS9 → TS14	$-9 \cdot 10^{-6}$	$-1 \cdot 10^{-3}$	$9 \cdot 10^{-6}$	$-2 \cdot 10^{-4}$	38	$3.6 \cdot 10^{-2}$
TS9 → TS3	$-1 \cdot 10^{-5}$	$-6 \cdot 10^{-4}$	$1 \cdot 10^{-5}$	$-4 \cdot 10^{-5}$	13	$2.3 \cdot 10^{-1}$
TS10 → TS16	$-3 \cdot 10^{-6}$	$-8 \cdot 10^{-4}$	$5 \cdot 10^{-6}$	$-2 \cdot 10^{-4}$	34	$2.1 \cdot 10^{-2}$
TS10 → TS8	$3 \cdot 10^{-4}$	-2	$4 \cdot 10^{-6}$	$-4 \cdot 10^{-5}$	769	$1.0 \cdot 10^{-1}$
TS4 → TS14	$-1 \cdot 10^{-6}$	$-2 \cdot 10^{-3}$	$6 \cdot 10^{-7}$	$-1 \cdot 10^{-4}$	38	$5.5 \cdot 10^{-3}$
TS4 → TS11	$-3 \cdot 10^{-5}$	$-2 \cdot 10^{-3}$	$3 \cdot 10^{-5}$	$-2 \cdot 10^{-4}$	54	$1.4 \cdot 10^{-1}$
TS8 → TS16	$-7 \cdot 10^{-7}$	$-1 \cdot 10^{-3}$	$5 \cdot 10^{-7}$	$-7 \cdot 10^{-5}$	23	$6.4 \cdot 10^{-3}$
TS8 → TS12	$-2 \cdot 10^{-5}$	$-1 \cdot 10^{-3}$	$4 \cdot 10^{-5}$	$-9 \cdot 10^{-5}$	26	$4.2 \cdot 10^{-1}$

Table B.1: Thermal transfer functions parameters between different locations. The model is given in Eq. (B.2).

Appendix C

$\triangle g$ model when there are thermal fluctuations

The standard expression used to compute the differential acceleration between both TMs in the x-axis is derived in Section 2.3.1. However, in thermal fluctuation scenarios, it is necessary to introduce some corrections to that equation [35].

Considering the distances defined in Figure C.1, we have the following relationships with respect the local inertial frame (0):

$$\begin{aligned} x_{\mathrm{GRS1}} &= x_1 - x_{\mathrm{EH1}}(T) - x_{\mathrm{SC}}, \\ x_{\mathrm{GRS2}} &= x_2 - x_{\mathrm{EH2}}(T) - x_{\mathrm{SC}}, \\ o_1 &= x_1 - x_{\mathrm{SC}} + n_1 - \frac{1}{2}o_{\mathrm{OB}} - o_{\mathrm{OW1}} - \frac{1}{2}o_{\mathrm{STR}}, \\ o_{12} &= x_2 - x_1 + n_{12} + o_{\mathrm{OB}} + o_{\mathrm{OW1}} + o_{\mathrm{OW2}} + o_{\mathrm{STR}}, \end{aligned} \tag{C.1}$$

where n_{12} is the noise read-out of the interferometer o_{12}, n_1 is the noise read-out of the interferometer o_1, o_{OB} is the path-length variation introduced in the interferometric signal due to thermal fluctuations on the OB, o_{OW1} is the path-length variation introduced in the interferometric signal

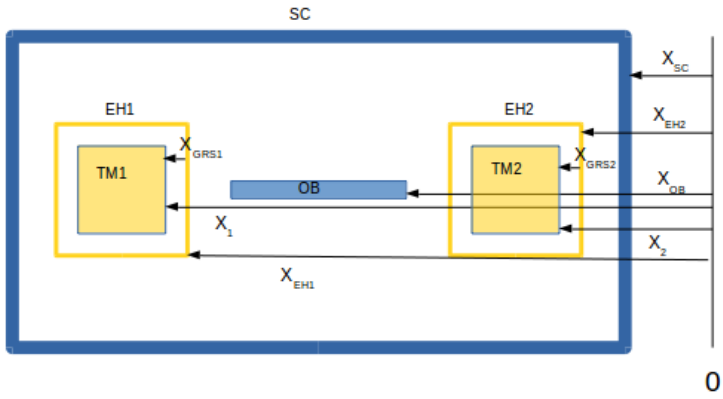

Figure C.1: Scheme that represents the different distances inside the LTP with respect to the inertial frame (0). Distance between the EH1 and the TM1, x_{GRS1}; distance between the inertial frame and the EH1, x_{EH1}; distance between the inertial frame and the TM1, x_1; distance between the EH2 and the TM2, x_{GRS2}; distance between the inertial frame and the EH2, x_{EH2}; distance between the inertial frame and the TM2, x_2; distance between the inertial frame and the spacecraft, x_{SC}; distance between the inertial frame and the OB, x_{OB}.

due to thermal fluctuations on the OW1, o_{OW2} is the path-length variation introduced in the interferometric signal due to thermal fluctuations on the OW2, and, finally, o_{STR} is the path-length variation introduced in the interferometric signal due to thermal fluctuations on the struts that perturb the OB which in turn changes the path length of the interferometric signal. Since during the mission the experiments were carried out using the heaters on the struts (there were no heaters on the OB), there are two terms to distinguish the perturbations on the OB from the ones coming from thermal fluctuations on the struts —see Section 5.4.

The equations of motion for the TMs are given by:

$$\ddot{x}_1 = \frac{F_1}{m_{\mathrm{TM}}} - \omega_1^2 \cdot x_{\mathrm{GRS1}},$$

$$\ddot{x}_2 = \frac{F_2}{m_{\mathrm{TM}}} - \omega_2^2 \cdot x_{\mathrm{GRS2}} + \frac{F_{\mathrm{ES}}}{m_{\mathrm{TM}}}, \tag{C.2}$$

where ω_1^2 and ω_2^2 are the total stiffness per unit mass between each TM and the spacecraft, F_1 and F_2 the forces on TM1 and TM2 respectively, F_{ES} contains all the forces acting on the spacecraft, and m_{TM} the TM mass.

Finally, the expression of Δg taking into account the corrections due to thermal fluctuations is given by:

$$\begin{aligned}
\Delta g_{\mathrm{te}} = \ddot{o}_{12}(t) - \frac{F_{\mathrm{ES}}(t)}{m_{\mathrm{TM}}} + \Delta\omega_{12}^2 \cdot o_1(t) + \omega_2^2 \cdot o_{12}(t) - \Delta g(t)_{\mathrm{IFO}} \\
-\ddot{o}_{\mathrm{OW1}} - \ddot{o}_{\mathrm{OW2}} - \ddot{o}_{\mathrm{STR}} - \ddot{o}_{\mathrm{OB}} \\
+\omega_2^2 \cdot (x_{\mathrm{GRS2}} - x_{\mathrm{GRS1}} - o_{12}) + \Delta\omega_{12}^2 \cdot (x_{\mathrm{GRS1}} - o_1) \\
= \Delta g_0 - \ddot{o}_{\mathrm{OW1}} - \ddot{o}_{\mathrm{OW2}} - \ddot{o}_{\mathrm{STR}} - \ddot{o}_{\mathrm{OB}} \\
+\omega_2^2 \cdot (x_{\mathrm{GRS2}} - x_{\mathrm{GRS1}} - o_{12}) + \Delta\omega_{12}^2 \cdot (x_{\mathrm{GRS1}} - o_1),
\end{aligned} \tag{C.3}$$

where Δg_0 is the standard definition of Δg —see Section 2.3.1. The terms

$\ddot{o}_{\mathrm{OW1}}$, $\ddot{o}_{\mathrm{OW2}}$, $\ddot{o}_{\mathrm{STR}}$, and $\ddot{o}_{\mathrm{OB}}$ are the path-length variations introduced in the residual acceleration when there are thermal fluctuations in those locations. The terms $\omega_2^2 \cdot (x_{\mathrm{GRS2}} - x_{\mathrm{GRS1}} - o_{12})$ and $\Delta\omega_{12}^2 \cdot (x_{\mathrm{GRS1}} - o_1)$ represent relative displacements between the GRSs and the OB, although the second term in negligible because $\Delta\omega_{12}^2 \ll \omega_2^2$. We can write Eq. (C.3) as:

$$\Delta g_0 = \Delta g_{\mathrm{te}} + \ddot{o}_{\mathrm{OW1}} + \ddot{o}_{\mathrm{OW2}} + \ddot{o}_{\mathrm{STR}} + \ddot{o}_{\mathrm{OB}}$$

$$-\omega_2^2 \cdot (x_{\mathrm{GRS2}} - x_{\mathrm{GRS1}} - o_{12}) - \Delta\omega_{12}^2 \cdot (x_{\mathrm{GRS1}} - o_1). \qquad \text{(C.4)}$$

Thus Δg_0 is the standard definition of Δg explained in Section 2.3.1 that includes the path-length variation introduced by $\ddot{o}_{\mathrm{OW1}}$, $\ddot{o}_{\mathrm{OW2}}$, $\ddot{o}_{\mathrm{STR}}$, and $\ddot{o}_{\mathrm{OB}}$, and the thermo-mechanical distortion between the GRSs and the OB expressed through the terms $\omega_2^2 \cdot (x_{\mathrm{GRS2}} - x_{\mathrm{GRS1}} - o_{12})$ and $\Delta\omega_{12}^2 \cdot (x_{\mathrm{GRS1}} - o_1)$. Hence, Δg_{te} is the Δg free of these effects.

Appendix D

Stiffness between the Gravitational Reference Sensors and the Optical Bench

At frequencies $\sim 10^{-5}$ Hz there is a clear correlation between temperatures and $\omega_2^2 \cdot (x_{\mathrm{GRS2}} - x_{\mathrm{GRS1}} - o_{12})$ —see Figure D.1. It manifests motion between the GRSs and the OB and, hence, the presence of a stiffness force.

If we consider that the effective temperature of the mechanism respon-

Run	EHs	OWs	OB	STRs
Run #1	1.0929 ± 0.0004	1.1100 ± 0.0003	1.1158 ± 0.0002	1.1602 ± 0.0002
Run #2	0.8756 ± 0.0007	0.9136 ± 0.0006	0.9296 ± 0.0005	0.9668 ± 0.0004
Run #3	0.243 ± 0.001	0.247 ± 0.001	0.2464 ± 0.0009	0.2423 ± 0.0009
Run #4	0.6910 ± 0.0004	0.7244 ± 0.0004	0.7452 ± 0.0004	0.7847 ± 0.0004
Run #5	1.2909 ± 0.0005	1.3199 ± 0.0005	1.3399 ± 0.0005	1.3753 ± 0.0005
Run #6	3.61 ± 0.03	5.15 ± 0.03	5.45 ± 0.02	5.85 ± 0.02
Run #7	0.764 ± 0.001	0.869 ± 0.001	0.928 ± 0.001	1.0541 ± 0.0009
Average	1.2 ± 0.4	1.5 ± 0.6	1.5 ± 0.7	1.6 ± 0.7

Table D.1: Coupling k (μm/K) between ($x_{\mathrm{GRS2}} - x_{\mathrm{GRS1}} - o_{12}$) and the average temperature at each location. The model is given by Eq. (D.3).

sible of this effect is $T_{\rm eff}$, we can write —see Eq. (C.4):

$$\frac{d\Delta g_0}{dT_{\rm eff}} = -\omega_2^2 \frac{d(x_{\rm GRS2} - x_{\rm GRS1} - o_{12})}{dT_{\rm eff}} = -k. \tag{D.1}$$

Thus, we can consider:

$$\omega_2^2 \cdot (x_{\rm GRS2} - x_{\rm GRS1} - o_{12}) = \omega_2^2 k T_{\rm eff}. \tag{D.2}$$

That is:

$$x_{\rm GRS2} - x_{\rm GRS1} - o_{12} = k T_{\rm eff}, \tag{D.3}$$

Eq. (D.3) allows us to make a fit for several noise runs (where the LTP temperature was roughly uniform) considering the average temperature for each location, namely, the EHs, the OB, the OWs, and the struts —see Figure D.1:

$$T_{\rm EHs} = \frac{TS1 + TS2 + TS3 + TS4 + TS5 + TS6 + TS7 + TS8}{8}, \tag{D.4}$$

$$T_{\rm OB} = \frac{TS13 + TS14 + TS15 + TS16}{4}, \tag{D.5}$$

$$T_{\rm OWs} = \frac{TS9 + TS11 + TS24 + TS10 + TS12 + TS23}{6}, \tag{D.6}$$

$$T_{\rm STRs} = \frac{TS17 + TS18 + TS19 + TS20 + TS21 + TS22}{6}. \tag{D.7}$$

Taking into account the noise runs considered in Appendix A, we get the values for the parameter k shown in Table D.1. We can see that all the values are around 1 μm/K.

As discussed in Section 5.3.3, the injections at 0.1 mHz with the heaters on the OWs produced a $\omega_2^2 \cdot (x_{\rm GRS2} - x_{\rm GRS1} - o_{12})$ contribution, being the coupling of this term with the average temperature of the sensors located on the OW that was being stimulated with the heaters of ≈ 0.04 μm/K —see

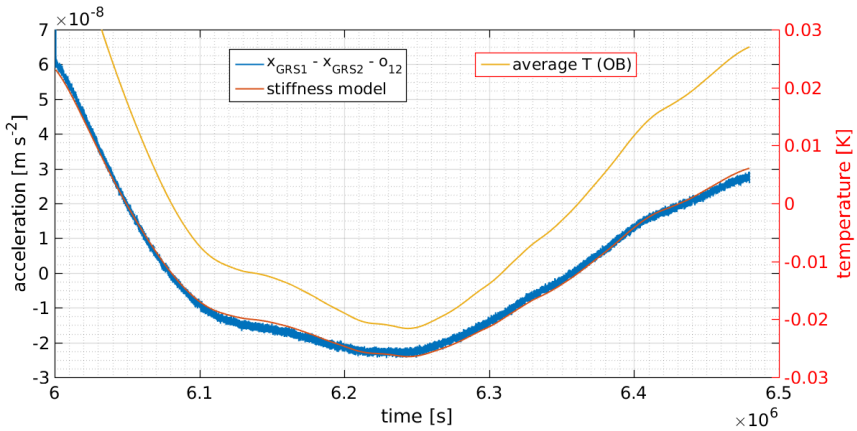

Figure D.1: This plot shows $x_{\mathrm{GRS2}} - x_{\mathrm{GRS1}} - o_{12}$, T_{OB} and the fit obtained by using Eq. (D.3). To ease the fit, we have made a detrend of order 1 to $x_{\mathrm{GRS2}} - x_{\mathrm{GRS1}} - o_{12}$ and T_{OB}.

Figure D.2—, smaller than the average coefficient k shown in Table D.1. If we consider the temperature measured by the closest thermistors on the OB the coupling is $\approx 4.5\,\mu$m/K, bigger than the average coefficient k shown in Table D.1. In addition, we observe in Figure D.2 that there is a delay between $\omega_2^2 \cdot (x_{\mathrm{GRS2}} - x_{\mathrm{GRS1}} - o_{12})$ and the temperature given by the sensors on the OB, which, together with the bigger coupling observed between these magnitudes, lead us to think that the heating of a part further than the OW but closer than the OB, for example the interface between the lateral slab and the GRS vacuum chambers, is the main responsible for producing the relative movement between the OB and the GRSs. Therefore, T_{eff} would be the temperature of this place.

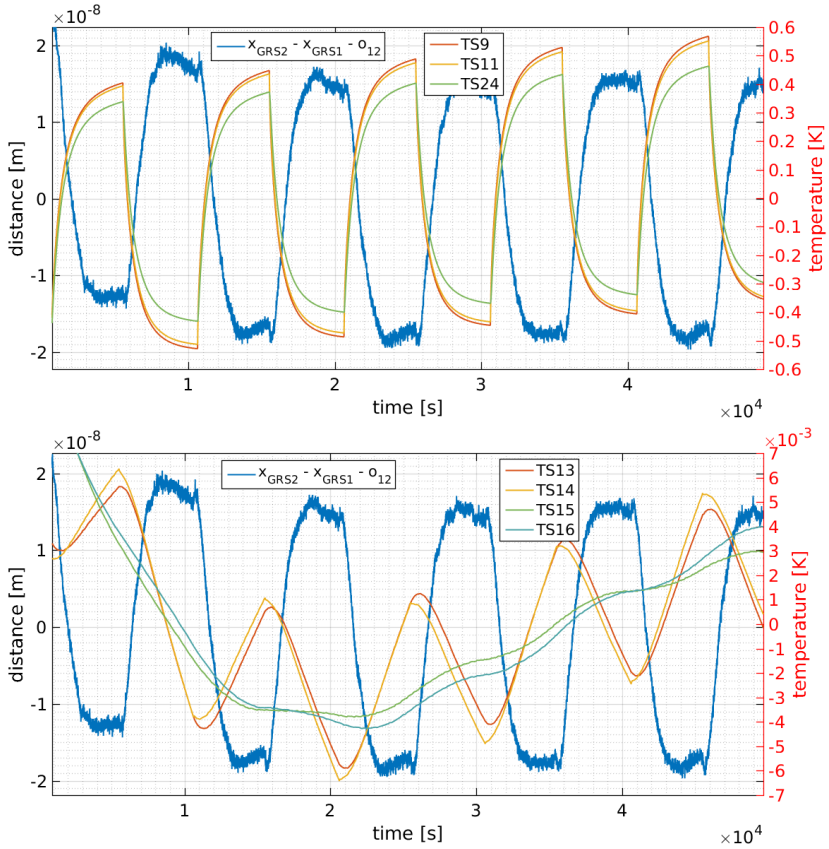

Figure D.2: This plot shows the $x_{\mathrm{GRS2}} - x_{\mathrm{GRS1}} - o_{12}$ signal and the temperatures measured by the thermal sensors on the OW1 (*top*) and the thermal sensors on the OB (*bottom*) when signals at 0.1 mHz were injected with the heaters on the OW1. We have made a detrend of order 1.

Appendix E

Glitches: the electromagnetic hypothesis

Through on-ground experiments, we have observed that when the heaters located on the OWs and struts are switched on/off, they produce a magnetic field like if the heaters were small coils. Taking into account that eddy currents can appear in the TMs [94], we can consider that when we switched on/off the heaters appeared currents in the TMs as a consequence of the magnetic flux variation in the TM surfaces (Lenz and Faraday's laws). It in turn produced a magnetic field which had the same direction but opposite sign that the magnetic field that produced the currents.

Therefore, as a first approximation, we are going to suppose that a heater acts as a dipole with magnetic moment $\vec{m}(t)$. Additionally, we will consider that an eddy current appears on the parallel face of the TM to the OW where a heater is injecting thermal stimuli in the same way as if the TM was a conductive ring as shown in Figure E.1. In that case, the induced azimuthal electric field will be given by [55]:

$$\vec{E} = -\frac{\partial}{\partial t}\left(\frac{\mu_0}{4\pi}\frac{\vec{m}\times\vec{r}}{r^3}\right) = -\frac{\mu_0}{4\pi}\frac{\dot{m}\rho}{(\rho^2+z^2)^{3/2}}u_\varphi, \tag{E.1}$$

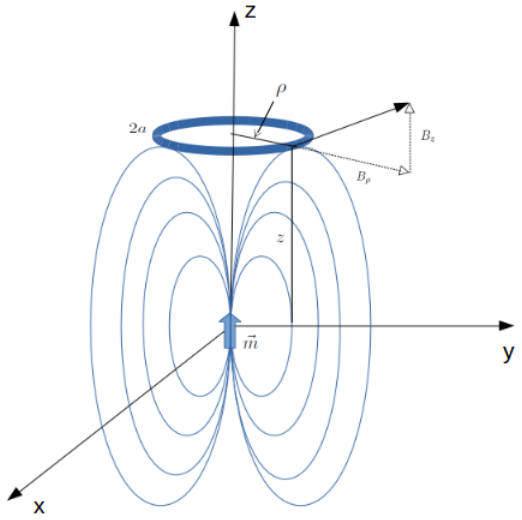

Figure E.1: Schematic where a heater is represented as a magnetic dipole $\vec{m}$ and the TM as a coductive ring whose thickness is $2a$.

where μ_0 is the magnetic permeability of vacuum, $\rho = 23\,mm$, and z is the distance between the ring (TM) and the dipole (heater). With this, the electromotive force will be [55]:

$$\varepsilon = \oint \vec{E} \cdot \vec{dl} = 2\pi\rho E_\varphi = -\frac{\mu_0}{2} \frac{\dot{m}\rho^2}{(\rho^2 + z^2)^{3/2}}. \tag{E.2}$$

Taking into account the self-inductance of the ring and Ohm's law, the phasor form of the induced current is as follows [55]:

$$\bar{I} = \frac{\bar{\varepsilon}}{R + i\omega L}, \tag{E.3}$$

where ω is the angular frequency, i is the complex unit, and R and L are the resistance of the ring and its self-inductance respectively. The equations

that provide us these parameters are [55]:

$$R = \frac{2\rho}{\sigma a^2}, \tag{E.4}$$

$$L \simeq \mu_0 \rho (ln\frac{8\rho}{a} - \frac{7}{4}), \tag{E.5}$$

being a the radius of the wire that in this case will be the penetration depth divided by 2:

$$a = \frac{1}{2}\sqrt{\frac{\sigma 2 t_{\mathrm{h}}}{\mu_0}}, \tag{E.6}$$

where $\sigma = 3 \cdot 10^{-7}\,\Omega\,m$ is the resistivity of the ring (TM) while $t_{\mathrm{h}} = 0.0094\,s$ is the RC-time constant of the heater. As $2a = 67\,mm$, bigger than the TM width, we can consider $2a = 46\,mm$, the TM width, obtaining the following values for the resistance and the self-inductance:

$$R \simeq 2.6 \cdot 10^{-5}\,\Omega, \tag{E.7}$$

$$L \simeq 9.5 \cdot 10^{-9}\,\mathrm{H}. \tag{E.8}$$

Once we have R and L, we can determine the induced intensity. The phasor form of the electromotive force that appears in Eq. (E.2) is:

$$\bar{\varepsilon} = -\frac{\mu_0}{2}\frac{\rho^2}{(\rho^2 + z^2)^{3/2}} s\bar{m}, \tag{E.9}$$

where $s = i\omega$ and $\bar{m}$ is the phasor form of the modulus of the magnetic moment. If a heater is like a small coil, its moment is the vector sum of the moments of individual turns. Considering that it has N turns and a vector area $\vec{S}$, we have:

$$\vec{m} = N I_{\mathrm{h}} \vec{S}, \tag{E.10}$$

being I_{h} the current intensity of the heater, which is given by the following equation at the time we turn on the heater (the intensity goes up):

$$I_{\mathrm{h}} = I_{\max}(1 - e^{-t/t_{\mathrm{h}}}), \tag{E.11}$$

with $I_{\max}$ the maximum intensity reached by the heater when we switch on it. When we turn off the heater, the equation for the intensity will be:

$$I_{\rm h} = I_{\max} e^{-t/t_{\rm h}}. \tag{E.12}$$

Therefore, the phasor form of the modulus of the magnetic moment when we switch on the heater will be given by:

$$\begin{aligned} \bar{m}(s) &= N \cdot S \cdot I_{\max} \cdot \int_0^\infty (1 - e^{-t/t_{\rm h}}) e^{-st} dt \\ &= N \cdot S \cdot I_{\max} \cdot (\frac{1}{s} - \frac{1}{\frac{1}{t_{\rm h}} + s}). \end{aligned} \tag{E.13}$$

This gives us the following expression for the induced intensity:

$$\begin{aligned} \bar{I} &= -\frac{\mu_0}{2} \frac{\rho^2}{(\rho^2 + z^2)^{3/2}} \frac{N \cdot S \cdot I_{\max}}{R} \cdot \frac{1}{1 + t_{\rm TM}} \cdot s(\frac{1}{s} - \frac{1}{\frac{1}{t_{\rm h}} + s}) \\ \Rightarrow I &= -\frac{\mu_0}{2} \frac{\rho^2}{(\rho^2 + z^2)^{3/2}} \frac{N \cdot S \cdot I_{\max}}{R \cdot (t_{\rm h} - t_{\rm TM})} \cdot \\ &\quad \cdot (e^{-t/t_{\rm h}} - e^{-t/t_{\rm TM}}), \end{aligned} \tag{E.14}$$

where $t_{\rm TM} = L/R$.

On the other side, the expression for the intensity when we switch off the heater —see Eq. (E.12)— will be:

$$\begin{aligned} I = -\frac{\mu_0}{2} \frac{\rho^2}{(\rho^2 + z^2)^{3/2}} \frac{N \cdot S \cdot I_{\max}}{R \cdot (t_{\rm TM}^2 - t_{\rm h} \cdot t_{\rm TM})} \cdot \\ \cdot (t_{\rm TM} \cdot e^{-t/t_{\rm h}} - t_{\rm h}\ e^{-t/t_{\rm TM}}). \end{aligned} \tag{E.15}$$

Finally, by means of Ampre's law, $\vec{F} = I \oint \vec{dl} \times \vec{B}$, we can obtain the value of the perpendicular force to the parallel face of the TM to the OW,

which will only depend on the radial component of the magnetic field [55]:

$$F = -2\pi\rho I B_\rho, \tag{E.16}$$

being B_ρ the radial component of the magnetic induction of a dipole. When we switch on the heater the equation for this component will be:

$$B_\rho = \frac{3\mu_0}{4\pi}\frac{\rho z}{(\rho^2+z^2)^{5/2}} N \cdot S \cdot I_{\max} \cdot (1 - e^{-t/t_{\mathrm{h}}}). \tag{E.17}$$

While when we switch off the heater:

$$B_\rho = \frac{3\mu_0}{4\pi}\frac{\rho z}{(\rho^2+z^2)^{5/2}} N \cdot S \cdot I_{\max} \cdot e^{-t/t_{\mathrm{h}}}. \tag{E.18}$$

Additionally, we can write the previous equations in terms of voltage or power considering:

$$I = \frac{V}{R}, \tag{E.19}$$

$$P = \frac{V^2}{R}. \tag{E.20}$$

Hence, taking into account Eqs. (E.16, E.14, E.17), when we turn on the heater the equation of the force in terms of power injected with the heaters will have the following form:

$$F = \frac{3\mu_0^2}{4}\frac{\rho^4 z}{(\rho^2+z^2)^4}\frac{(N\cdot S)^2}{R\cdot(t_{\mathrm{h}} - t_{\mathrm{TM}})} \cdot \frac{1}{R_{\mathrm{h}}} \cdot$$

$$\cdot(1 - e^{-t/t_{\mathrm{h}}}) \cdot (e^{-t/t_{\mathrm{h}}} - e^{-t/t_{\mathrm{TM}}}) \cdot P_{\max}, \tag{E.21}$$

where $R_{\mathrm{h}} = 45\,\Omega$ is the heater resistance and $P_{\max}$ is the maximum power reached by the heater during the injection. Taking into account Eqs (E.16, E.15, E.18) for the turn-off instant, the equation will be:

$$F = \frac{3\mu_0^2}{4}\frac{\rho^4 z}{(\rho^2+z^2)^4}\frac{(N\cdot S)^2}{R\cdot(t_{\rm TM}^2 - t_{\rm h}\cdot t_{\rm TM})}\cdot\frac{1}{R_{\rm h}}\cdot$$

$$\cdot e^{-t/t_{\rm h}}\cdot(t_{\rm TM}\cdot e^{-t/t_{\rm h}} - t_{\rm h}\, e^{-t/t_{\rm TM}})\cdot P_{\rm max}. \tag{E.22}$$

On the other hand, in Eq. (E.16) we can introduce the interplanetary magnetic field B_0 (210 nT) as follows:

$$F = -2\pi\rho I(B_\rho + B_0). \tag{E.23}$$

Taking into account that for all the injections carried out during the OWs and struts experiments $B_0 \simeq 10^2\cdot B_\rho$, we can write:

$$F = -2\pi\rho I\cdot B_\rho(\frac{B_0}{B_\rho}+1) \simeq -10^2\cdot 2\pi\rho I B_\rho. \tag{E.24}$$

With this, dividing the force by the TM mass, $m_{\rm TM}$, we will obtain the differential acceleration due to this magnetic effect . For the turn-on instant:

$$\Delta g_{\rm induc} = \frac{10^2\cdot 3\mu_0^2}{4}\frac{\rho^4 z}{(\rho^2+z^2)^4}\frac{(N\cdot S)^2}{R\cdot(t_{\rm h}-t_{\rm TM})}\cdot\frac{1}{R_{\rm h}\cdot m_{\rm TM}}\cdot$$

$$\cdot(1-e^{-t/t_{\rm h}})\cdot(e^{-t/t_{\rm h}} - e^{-t/t_{\rm TM}})\cdot P_{\rm max}. \tag{E.25}$$

And for the turn-off instant:

$$\Delta g_{\rm induc} = \frac{10^2\cdot 3\mu_0^2}{4}\frac{\rho^4 z}{(\rho^2+z^2)^4}\frac{(N\cdot S)^2}{R\cdot(t_{\rm TM}^2 - t_{\rm h}\cdot t_{\rm TM})}\cdot$$

$$\cdot\frac{1}{R_{\rm h}\cdot m_{\rm TM}}\cdot e^{-t/t_{\rm h}}\cdot(t_{\rm TM}\cdot e^{-t/t_{\rm h}} - t_{\rm h}\, e^{-t/t_{\rm TM}})\cdot P_{\rm max}. \tag{E.26}$$

In the analysis of the experiments carried out injecting thermal stimuli with the heaters on the OWs and the struts, we are only representing the

height of the rise reached for the glitches of Δg when we switch on/off the heaters as a function of $P_{\max}$. So, we are going to use only Eq. (E.25) to compare with the experimental results.

We have estimated the value of the product $N \cdot S$ to a distance of $z \simeq 5$ cm, which is the distance between the OW and the closest face of the TM, by means of on-ground experiments, getting the following reduced expression:

$$\Delta g_{\text{induc}} = c_{\text{P}} \cdot P_{\max} \simeq 2.5 \cdot 10^{-12} \cdot P_{\max}. \tag{E.27}$$

To end, taking into account a distance between the heaters on the struts and their closest TM of $z \simeq 13$ cm, we have experimentally determined in the laboratory a value of $N \cdot S$ which provides us the following reduced expression:

$$\Delta g_{\text{induc}} = c_{\text{P}} \cdot P_{\max} \simeq 2 \cdot 10^{-13} \cdot P_{\max}. \tag{E.28}$$

Appendix F

Equivalent resistive model for the struts

In Figure F.1 we show that we can model a strut as a circuit whose elements will be a thermal resistance and a thermal capacitance for each material [46]. Taking into account that one strut is composed of three parts, namely two Titanium end fittings and a central part of CFRP, we can represent it as a circuit with three different parts, each of them with a resistance and a capacitance. This equivalent resistive model allows to estimate which is the cut-off frequency of the low-pass temperature filter that represents each of the different parts. Since the thermistor was located in the center of the strut —see Figure 3.4— we can reduce the model to only half of the CFRP

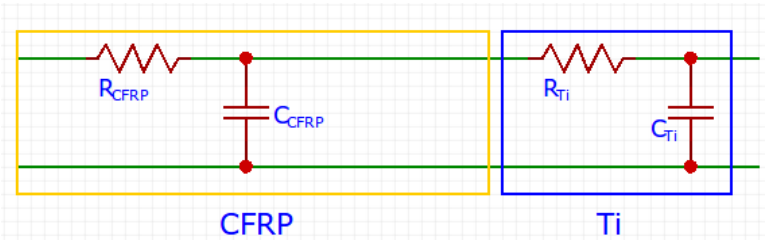

Figure F.1: Scheme of the equivalent resistive model for the struts.

Part	Thermal Resistance [K/W]	Thermal Capacitance [J/K]
CFRP	13	31.5
Titanium end fitting	7	30.5
Total	20	62

Table F.1: Thermal properties of the CFRP part and the Titanium end fitting.

part, and a Titanium end fitting, obtaining the model in Figure F.1. In Table F.1 we quote the values for the thermal resistance and the thermal capacitance for each of the parts considered [46].

Therefore, the cut-off frequency for the complete part of the strut shown in Figure F.1 is:

$$f_{\text{Total}} = \frac{1}{R_{\text{Total}} \cdot C_{\text{Total}}} = \frac{1}{20 \cdot 62} = 0.81\,\text{mHz}. \tag{F.1}$$

While the cut-off frequency considering only the CFRP part is:

$$f_{\text{CFRP}} = \frac{1}{R_{\text{CFRP}} \cdot C_{\text{CFRP}}} = \frac{1}{13 \cdot 31.5} = 2.4\,\text{mHz}. \tag{F.2}$$

Bibliography

[1] Abbott, B. P. et al. Observation of Gravitational Waves from a Binary Black Hole Merger. *Phys. Rev. Lett.*, 116:061102, Feb 2016. doi: 10.1103/PhysRevLett.116.061102. URL `https://link.aps.org/doi/10.1103/PhysRevLett.116.061102`.

[2] Abbott, B. P. et al. GW170817: Observation of Gravitational Waves from a Binary Neutron Star Inspiral. *Phys. Rev. Lett.*, 119:161101, Oct 2017. doi: 10.1103/PhysRevLett.119.161101. URL `https://link.aps.org/doi/10.1103/PhysRevLett.119.161101`.

[3] Abbott, B. P. et al. GWTC-1: A Gravitational-Wave Transient Catalog of Compact Binary Mergers Observed by LIGO and Virgo during the First and Second Observing Runs. *arXiv:1811.12907 [astro-ph, physics:gr-qc]*, 2018. URL `http://arxiv.org/abs/1811.12907`.

[4] Abramovici, A. et al. LIGO: The Laser Interferometer Gravitational-Wave Observatory. *Science*, 256(5055):325–333, 1992. doi: 10.1126/science.256.5055.325. URL `http://www.sciencemag.org/content/256/5055/325.abstract`.

[5] Acernese, F. et al. Advanced Virgo: a second-generation interferometric gravitational wave detector. *Classical and Quantum Gravity*, 32(2):024001, dec 2014. doi: 10.1088/0264-9381/32/2/024001.

[6] Acernese, F. et al. The Advanced Virgo detector. *Journal of Physics: Conference Series*, 2015.

[7] Adam, R. et al. Planck 2015 results. I. Overview of products and scientific results. *A&A*, 594, Oct 2015. doi: https://doi.org/10.1051/0004-6361/201527101.

[8] Ade, P. A. R . et al. Joint Analysis of BICEP2/Keck Array and Planck Data. *Phys. Rev. Lett.*, 114:101301, Mar 2015. doi: 10.1103/PhysRevLett.114.101301. URL `https://link.aps.org/doi/10.1103/PhysRevLett.114.101301`.

[9] Aggarwal, K. et al. The NANOGrav 11-Year Data Set: Limits on Gravitational Waves from Individual Supermassive Black Hole Binaries. *arXiv:1812.11585*, 2018.

[10] Odylio Denys Aguiar. Past, present and future of the resonant-mass gravitational wave detectors. *Research in Astronomy and Astrophysics*, 2010.

[11] Aguilera, D. N. et al. STE-QUEST—test of the universality of free fall using cold atom interferometry. *Classical and Quantum Gravity*, 31(11):115010, 2014. URL `http://stacks.iop.org/0264-9381/31/i=11/a=115010`.

[12] Airbus Defence and Space.

[13] Amaro-Seoane, P. et al. Laser Interferometer Space Antenna. *ArXiv e-prints*, February 2017.

[14] Anderson, G. et al. Experimental results from the ST7 mission on LISA Pathfinder. *Phys. Rev. D*, 2018.

[15] Antonucci, F. et al. The LISA Pathfinder mission. *Classical and Quantum Gravity*, 29(12):124014, 2012. URL `http://stacks.iop.org/0264-9381/29/i=12/a=124014`.

[16] Armano, M. et al. The LISA Pathfinder Mission. *Journal of Physics: Conference Series*, (610):012005, 2015.

[17] Armano, M. et al. Sub-Femto-g Free Fall for Space-Based Gravitational Wave Observatories: LISA Pathfinder Results. *Phys. Rev. Lett.*, 116:231101, Jun 2016. doi: 10.1103/PhysRevLett.116.231101. URL `https://link.aps.org/doi/10.1103/PhysRevLett.116.231101`.

[18] Armano, M. et al. Capacitive sensing of test mass motion with nanometer precision over millimeter-wide sensing gaps for space-borne gravitational reference sensors. *Phys. Rev. D*, 96:062004, Sep 2017. doi: 10.1103/PhysRevD.96.062004. URL `https://link.aps.org/doi/10.1103/PhysRevD.96.062004`.

[19] Armano, M. et al. Charge-Induced Force Noise on Free-Falling Test Masses: Results from LISA Pathfinder. *Phys. Rev. Lett.*, 118:171101, Apr 2017. doi: 10.1103/PhysRevLett.118.171101. URL `https://link.aps.org/doi/10.1103/PhysRevLett.118.171101`.

[20] Armano, M. et al. Measuring the Galactic Cosmic Ray flux with the LISA Pathfinder radiation monitor. *Astroparticle Physics*, 98:28 – 37, 2018. ISSN 0927-6505. doi: https://doi.org/10.1016/j.astropartphys.2018.01.006.

[21] Armano, M. et al. Beyond the Required LISA Free-Fall Performance: New LISA Pathfinder Results down to 20μHz. *Phys. Rev. Lett.*, 120:061101, Feb 2018. doi: 10.1103/PhysRevLett.120.061101. URL `https://link.aps.org/doi/10.1103/PhysRevLett.120.061101`.

[22] Armano, M. et al. Beyond the Required LISA Free-Fall Performance: New LISA Pathfinder Results down to 20μHz, additional material. *Phys.Rev.Lett.*, 2018.

[23] Armano, M. et al. Calibrating the system dynamics of LISA Pathfinder. *Phys. Rev. D*, 97:122002, Jun 2018. doi: 10.1103/PhysRevD.97.122002. URL `https://link.aps.org/doi/10.1103/PhysRevD.97.122002`.

[24] Armano, M. et al. Characteristics and Energy Dependence of Recurrent Galactic Cosmic-Ray Flux Depressions and of a Forbush Decrease with LISA Pathfinder. *The Astrophysical Journal*, 854(2):113, Feb 2018. doi: 10.3847/1538-4357/aaa774.

[25] Armano, M. et al. Temperature stability in the sub-milliHertz band with LISA Pathfinder. *Monthly Notices of the Royal Astronomical Society*, 486(3):3368–3379, 04 2019. ISSN 0035-8711. doi: 10.1093/mnras/stz1017. URL `https://doi.org/10.1093/mnras/stz1017`.

[26] Astone, P. et al. The next science run of the gravitational wave detector NAUTILUS. *Classical and Quantum Gravity*, 19(7):1911–1917, Mar 2002. doi: 10.1088/0264-9381/19/7/392.

[27] Bender, P. et al. LISA for the detection and observation of gravitational waves. Prephase A. Technical Report 244. Technical report, Max Plank fr Quantenoptik, 1998.

[28] Bortoluzzi, D. et al. Testing LISA drag-free control with the LISA technology package flight experiment. *Class. Quantum Grav.*, 20:89–97, 2003.

[29] Cañizares, P. et al. The diagnostics subsystem on board LISA Pathfinder and LISA. *Classical and Quantum Gravity*, 26(9):094005, 2009. URL `http://stacks.iop.org/0264-9381/26/i=9/a=094005`.

[30] Herbert B. Callen and Richard F. Greene. On a theorem of irreversible thermodynamics. *Phys. Rev.*, 86:702–710, Jun 1952. doi: 10.1103/PhysRev.86.702. URL `https://link.aps.org/doi/10.1103/PhysRev.86.702`.

[31] Carbone, L. et al. Thermal gradient-induced forces on geodesic reference masses for LISA. *Phys. Rev. D*, 76(10):102003, Nov 2007. doi: 10.1103/PhysRevD.76.102003.

[32] Cavalleri, A. et al. Increased Brownian Force Noise from Molecular Impacts in a Constrained Volume. *Phys. Rev. Lett.*, 103(14):140601, Sep 2009. doi: 10.1103/PhysRevLett.103.140601.

[33] Cerdonio, M. et al. The ultracryogenic gravitational-wave detector AURIGA. *Classical and Quantum Gravity*, 14(6):1491–1494, Jun 1997. doi: 10.1088/0264-9381/14/6/016.

[34] Marc Díaz-Aguiló. *Magnetic Diagnostics Algorithms for LISA Pathfinder: System Identification and Data Analysis*. PhD thesis, Universitat Politècnica de Catalunya, 2011.

[35] Rita Dolesi. Temperature dependent contributions to Delta g. *Slides for the meeting: Thermal analysis during the LPF mission, Trento*, 2017.

[36] Dolesi, R. et al. Gravitational sensor for LISA and its technology demonstration mission. *Classical and Quantum Gravity*, 20(10):S99, 2003. URL `http://stacks.iop.org/0264-9381/20/i=10/a=312`.

[37] Dwyer, S. et al. Advanced LIGO status. *Journal of Physics: Conference Series*, 610:012013, May 2015. doi: 10.1088/1742-6596/610/1/012013.

[38] A Einstein. Über Gravitationswellen. *Sitzungsberichte der Königlich Preussischen Akademie der Wissenschaften zu Berlin*, page p. 154, 1918.

[39] E J Elliffe et al. Hydroxide-catalysis bonding for stable optical systems for space. *Classical and Quantum Gravity*, 22(10):S257–S267, apr 2005. doi: 10.1088/0264-9381/22/10/018.

[40] Eyer, L. et al. The Gaia mission. *arXiv:1303.0303*, 2013.

[41] Ferdman, R. D. et al. The European Pulsar Timing Array: current efforts and a LEAP toward the future. *Classical and Quantum Gravity*, 2010.

[42] Antonio F. García-Marín. *Minimasation of optical pathlength noise for the detection of gravitational waves with the spaceborn laser interferometer LISA and LISA Pathfinder*. PhD thesis, Gotfried Wilhelm Leibniz Universität Hannover, 2007.

[43] García Marín, A. F. et al. On-orbit alignment and diagnostics for the LISA Technology Package. *Class. Quantum Grav.*, 23:133–140, 2006.

[44] Gibert, F. et al. Thermo-elastic induced phase noise in the LISA Pathfinder spacecraft. *Classical and Quantum Gravity*, 32(4):045014, 2015. URL `http://stacks.iop.org/0264-9381/32/i=4/a=045014`.

[45] B Gustavsen and A Semlyen. Rational approximation of frequency domain responses by vector fitting. *IEEE Trans. Power Delivery*, 14 (3):1052–1061, 1999.

[46] Ferran Gibert Gutiérrez. *Thermal diagnostics experiments for LISA PathFinder*. PhD thesis, Universitat Politècnica de Catalunya, 2015.

[47] Harry, G. M. et al. Advanced LIGO: the next generation of gravitational wave detectors. *Classical and Quantum Gravity*, 27(8):084006, Apr 2010. doi: 10.1088/0264-9381/27/8/084006.

[48] Hechenblaikner, G. et al. Digital Laser Frequency Control and Phase-Stabilization Loops in a High Precision Space-Borne Metrology System. *IEEE Journal of Quantum Electronics*, 47(5):651–660, May 2011. ISSN 0018-9197. doi: 10.1109/JQE.2011.2108637.

[49] Heinzel, G. et al. Interferometry for the LISA technology package (LTP) aboard SMART-2. *Class. Quantum Grav.*, 20:153–161, 2003.

[50] Heinzel, G. et al. The LTP interferometer and Phasemeter. *Class. Quantum Grav.*, 21:581–587, 2004.

[51] Martin Hewitson. Mission Operation for LISA Pathfinder. *Slides for the COSPAR meeting, Moscow*, 2014.

[52] Hewitson, M. et al. Data analysis for the LISA Technology Package. *Class. Quant. Grav.*, 26:094003, 2009. doi: 10.1088/0264-9381/26/9/094003.

[53] Hobbs, G. et al. The International Pulsar Timing Array project: using pulsars as a gravitational wave detector. *Classical and Quantum Gravity*, 2010.

[54] R.A. Hulse and J.H. Taylor. Discovery of a pulsar in a binary system. *Astroph. Jour. (Letters)*, 195 (L59):51–53, 1975.

[55] Íñiguez, J. et al. Magnetic levitation by induced eddy currents in non-magnetic conductors and conductivity measurements. *European Journal of Physics*, 26(6):951–957, Aug 2005. doi: 10.1088/0143-0807/26/6/002.

[56] Bert Janssen. Expansión del campo débil. *Universidad de Granada*.

[57] Nikolaos Karnesis. *Bayesian data analysis for LISA Pathfinder*. PhD thesis, Universitat Autònoma de Barcelona, 2014.

[58] Lämmerzahl, C. et al. OPTIS: a satellite-based test of special and general relativity. *Classical and Quantum Gravity*, 18(13):2499, 2001. URL `http://stacks.iop.org/0264-9381/18/i=13/a=312`.

[59] A. Lobo, M. Nofrarias, J. Ramos-Castro, and J. Sanjuán. On-ground tests of LISA Pathfinder thermal diagnostics system. *Class. Quant. Grav.*, 23:5177–5194, 2006. doi: 10.1088/0264-9381/23/17/005.

[60] J A Lobo. Effect of a weak plane GW on a light beam. *Classical and Quantum Gravity*, 9(5):1385–1394, May 1992. doi: 10.1088/0264-9381/9/5/019. URL `https://doi.org/10.1088%2F0264-9381%2F9%2F5%2F019`.

[61] I. Mateos and I. Lloro. DMU Temperature Data Conversion. Technical Note S2-IEC-TN-3091, Institut de Ciències de l'Espai (ICE-IEEC/CSIC), 2011.

[62] McNamara, P. et al. The LISA Pathfinder mission. *ASP Conference Series*, 2013.

[63] Josep Sanjuán Muñoz. *Development and validation of the thermal diagnostics instrumentation in LISA Pathfinder*. PhD thesis, Universitat Politècnica de Catalunya, 2009.

[64] Miquel Nofrarias. *Thermal Diagnostics in the LISA Technology Package Experiment*. PhD thesis, Universitat de Barcelona, 2007.

[65] Nofrarias, M. et al. Thermal diagnostic of the optical window on board LISA Pathfinder. *Classical and Quantum Gravity*, 24(20):5103–5121, 2007. URL `http://stacks.iop.org/0264-9381/24/5103`.

[66] Nofrarias, M. et al. Subtraction of temperature induced phase noise in the LISA frequency band. *Phys. Rev. D*, 87:102003, May 2013. doi: 10.1103/PhysRevD.87.102003. URL `https://link.aps.org/doi/10.1103/PhysRevD.87.102003`.

[67] Ogburn IV, R. W. et al. The BICEP2 CMB polarization experiment. *Proceedings of SPIE - The International Society for Optical Engineering*, 2010.

[68] Paczkowski, S. et al. Laser Frequency Noise Stabilisation and Interferometer Path Length Differences on LISA Pathfinder. *Journal of Physics: Conference Series*, 840:012004, May 2017. doi: 10.1088/1742-6596/840/1/012004.

[69] Giuseppe D. Racca and Paul W. McNamara. The LISA Pathfinder Mission. *Space Science Reviews*, 151(1):159–181, Mar 2010. ISSN 1572-9672. doi: 10.1007/s11214-009-9602-x.

[70] Piero Rapagnani. Gravitational wave detectors on the earth. *Classical and Quantum Gravity*, 27(19):194001, sep 2010. doi: 10.1088/0264-9381/27/19/194001. URL `https://doi.org/10.1088%2F0264-9381%2F27%2F19%2F194001`.

[71] Robertson, D. et al. LTP interferometer—noise sources and performance. *Classical and Quantum Gravity*, 22(10):S155–S163, Apr 2005. doi: 10.1088/0264-9381/22/10/004.

[72] J. Sanjuán and M. Nofrarias. Non-linear quantization error reduction for the temperature measurement subsystem on-board LISA Pathfinder. *Review of Scientific Instruments*, 89(4):045004, 2018. doi: 10.1063/1.5012692. URL `https://doi.org/10.1063/1.5012692`.

[73] Josep Sanjuán. Calibration of FMNTC Thermistors. Technical report, Institut de Ciències de l'Espai (ICE-CSIC), 2010.

[74] Sanjuán, J. et al. Thermal diagnostics front-end electronics for LISA Pathfinder. 78(10):104904, 2007. ISSN 00346748. doi: 10.1063/1.2800776. URL `http://dx.doi.org/doi/10.1063/1.2800776`.

[75] Sanjuán, J. et al. Magnetic polarisation effects of temperature sensors and heaters in LISA Pathfinder. *Review of Scientific Instruments*, 79:084503, 2008.

[76] Sanjuán, J. et al. Analog-to-digital converters nonlinear errors correction in thermal diagnostics for the laser interferometer space antenna mission. *Review of Scientific Instruments*, 80:114901, 2009.

[77] B. Schutz. *A First Course in General Relativity*. Cambridge University Press, 1985.

[78] Sheard, B. S. et al. Intersatellite laser ranging instrument for the GRACE follow-on mission. *Journal of Geodesy*, 86(12):1083–1095, Dec 2012. ISSN 1432-1394. doi: 10.1007/s00190-012-0566-3. URL `https://doi.org/10.1007/s00190-012-0566-3`.

[79] Kentaro Somiya. Detector configuration of KAGRA–the japanese cryogenic gravitational-wave detector. *Classical and Quantum Gravity*, 29(12):124007, Jun 2012. doi: 10.1088/0264-9381/29/12/124007.

[80] Carlo Gavacci Space. Optical Window Breadboard. Personal technical note.

[81] Carlo Gavacci Space. OPTICAL WINDOW ASSEMBLY LEAK TEST REPORT. October 2005. LTP project technical note.

[82] Stefansson, G. et Al. A Versatile Technique to Enable Sub-milli-Kelvin Instrument Stability for Precise Radial Velocity Measurements: Tests with the Habitable-zone Planet Finder. *The Astrophysical Journal*, 833(2):175, 2016. URL `http://stacks.iop.org/0004-637X/833/i=2/a=175`.

[83] DDS team. S2-NTE-MA-3001 DDS USER MANUAL. Technical report, Institut de Ciències de l'Espai (ICE-IEEC/CSIC), 2014.

[84] LISA TEAM. LISA, Laser Intereferometer Space Antenna. *Proposal*, 2017.

[85] The eLISA Consortium. The Gravitational Universe. *ArXiv e-prints*, May 2013.

[86] S Timoshenko. *Strength of materials*. 1956.

[87] Massimo Tinto and Sanjeev V. Dhurandhar. Time-delay interferometry. *Living Reviews in Relativity*, 17(1):6, Aug 2014. ISSN 1433-8351. doi: 10.12942/lrr-2014-6.

[88] `http://lpf.esac.esa.int/lpfsa/`.

[89] `https://gracefo.jpl.nasa.gov/`.

[90] `https://science.gsfc.nasa.gov/`.

[91] `https://www.ligo.org/`.

[92] `http://www.rssd.esa.int/index.php?project=LISA&page=index` and `http://sci.esa.int/lisapf`. Official ESA websites of the LISA project.

[93] van Haasteren, R. et al. Placing limits on the stochastic gravitational-wave background using European Pulsar Timing Array data. *Monthly Notices of the Royal Astronomical Society*, 414(4):3117–3128, 2011. doi: 10.1111/j.1365-2966.2011.18613.x. URL http://dx.doi.org/10.1111/j.1365-2966.2011.18613.x.

[94] S. Vitale. Effect of eddy currents on down-conversion of magnetic noise. *Memo LISA Technology Package*, 2007.

[95] Vitale, S. et al. Data series subtraction with unknown and unmodeled background noise. *Phys. Rev. D*, 90:042003, Aug 2014. doi: 10.1103/PhysRevD.90.042003. URL https://link.aps.org/doi/10.1103/PhysRevD.90.042003.

[96] Misner C. W., Thorne K. S., and Wheeler J. A. *Gravitation*. W. H. Freeman and Company, New York, 1973.

[97] Gudrun Wanner and Nikolaos Karnesis. Preliminary results on the suppression of sensing cross-talk in LISA Pathfinder. *Journal of Physics: Conference Series*, 840:012043, may 2017. doi: 10.1088/1742-6596/840/1/012043. URL https://doi.org/10.1088%2F1742-6596%2F840%2F1%2F012043.

[98] J. Weber. Detection and generation of gravitational waves. *Phys. Rev.*, 117:306–313, Jan 1960. doi: 10.1103/PhysRev.117.306. URL https://link.aps.org/doi/10.1103/PhysRev.117.306.

[99] J. Weber. Evidence for Discovery of Gravitational Radiation. *Phys. Rev. Lett.*, 22:1320–1324, Jun 1969. doi: 10.1103/PhysRevLett.22.1320. URL https://link.aps.org/doi/10.1103/PhysRevLett.22.1320.

[100] J. Weber. Anisotropy and Polarization in the Gravitational-Radiation Experiments. *Phys. Rev. Lett.*, 25:180–184, Jul 1970. doi: 10.1103/PhysRevLett.25.180. URL https://link.aps.org/doi/10.1103/PhysRevLett.25.180.

[101] William Joseph Weber. LISA Pathfinder and eLISA: measuring differential acceleration for gravitational wave astrophysics. *Slides for the Iberian Gravitational Wave Meeting, Barcelona*, 2015.

[102] C Zanoni, D Bortoluzzi, J W Conklin, I Kker, B Seutchat, and S Vitale. Summary of the results of the LISA-Pathfinder Test Mass release. *Journal of Physics: Conference Series*, 610:012022, may 2015. doi: 10.1088/1742-6596/610/1/012022. URL `https://doi.org/10.1088%2F1742-6596%2F610%2F1%2F012022`.

[103] Zhu, X. -J. et al. An all-sky search for continuous gravitational waves in the Parkes Pulsar Timing Array data set. *Monthly Notices of the Royal Astronomical Society*, 444(4):3709–3720, 2014. doi: 10.1093/mnras/stu1717. URL `http://dx.doi.org/10.1093/mnras/stu1717`.